

DTIC FILE COPY

1

AD-A212 887

CURRENT MANAGEMENT FOR IMPROVED  
RAILGUN PERFORMANCE

DTIC  
ELECTE  
SEP 25 1989  
S D D

APPROVED BY  
SUPERVISORY COMMITTEE:

Wm. F. Webb

Herbert A. Woodson

J. D. Higgs

W. R. Osterhoff

Eric F. Fuentun

Edward J. Pomeroy

DISTRIBUTION STATEMENT A  
Approved for public release  
Distribution Unlimited

89 9 25 036

# REPORT DOCUMENTATION PAGE

Form Approved  
OMB No. 0704-0188

Public reporting burden for this collection of information is estimated to average 1 hour per response, including the time for reviewing instructions, searching existing data sources, gathering and maintaining the data needed, and reviewing the collection of information. Send comments regarding this burden estimate or any other aspect of this collection of information, including suggestions for reducing the burden, to Washington Headquarters Services, Directorate for Information Operations and Reports, 1215 Jefferson Davis Highway, Suite 1204, Arlington, VA 22202-4302, and to the Office of Information and Regulatory Affairs, Office of Management and Budget, Washington, DC 20503.

1. AGENCY USE ONLY (Leave Blank)		2. REPORT DATE Aug 89	3. REPORT TYPE AND DATES COVERED Ph D Dissertation
4. TITLE AND SUBTITLE Current Management for Improved Railgun Performance			5. FUNDING NUMBERS
6. AUTHOR(S) Joseph H. Bena			
7. PERFORMING ORGANIZATION NAME(S) AND ADDRESS(ES) U.S. Student Detachment Ft Benjamin Harrison, IN 46216			8. PERFORMING ORGANIZATION REPORT NUMBER
9. SPONSORING/MONITORING AGENCY NAME(S) AND ADDRESS(ES) <del>FAPC</del> HQ DA Milpore DAPC-OPB-D			10. SPONSORING/MONITORING AGENCY REPORT NUMBER
11. SUPPLEMENTARY NOTE			
12a. DISTRIBUTION/AVAILABILITY STATEMENT Unclassified, available to public			12b. DISTRIBUTION CODE
13. ABSTRACT (Maximum 200 words) The potential for active and passive current management in railgun rails is investigated. Multi-rail and two-rail railgun optimized rail designs are presented which have increased performance, lower peak rail currents and improved rail mechanical containment properties.			
SUBJECT TERMS Railgun, electromagnetic launchers, current distribution			15. NUMBER OF PAGES 220
			16. PRICE CODE
17. SECURITY CLASSIFICATION OF REPORT unclassified	18. SECURITY CLASSIFICATION OF THIS PAGE unclassified	19. SECURITY CLASSIFICATION OF ABSTRACT unclassified	20. LIMITATION OF ABSTRACT UL

## GENERAL INSTRUCTIONS FOR COMPLETING SF 298

The Report Documentation Page (RDP) is used in announcing and cataloging reports. It is important that this information be consistent with the rest of the report, particularly the cover and title page. Instructions for filling in each block of the form follow. It is important to *stay within the lines* to meet optical scanning requirements.

**Block 1. Agency Use Only (Leave blank).**

**Block 2. Report Date.** Full publication date including day, month, and year, if available (e.g. 1 Jan 88). Must cite at least the year.

**Block 3. Type of Report and Dates Covered.** State whether report is interim, final, etc. If applicable, enter inclusive report dates (e.g. 10 Jun 87 - 30 Jun 88).

**Block 4. Title and Subtitle.** A title is taken from the part of the report that provides the most meaningful and complete information. When a report is prepared in more than one volume, repeat the primary title, add volume number, and include subtitle for the specific volume. On classified documents enter the title classification in parentheses.

**Block 5. Funding Numbers.** To include contract and grant numbers; may include program element number(s), project number(s), task number(s), and work unit number(s). Use the following labels:

C - Contract	PR - Project
G - Grant	TA - Task
PE - Program Element	WU - Work Unit Accession No.

**Block 6. Author(s).** Name(s) of person(s) responsible for writing the report, performing the research, or credited with the content of the report. If editor or compiler, this should follow the name(s).

**Block 7. Performing Organization Name(s) and Address(es).** Self-explanatory.

**Block 8. Performing Organization Report Number.** Enter the unique alphanumeric report number(s) assigned by the organization performing the report.

**Block 9. Sponsoring/Monitoring Agency Name(s) and Address(es).** Self-explanatory.

**Block 10. Sponsoring/Monitoring Agency Report Number.** (If known)

**Block 11. Supplementary Notes.** Enter information not included elsewhere such as: Prepared in cooperation with...; Trans. of...; To be published in.... When a report is revised, include a statement whether the new report supersedes or supplements the older report.

**Block 12a. Distribution/Availability Statement.** Denotes public availability or limitations. Cite any availability to the public. Enter additional limitations or special markings in all capitals (e.g. NOFORN, REL, ITAR).

DOD - See DoDD 5230.24, "Distribution Statements on Technical Documents."

DOE - See authorities.

NASA - See Handbook NHB 2200.2.

NTIS - Leave blank.

**Block 12b. Distribution Code.**

DOD - Leave blank.

DOE - Enter DOE distribution categories from the Standard Distribution for Unclassified Scientific and Technical Reports.

NASA - Leave blank.

NTIS - Leave blank.

**Block 13. Abstract.** Include a brief (Maximum 200 words) factual summary of the most significant information contained in the report.

**Block 14. Subject Terms.** Keywords or phrases identifying major subjects in the report.

**Block 15. Number of Pages.** Enter the total number of pages.

**Block 16. Price Code.** Enter appropriate price code (NTIS only).

**Blocks 17. - 19. Security Classifications.** Self-explanatory. Enter U.S. Security Classification in accordance with U.S. Security Regulations (i.e., UNCLASSIFIED). If form contains classified information, stamp classification on the top and bottom of the page.

**Block 20. Limitation of Abstract.** This block must be completed to assign a limitation to the abstract. Enter either UL (unlimited) or SAR (same as report). An entry in this block is necessary if the abstract is to be limited. If blank, the abstract is assumed to be unlimited.

Copyright  
by  
Joseph Henry Beno, Jr.  
1989

**CURRENT MANAGEMENT FOR IMPROVED  
RAILGUN PERFORMANCE**

by

**JOSEPH HENRY BENO, B.S., M.S.**

**DISSERTATION**

**Presented to the Faculty of the Graduate School of  
The University of Texas at Austin  
in Partial Fulfillment  
of the Requirements  
for the Degree of  
DOCTOR OF PHILOSOPHY**

**THE UNIVERSITY OF TEXAS AT AUSTIN**

**August 1989**

Accession #	
NTIS ORNL	
DTIC TAB	
Unannounced	
Justification	
By	
Distribution	
Availability Codes	
Dist	Availability Codes
A-1	

## ACKNOWLEDGEMENTS

As is customary and appropriate at the successful completion of an important endeavor, such as a dissertation, I wish to express heartfelt appreciation for the contributions of other people and organizations to my life and to this work. In most cases, this is long overdue and my thanks really should have been expressed many times before.

First, I would like to thank my parents. Their love, nurturing, and guidance still affects my life, more than twenty years after leaving home. Especially significant in this dissertation effort has been the desire to continue the formal education process -- a trait which has been instilled in myself, my sister and my brother.

My entire supervisory committee has earned my appreciation for their help, patience, and time. Special thanks to committee members Professor Mircea D. Driga and Dean Herbert H. Woodson for their concern, support, and assistance. Of course, the contributions of my supervisor, Professor William F. Weldon, cannot be adequately acknowledged. The insights gained during our frequent, and often lengthy, discussions were of inestimable value. I also should mention that I found these meetings to be very enjoyable.

While it would be impractical to mention everybody by name, I would like to thank my associates at the University of

Texas-Center for Electromechanics for their hospitality, free exchange of ideas, help, and cooperation. Within this organization, the overworked and under-appreciated group known as the "grad studs" deserve special recognition.

Although there has been no significance to the order in which I previously mentioned people or organizations, I have saved the most important people for last. The person who has had the most profound impact on my life has been my best friend for twenty years, my wife for eighteen years, and fellow graduate student for the last two years. I thank Cindy for the love, support, encouragement, and fun she has given me for twenty years, and I look forward to the next 200 years (or more). My two sons, Jeff and Tim, exceed all my reasonable expectations and most of my unreasonable expectations. The happiness they continually bring me, and their patience and understanding for the last three years deserve my special thanks.

Joseph H. Beno

The University of Texas at Austin  
August 1989

## **CURRENT MANAGEMENT FOR IMPROVED RAILGUN PERFORMANCE**

Publication No. \_\_\_\_\_

Joseph Henry Beno Jr., Ph.D.  
The University of Texas at Austin, 1989

Supervising Professor: William F. Weldon

Continued railgun development toward high energy devices that launch useful projectiles and have a lifetime of hundreds to thousands of shots, requires progress in two related aspects of accelerator design: 1) rail containment structures must be made capable of withstanding greater rail repulsion forces, without causing accelerators to become too bulky for their intended use; and 2) rails must sustain very minor heat-related damage during projectile launch. These issues are related because they primarily represent direct effects of railgun current and its distribution.



The potential for managing rail current and its distribution to alleviate the two aforementioned problems is investigated. Techniques for calculating pulsed, rail current distribution, in the infinite conductivity approximation, and resultant projectile force are developed. Then, passive, current management methods -- involving multiple rail pairs to distribute currents and rail-repulsive forces in a few, evenly-spaced, radial directions, for easier rail containment -- are explored. Optimized multi-rail, railgun cross-sectional shapes that produce more projectile force than conventional two-rail railguns operating under the same local peak current density constraints are determined. These railguns have nontraditional bore shapes, i.e., not square or round.

The use of neighboring, current-carrying conductors to actively influence rail current distribution is then studied. Optimized, square- and round-bore, railgun geometries, employing separately-powered auxiliary conductors, are developed. Compared with conventional, two-rail railguns, or normal, augmented, two-rail railguns, these designs produce three to seven fold increases in projectile force, for the same local peak current density limits. Additionally, the possibility of restricting current to inner rail surfaces to ease armature design and interfacing is explored. Active current management measures are then combined with multi-rail concepts to produce viable, round-bore, multi-rail railguns, employing active current management.

Finally, implementation issues for the active and passive current management techniques are addressed. Series-connected railguns, with optimized, active current management, that require only one power supply are devised. Projectile interface problems are identified.

## Table of Contents

Acknowledgements .....	i
Abstract. ....	iii
Table of Contents. ....	v
List of Illustrations .....	viii
List of Tables. ....	xiii
Chapter 1. Introduction and Problem Definition	
1.1 Electromagnetic Railguns. ....	1
1.2 The Present State of Railgun Technology. ....	5
1.3 Problem Description. ....	7
1.4 General Approach and Dissertation Organization . . . .	10
Chapter 2. Analysis and Computation of Railgun Current Distribution, Inductance Gradient, and Forces	
2.1 Introduction. ....	14
2.2 Current Density Calculations .....	17
2.3 Calculation of Railgun Inductance Gradient and Associated Force .....	31

### Chapter 3. Multiple Rails for Passive Current Management

3.1	Introduction . . . . .	38
3.2	Two- and Four-Rail, Square-Bore Railguns. . . . .	40
3.3	Four-Rail, X-Bore Railguns. . . . .	57
3.4	Four-Rail Railguns with Trapezoidal-Shaped Rails. . . . .	64
3.5	Multi-Rail Optimization. . . . .	71
3.6	Chapter Conclusion. . . . .	85

### Chapter 4. Active Shaping of Rail Current

4.1	Introduction. . . . .	86
4.2	Force, Current Distribution, and Inductance Gradient Calculations . . . . .	89
4.3	Current Density Limits on Conductors Other Than the Accelerator Rails. . . . .	97
4.4	Square-Bore Current Guard Plates. . . . .	105
4.5	Round-Bore Railguns: Baseline Performance. . . . .	127
4.6	Force-Optimized Round-Bore Guard Plates. . . . .	135
4.7	Current-Optimized Round-Bore Guard Plates. . . . .	148
4.8	Chapter Conclusion. . . . .	159

## Chapter 5. Four-Rail, Round-Bore Railguns with Current Guard Plates

5.1	Introduction. . . . .	162
5.2	Force-Optimized Round-Bore Guard Plates for Four-Rail Railguns. . . . .	164
5.3	Current-Optimized Round-Bore Guard Plates for Four-Rail Railguns . . . . .	173
5.4	Chapter Conclusion . . . . .	178

## Chapter 6 Concluding Remarks

6.1	Introduction. . . . .	179
6.2	Recovered Projectiles . . . . .	182
6.3	Design Implementation. . . . .	192
6.4	Summary and Conclusions . . . . .	206

Appendix A: Magnetic Field Plots. . . . .	210
---	-----

List of References. . . . .	217
-----------------------------	-----

## List of Illustrations

Figure 1.1:	Railgun Components . . . . .	3
Figure 1.2:	Railgun with Support Structure . . . . .	4
Figure 1.3:	Two-Rail Railguns. . . . .	11
Figure 2.1:	Square-Bore Railgun Geometry . . . . .	21
Figure 2.2:	Normalized Current Density: Two-Rail, Square-Bore Railgun. . . . .	26
Figure 2.3:	Numerical Convergence. . . . .	30
Figure 3.1:	Four-Rail, Square-Bore Geometry. . . . .	41
Figure 3.2:	Normalized Current Density: Two-Rail, Square-Bore Railgun. . . . .	43
Figure 3.3:	Normalized Current Density: Four-Rail, Square-Bore Railgun. . . . .	44
Figure 3.4:	Normalized Current Density: Four-Rail, Square-Bore Railgun. . . . .	45
Figure 3.5:	Normalized Current Density: Two-Rail, Square-Bore Railgun. . . . .	47
Figure 3.6:	Normalized Current Density: Four-Rail, Square-Bore Railgun. . . . .	48
Figure 3.7:	Inductance Gradient: Four-Rail, Square-Bore Railgun. . . . .	49
Figure 3.8:	Current and Force: Four-Rail, Square-Bore Railgun. . . . .	51
Figure 3.9:	Inductance Gradient: Four-Rail, Square-Bore Railgun. . . . .	53
Figure 3.10:	Current and Force: Four-Rail, Square-Bore Railgun. . . . .	54
Figure 3.11:	X-Bore Geometry. . . . .	56

Figure 3.12:	Normalized Current Density: Four-Rail, X-Bore Railgun. . . . .	59
Figure 3.13:	Inductance Gradient: Four-Rail, X-Bore Railgun. . . . .	60
Figure 3.14:	Current and Force: Four-Rail, X-Bore Railgun. . . . .	61
Figure 3.15:	X-Bore Railgun: Equal Force as Two-Rail Railgun. . . . .	62
Figure 3.16:	Four-Rail Railgun with Trapezoidal Rails. . . .	65
Figure 3.17:	Force for Railguns with Trapezoidal Rails: Four-Rail Railgun. . . . .	68
Figure 3.18:	Force for Railguns with Trapezoidal Rails: Four-Rail Railgun. . . . .	69
Figure 3.19:	Force for Railguns with Trapezoidal Rails: Four-Rail Railgun. . . . .	70
Figure 3.20:	Rail Corner Designs. . . . .	73
Figure 3.21:	Optimum Multi-Rail Railgun . . . . .	79
Figure 3.22:	Normalized Current Density: Four Trapezoidal Rails; Maximum Force Geometry . . . . .	80
Figure 3.23:	Optimum Six-Rail Railgun . . . . .	82
Figure 3.24:	Optimum Eight-Rail Railgun. . . . .	83
Figure 3.25:	Two-Rail, Square-Bore Railgun. . . . .	84
Figure 4.1:	Augmented Rail Geometry . . . . .	90
Figure 4.2:	Representative Armature Design . . . . .	102
Figure 4.3:	Square-Bore Guard Plates . . . . .	108
Figure 4.4:	Normalized Rail Current Density: Two-Rail, Square-Bore, Augmented Railgun . . . . .	111
Figure 4.5:	Normalized Augmenting Current Density: Two-Rail, Square-Bore, Augmented Railgun. . . . .	112
Figure 4.6:	Rail and Guard Plate Current Densities . . . .	116
Figure 4.7:	Rail and Guard Plate Current Densities . . . .	117
Figure 4.8:	Rail and Guard Plate Current Densities . . . .	118
Figure 4.9:	Rail and Guard Plate Current Densities . . . .	119
Figure 4.10:	Force vs. Vector Potential Ratios . . . . .	121

Figure 4.11:	Force Optimized Square-Bore Railgun . . . . .	124
Figure 4.12:	Normalized Rail Current Density . . . . .	125
Figure 4.13:	Normalized Guard Plate Current Density . . . . .	126
Figure 4.14:	Round-Bore Railgun . . . . .	128
Figure 4.15:	Normalized Rail Current Density: Two-Rail, Round-Bore Railgun. . . . .	129
Figure 4.16:	Round-Bore, Augmented Railgun . . . . .	133
Figure 4.17:	Normalized Rail Current Density: Two-Rail, Round-Bore, Augmented Railgun. . . . .	134
Figure 4.18:	Round-Bore Guard Plate Design. . . . .	137
Figure 4.19:	Force-Optimized, Round-Bore Railgun with Guard Plates . . . . .	140
Figure 4.20:	Normalized Rail Current Density: Two Rail, Railgun with Guard Plates . . . . .	141
Figure 4.21:	Normalized Guard Plate Current Density: Two-Rail Railgun with Guard Plates . . . . .	142
Figure 4.22:	Force-Optimized, Round-Bore Railgun with Guard Plates (Without Overhang). . . . .	144
Figure 4.23:	Normalized Rail Current Density: Two-Rail Railgun with Guard Plates (Without Overhang). . . . .	145
Figure 4.24:	Normalized Guard Plate Current Density: Two-Rail Railgun with Guard Plates . . . . .	146
Figure 4.25:	Normalized Rail Current Density: Two Rail Railgun with Guard Plates . . . . .	152
Figure 4.26:	Normalized Rail Current Density: Two-Rail Railgun with Guard Plates . . . . .	153
Figure 4.27:	Current-Optimized, Round-Bore Railgun with Guard Plates . . . . .	155
Figure 4.28:	Normalized Rail Current Density: Two-Rail Railgun with Guard Plates . . . . .	156
Figure 4.29:	Normalized Guard Plate Current Density: Two-Rail Railgun with Guard Plates . . . . .	157
Figure 5.1:	Force-Optimized, Round-Bore, Four-Rail Railgun with Guard Plates. . . . .	167



Figure 5.2:	Normalized Rail Current Density: Four-Rail Railgun with Guard Plates. . . . .	168
Figure 5.3:	Normalized Guard Plate Current Density: Four-Rail Railgun with Guard Plates. . . . .	169
Figure 5.4:	Force-Optimized, Round-Bore, Four-Rail Railgun with Guard Plates (Without Overhang). . . . .	170
Figure 5.5:	Normalized Rail Current Density: Four-Rail Railgun with Guard Plates. . . . .	171
Figure 5.6:	Normalized Guard Plate Current Density: Four-Rail Railgun with Guard Plates . . . . .	172
Figure 5.7:	Current-Optimized, Round-Bore, Four-Rail Railgun with Guard Plates . . . . .	175
Figure 5.8:	Normalized Rail Current Density: Four-Rail Railgun with Guard Plates . . . . .	176
Figure 5.9:	Normalized Guard Plate Current Density: Four-Rail Railgun with Guard Plates . . . . .	177
Figure 6.1:	Recovered Armature . . . . .	184
Figure 6.2:	Recovered Armature . . . . .	185
Figure 6.3:	Recovered Armature . . . . .	186
Figure 6.4:	Recovered Armature . . . . .	188
Figure 6.5:	Recovered Armature . . . . .	189
Figure 6.6:	Recovered Armature . . . . .	191
Figure 6.7:	Alternate Four-Rail Armature. . . . .	194
Figure 6.8:	Current Diffusion into a Flat Conductor . . . . .	198
Figure 6.9:	Force-Optimized, Round-Bore Railgun With Split Guard Plates (Without Overhang) . . . . .	200
Figure 6.10:	Normalized Rail Current Density: Two-Rail Railgun with Guard Plates (Without Overhang) . . . . .	202
Figure 6.11:	Normalized Guard Plate Current Density: Two-Rail Railgun with Guard Plates (Without Overhang) . . . . .	203

Figure 6.12:	Normalized Rail Current Density: Two-Rail Railgun with Split Guard Plates (Without Overhang) . . . . .	204
Figure 6.13:	Normalized Guard Plate Current Density: Two-Rail Railgun with Split Guard Plates (Without Overhang) . . . . .	205
Figure A.1:	Field Plot: Two-Rail, Round-Bore Railgun. .	212
Figure A.2:	Field Plot: Force-Optimized, Two-Rail, Round-Bore Railgun with Guard Plates. . . . .	213
Figure A.3:	Field Plot: Force-Optimized, Two-Rail, Round-Bore Railgun with Guard Plates (Without Overhang). . . . .	214
Figure A.4:	Field Plot: Current-Optimized, Two-Rail, Round-Bore Railgun with Guard Plates (Without Overhang). . . . .	215
Figure A.5:	Field Plot: Force-Optimized, Four-Rail, Round-Bore Railgun with Guard Plates (Without Overhang). . . . .	216

## List of Tables

Table 2.1:	"Benchmark" Square-Bore, Two-Rail Railgun Performance . . . . .	37
Table 4.1:	Current Density Limits for Auxiliary Conductors. . . . .	104
Table 4.2:	Augmented, Square-Bore Railgun Performance . . . . .	110
Table 4.3:	Force Optimization Results (Square Bore) . . . . .	122
Table 4.4:	Square-Bore and Round-Bore Railgun Performance Summary . . . . .	132
Table 4.5:	Force Optimization Results (Round Bore) . . .	147
Table 4.6:	Current Optimization Results (Round Bore). .	158
Table 5.1:	Force Optimization Results (Four-Rail, Round Bore). . . . .	166
Table 5.2:	Current Optimization Results (Four-Rail, Round Bore). . . . .	174
Table 6.1:	Split Guard Plate Performance Comparison. . . . .	201

# Chapter 1

## Introduction and Problem Definition

### Chapter Outline

1.1	Electromagnetic Railguns. . . . .	1
1.2	The Present State of Railgun Technology . . . . .	5
1.3	Problem Description . . . . .	7
1.4	General Approach and Dissertation Organization. . . .	10

### 1.1 Electromagnetic Railguns

The development of devices which use electromagnetic forces to launch projectiles has been the goal of a few researchers since the early 1900's, and has received substantial attention in the last ten years. Most of this effort has been expended in an attempt to electromagnetically do a job better which is already done very well using chemical propellants, i.e., launching military projectiles. However, other tasks which are not practicable or possible with chemical propellants, such as impact fusion, hypervelocity material development, and earth to space launch of waste material, have also received serious consideration (Fair 1982).

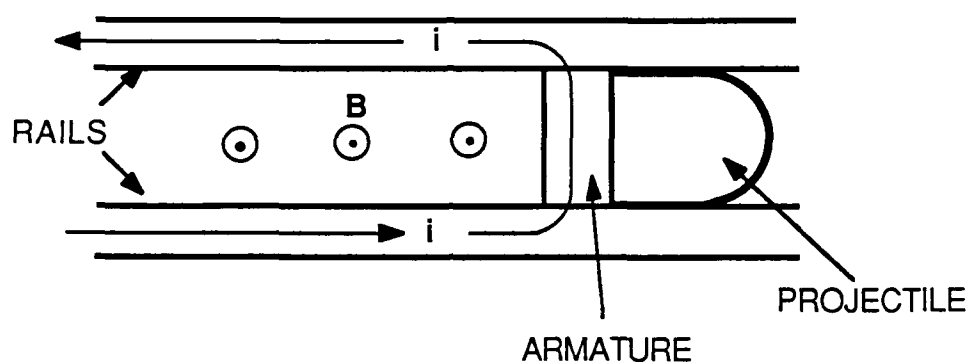
Railguns, the simplest electromagnetic accelerators, have received most of the research effort and achieved the most spectacular results. These devices consist of parallel, current-

carrying conductors (the rails) bridged by a conducting solid or plasma armature, as shown in Figure 1.1. Figure 1.1a depicts a railgun with two rails, as is customary, although designs with more than two rails are also possible. Figures 1.1b and 1.1c show transverse cross-sections of square-bore, two- and four-rail railguns. The armature is acted on by a Lorentz force, caused by the interaction of armature current with the magnetic fields in the bore. The armature then either pushes a projectile or is an intrinsic part of the projectile. The fields which create a Lorentz force on the armature also create outward forces on the rails which must be restrained. The structure that supports and restrains the rails is not shown in Figure 1.1, but it is necessary that the portions of this structure adjacent to the rails and bore area be a dielectric material. The cross-section of a typical laboratory railgun support structure is shown in Figure 1.2 (Long 1987). Not shown in either Figure 1.1 or 1.2 are the necessary power sources, power conditioning equipment, switches, and cooling systems which, with the accelerator, constitute an entire railgun system.

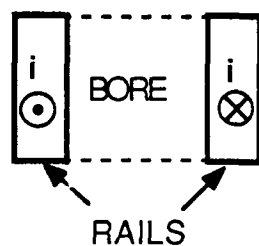
Most currently envisioned railgun tasks involve a short duration launch of a high energy projectile. Typically, projectile energies are one to twenty megajoules and launch times are one to ten milliseconds. This dictates that useful railguns operate as pulsed current devices, driven by pulsed power supplies. Maximization of projectile acceleration requires that rail and armature current densities be very high. Figure 1.1 schematically shows the current as existing in the rails, but gives no indication of the actual distribution of the high, pulsed current on (or in) the rails. This dissertation is concerned with

## RAILGUN COMPONENTS

(A) TOP VIEW



(B) END VIEW



(C) END VIEW

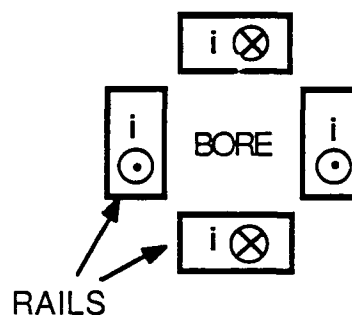


**FIGURE 1.1:** Two-rail and four-rail railguns. The rails, armature, projectile, current ( $i$ ), and magnetic field ( $B$ ) which is into the page, for a two-rail railgun are shown in Figure (a). The Lorentz force acting on the projectile is to the right in Figure (a). Figures (b) and (c) depict rail cross-sections and currents (into and out of the page) for two- and four-rail railguns.

## RAILGUN WITH SUPPORT STRUCTURE

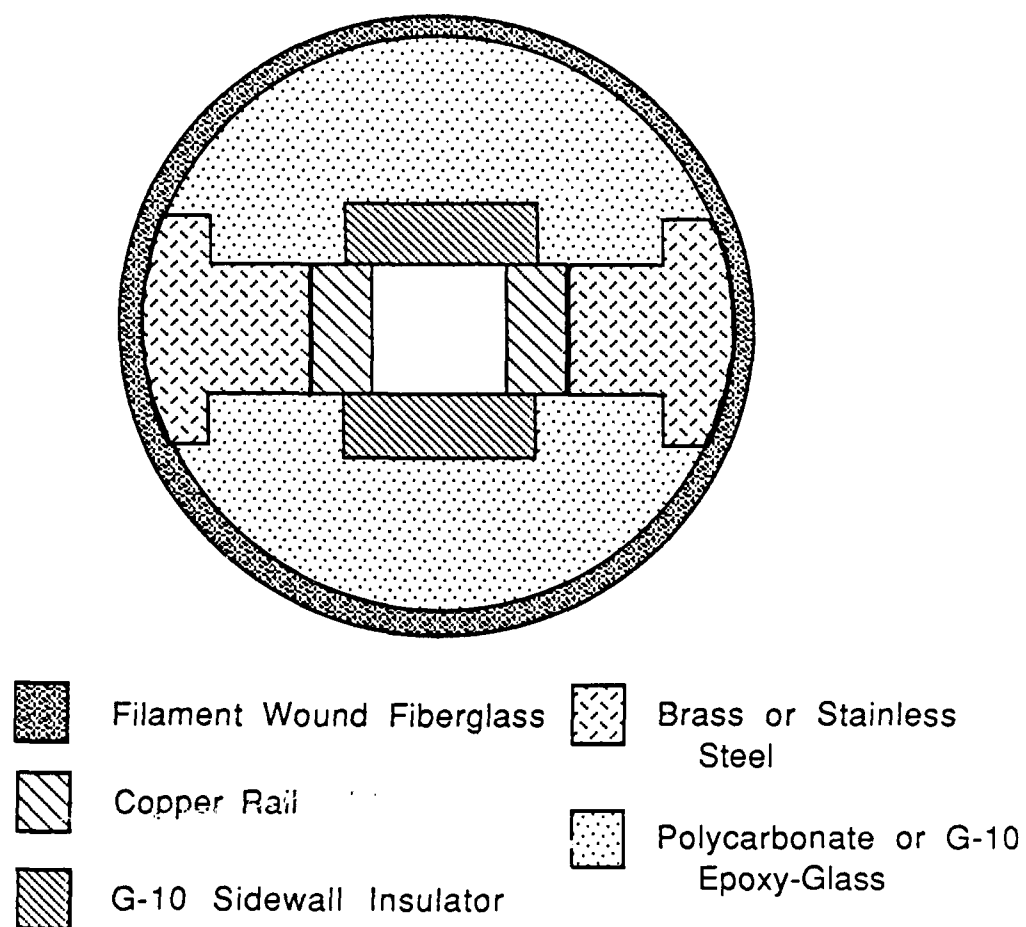


FIGURE 1.2: A common laboratory railgun support structure.

this current distribution, and how to control it to maximize railgun acceleration capabilities.

## 1.2 The Present State of Railgun Technology

Although there was some interest in electromagnetic launchers at least 85 years ago and some development during World War II, railgun successes at the Australian National University (ANU) in the 1970's sparked the recent interest (Fair 1982). The ANU group, under the direction of Richard Marshall, concentrated on railgun accelerator and projectile development. They achieved moderate success with solid armatures and developed the concept of a plasma armature, attaining a velocity of 5.9 km/s with a 3 gram projectile (kinetic energy = 52 kJ). The ANU railguns were powered by a three story tall, 500 megajoule (MJ) homopolar generator.

A railgun system built by Westinghouse Electric Corporation for the U.S. Army, currently installed in the Army railgun laboratory at Picatinney Arsenal, N.J., represented the next major step in railgun development. This railgun had a square, two-inch bore, and achieved a velocity of 4.2 km/s with a 317 gram solid armature projectile (kinetic energy = 2.8 MJ) in 1982 (Deis, Sherbarth, and Ferrantino 1984). Designed as a laboratory demonstrator, the railgun was powered by a 17.5 MJ homopolar generator and was the first device to launch projectiles with sufficient mass and energy to be of military interest. Although the projectile size and energy were of military interest, the rate of fire (one shot per week) and the durability (one to five shots per pair of rails) highlighted the



progress required before a military weapon system could be fielded.

In the 1980's, electromagnetic launch became the focus of a large military research program with substantial funding. Consequently, many universities and defense corporations developed railgun laboratories; and since then progress on the various components of railgun systems has been steady. Perhaps the most significant achievement has been the development of compact, high-energy density, homopolar generators and compensated pulsed alternators (compulsators) by the University of Texas-Center for Electromechanics (UT-CEM). This compact power supply development has allowed a steady succession of military weapon concept designs for artillery, anti-armor, and air defense, vehicular-mounted weapon systems. Although not yet built, these conceptual designs represent estimates of the potential of electromagnetic guns for military use. The first designs were two-vehicle artillery systems (one entire 60 ton, armored, tracked vehicle was dedicated to power supplies), and the more recent designs are one-vehicle systems which rival current chemical propellant artillery systems in size and performance. The author participated in several of these conceptual design efforts from 1982 to 1984.

In the last two years, high-energy shots of military interest have become commonplace. UT-CEM built a railgun with a 90 mm bore which fires 2 kg armor-penetrating projectiles at velocities of 2 km/s. However, artillery-type weapons (50 kg projectiles with a velocity of 600-800 m/s) have not yet been demonstrated. Also, sustained rates of fire and railgun durability are still far below that required for the military.

Typically, today's high-energy railguns display unacceptable armature and rail damage during a shot. Most damage is heat-related. The armature usually experiences substantial melting and material vaporization, while the rails and the dielectric material above and below the rails experience similar damage to a lesser degree. The rail damage causes degraded armature-rail contact on subsequent shots, which aggravates the heating problem. The outgrowth is that railguns require new rails or rail honing after just a few shots. Since plasma armature railguns require a good seal around the projectile to prevent plasma from leaking around the projectile, the dielectric material above and below the rails requires frequent replacement in these railguns.

### **1.3 Problem Description**

As railgun development continues toward higher energy devices capable of firing larger projectiles, more progress must be made in two aspects of accelerator design: 1) rail containment structures must be made capable of withstanding the greater repulsion forces exerted on the rails, without causing accelerators to become too bulky for their intended use (such as trunnion mounted, military projectile launchers); and 2) accelerators must be made capable of sustaining hundreds or thousands of shots, with sufficiently minor heat-related damage that rail honing or component replacement is not necessary. These two issues are related because poor rail containment allows rail flexing, causing poor rail-armature contact and aggravated rail damage. Both issues are further related in that

they primarily represent direct effects of railgun current and its distribution, as discussed in the following paragraphs.

First, rail containment will be discussed. Restraining the rails during a high-energy firing is especially difficult for two-rail railguns because the two rails directly repel each other. The net forces on the two rails are, therefore, oppositely directed and in the same plane. In contrast, the outward forces on the walls of a conventional, chemical propellant cannon are radially directed, evenly distributed, and comparatively easy to restrain. Distributing rail forces in a few, evenly-spaced radial directions, allows tremendous simplification in required accelerator structural design. Accordingly, using four or more parallel rails that are evenly positioned around the circumference of the railgun bore is a method of favorably distributing rail separation forces in space to facilitate railgun design. Although railgun development so far has been almost exclusively devoted to two-rail railguns, multi-rail railguns are now receiving some consideration.

The second issue, rail thermal damage, will be discussed next. The sources of the heat-related rail damage for a solid-armature railgun are: 1) heat generated by the rail-armature interface contact voltage drop; 2) Joule-heating from the current in the rails; and 3) friction heating. The first two sources of damage are strongly dependent on the local current density. As will be shown in subsequent chapters, the distribution of pulsed rail current is not uniform and exhibits extreme concentrations in the vicinity of sharp rail corners. In the past, effort has been devoted to passive measures which reduce local peak current densities e.g., by designing rails with

a cross-sectional shape without sharp corners etc. However, these measures generally have disadvantages concerning the rail-armature interface in the vicinity of rail corners (this will be explained further in Chapter 3). But because current distribution in a conductor is affected by neighboring currents, using auxiliary current-carrying conductors to influence rail current distribution is an attractive method of reducing the local rail current density peaks and reducing rail damage.

Consequently, the use of multiple pairs of rails to distribute railgun current in space and the use of auxiliary conductors to influence the current distribution on a rail are prime means of managing railgun current distribution to improve railgun performance. The use of auxiliary, current-carrying conductors is an active method of managing current; the use of multiple pairs of rails is passive. As might be expected, similar analytical techniques can be used to investigate both active and passive current management.

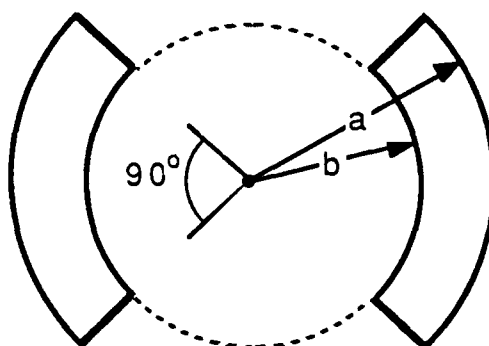
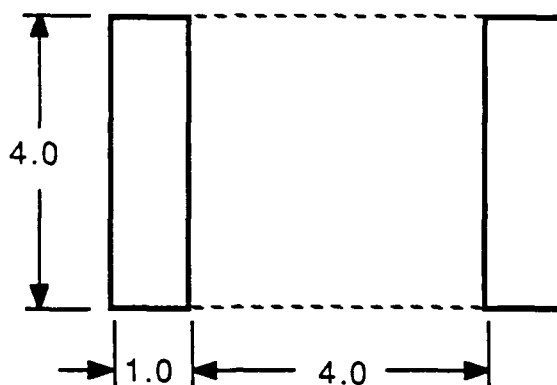
This dissertation is an investigation into railgun current management techniques with two objectives: 1) develop multi-rail railgun configurations which perform at least as well as the conventional two-rail railgun, but have improved distribution of the outward rail forces; and 2) develop active current control measures to influence rail current distribution for improved railgun performance capability. Since railguns are used to accelerate projectiles, for this dissertation, the performance capability of a railgun is judged by the force exerted on the armature. However, since railgun durability is a critical issue affecting the ultimate usefulness of a railgun, increasing projectile force at the expense of increased rail damage is not

acceptable. Accordingly, in this dissertation, railgun performance is quantified by its force-producing capability, subject to the limitation that local current densities cannot be allowed to exceed a specified limit. Furthermore, this dissertation is concerned only with railguns, the accelerator portion of a railgun system. Other system components, such as power supplies, power conditioning equipment, and switches are not considered, and other concerns, such as overall system efficiency are also not considered.

#### **1.4 General Approach and Dissertation Organization**

The research objective of this dissertation, as stated at the end of the previous section, necessarily implies comparative studies: multi-rail railguns must be compared with conventional two-rail railguns to find viable alternatives with comparable performance, but without some of the disadvantages of the two-rail railguns; and railguns employing active current management must be compared with conventional two-rail railguns to find alternatives with improved performance. For these comparative studies, based on the performance criterion of projectile force, a two-rail railgun must be selected as the standard. The two-rail railguns of Figure 1.3, with 16 square centimeter bores and 1.0 cm thick rails, are representative of many railguns found in the literature, and were selected as "benchmark" square- and round-bore railguns. The selection of these benchmark railguns is not intended to unnecessarily limit the applicability of the results of this dissertation, but, rather to provide a framework in which to make comparisons. Although

## TWO-RAIL RAILGUNS



$$a = 3.257$$

$$b = 2.257$$

**FIGURE 1.3:** Square- and round-bore railguns. These "benchmark" railguns have a 16 sq. cm bore and 1.0 cm thick rails. Dimensions shown are in centimeters.

the specifics will be discussed in later chapters, the conduct of the comparative studies for this dissertation was such that the general conclusions are widely applicable. Specific design examples, with rail dimensions applicable only to 16 square centimeter bore railguns, are presented to illustrate the more general conclusions (although direct scaling of these designs may be useful for many purposes). There is no attempt to make this dissertation a source for charts, tables, or graphs to allow, with perhaps a few simple calculations, design of improved railguns to meet every possible railgun objective.

It has already been stated that the railgun performance criterion for the comparative studies of this dissertation is projectile force producing capability, subject to the limitation that local peak current densities cannot exceed a specified limit. The specified limit for rail current density used in this dissertation is a line current density, expressed in terms of arc length around the perimeter of the rail cross-section. The limit is specified as one MA/inch which is based on a general "rule of thumb" often cited by railgun designers. However, the comparative analyses have been conducted so that the actual limit of "one MA/inch" is not important. It is only important that a limit be consistently applied.

This dissertation is intended to present quantitative results of research, as well as a logical development of ideas and concepts. Therefore, it is appropriate that the first topics to be addressed are the necessary theory and computational procedures developed to calculate the force-producing capability of railguns. Chapter 2 is devoted to these topics.

With Chapter 2 as background, the remainder of the dissertation is oriented toward presenting quantitative results. Chapters 3 and 4 discuss the topics of multi-rail railguns and active current management in two-rail railguns, respectively. These two chapters are intended to be independent of each other, so that readers interested in only one topic need not become enmeshed in the other. Consequently, concepts, theory, and procedures which apply only to one of the two chapters are developed within that chapter. Also, Chapters 3 and 4 each contain their own concluding remarks, to further promote independence. It is useful to interject that abbreviated, journal-style summaries of much of the research discussed in these chapters are available in two articles by Beno and Weldon (1989a,1989b). Chapter 5 combines the multi-rail concepts of Chapter 3 and the active current management concepts of Chapter 4 to discuss four-rail railguns with active current management. Chapter 6 presents some suggestions for future research and concluding remarks.



## Chapter 2

### Analysis and Computation of Railgun Current Distribution, Inductance Gradient, and Forces

#### Chapter Outline

2.1	Introduction . . . . .	14
2.2	Current Density Calculations. . . . .	17
2.3	Calculation of Railgun Inductance Gradient and Associated Force. . . . .	31

#### 2.1 Introduction

The objective of this chapter is to develop the analytical tools necessary to predict railgun accelerator performance. As mentioned in Chapter 1, an accelerator's performance is quantified solely by its force-producing capability, subject to the limitation that local current densities cannot be allowed to exceed a specified limit. It is widely known that the force on a railgun projectile can be expressed as  $F = \frac{1}{2} L' i^2$ , where  $L'$  is the accelerator inductance per unit length, or inductance gradient, and  $i$  is the total accelerator current. However, since the projectile is in motion and railguns usually operate in a pulsed mode, the current distributes itself in a complex, time-dependent manner throughout the rails and projectile. This

distribution must be known or approximated in order to calculate the inductance gradient.

Until recently, most attempts to analyze current related aspects of a railgun involved assuming a current distribution on the inside of the rails, the surfaces of the two rails which face each other (see, for example, Young and Hughes 1982; Drake and Rathmann 1986; and Long 1986). Often, the assumed distribution was a uniform current diffused into the rails to some (skin) depth considered appropriate for the launch times involved. Using this approximation, inductance for a unit length of railgun can be calculated from the formula for mutual inductance of a pair of parallel filaments by integrating over the region of assumed currents (Grover 1946; Chapters 2 and 3). If the assumed current distribution is nonuniform, the local current density is used as a weighting function in the integration. Although this method is conceptually simple, the integrations usually must be done numerically and the results obtained for simple two-rail railguns only agree with experimental results to within approximately 15%. Furthermore, extending this method to more complicated geometries, such as two rails within a cylindrical, steel containment structure or a four-rail railgun, is difficult because the current distribution becomes more uncertain. It is quickly realized that a better means of approximating current distribution is needed.

Work done by Kerrisk (1981) showed that actual current distributions in railguns are very different from what was often assumed. Kerrisk developed a technique for calculating current distribution for long, parallel conductors and inductance per unit

length in a high-frequency, or infinite conductivity limit. Although Kerrisk's technique was somewhat cumbersome and used an existing Los Alamos National Laboratory computer code (unavailable to the general public) to generate a cubic spline approximation for the current distribution, his work represents a milestone in understanding the current distribution in railgun rails (including some of the more complicated cases). Furthermore, the inductance gradients calculated using these current distributions were shown by Kerrisk to very accurately predict the projectile force developed by a railgun. Kerrisk's work has gradually achieved more widespread acceptance. Leuer (1986) developed a calculational method using a least-squares curve fit routine to calculate infinite conductivity, parallel conductor, current distributions, and inductance gradients which is more easily replicated than Kerrisk's method. He then applied the technique to several railgun geometries, including railguns with augmenting turns. The University of Texas-Center for Electromechanics (UT-CEM) has extensively used inductance gradients based on infinitely-conducting conductors in modeling work since November 1987, with success for a variety of railgun geometries. The computer program used at UT-CEM is based on Leuer's method.

In addition to the aforementioned computational advancements, experimental and modeling work done at UT-CEM has shown that the measured inductance per unit length which most correctly predicts projectile force is that which is measured using a high-frequency source. This is in agreement with findings in other railgun laboratories (Deis, Scherbarth and Ferrentino 1984).

Due to the above considerations, an appropriate approximation for rail current distribution is to model the rails as infinitely conducting. Then, determination of the force producing capability of an accelerator involves finding the current distribution and inductance per unit length of long, infinitely conducting, parallel conductors in a region remote from the projectile. For this dissertation, a method of calculating this current distribution based on an analogy with the charge distribution on a capacitor composed of long, parallel conductors was developed. The resulting equations and concepts are simple, which gives this method the distinct advantage that current distributions can be more readily visualized and understood than with the methods developed by Kerrisk and Leuer. Additionally, appropriate simplifying assumptions which greatly improve computer computational times can readily be conceived. In the next section, this method is presented.

## 2.2 Current Density Calculations

As stated by Kerrisk without proof (1981), if one assumes infinite rail conductivity, calculating the rail current distribution is equivalent to finding the electrostatic charge distribution on long, parallel conductors when the electric potential,  $V$ , is known.<sup>1</sup> The analogy can be established by beginning with Ampere's Law in the magnetostatic case:

---

<sup>1</sup> Lewis (1966), a reference cited by Kerrisk, does provide a brief discussion concerning the equivalence of electrostatic and rapidly pulsed magnetic field equations for some conductor configurations.

$$\nabla \times \mathbf{B} = \mu_0 \mathbf{J} \quad (2.1)$$

where  $\mathbf{B}$  is the magnetic flux density and  $\mathbf{J}$  is the current density. Defining the magnetic vector potential,  $\mathbf{A}$ , in the usual manner, by the equation  $\mathbf{B} = \nabla \times \mathbf{A}$ ; using the vector identity  $\nabla \times (\nabla \times \mathbf{A}) = \nabla (\nabla \cdot \mathbf{A}) - \nabla^2 \mathbf{A}$ ; and setting the divergence of  $\mathbf{A}$  to be zero, yields the following equation relating the vector potential and current density:

$$\nabla^2 \mathbf{A} = -\mu_0 \mathbf{J} \quad (2.2)$$

For long, parallel conductors, as in railguns in a region remote from the projectile, the current is entirely in one direction which can be taken to be in the  $z$  direction. Then, in Cartesian coordinates, equation 2.2 becomes a scalar equation:

$$\nabla^2 A_z = -\mu_0 J_z \quad (2.3)$$

This equation is the same form as that which relates the electric potential to charge in electrostatics:

$$\nabla^2 V = -\frac{\rho}{\epsilon_0} \quad (2.4)$$

where  $V$  is electric potential and  $\rho$  is charge density.

The identical format of equations 2.3 and 2.4 is not sufficient to establish an analogy between current and charge distribution. Boundary conditions and distribution of source

terms must also be considered. For long, parallel, infinitely conducting, railgun conductors, all current resides on the surface. In the electrostatic case, for the same conductors, all charge also resides on the surface. Boundary conditions on the electric and magnetic fields require that both  $A_z$  and  $V$  be continuous at the conductor boundary (Smythe 1950; Chap 8.04). Therefore, by basic properties of functions which obey the Laplace equation (as  $A_z$  and  $V$  do on the interior of the conductors), one finds that  $A_z$  is constant everywhere inside and on the surface of the long rails. This is also widely known to be true for  $V$ . The analogy between  $A_z$  and  $V$ , and between  $J_z$  and  $\rho$  is, therefore, complete. Furthermore, symmetry considerations indicate that an equal and opposite electric potential on the two long conductors will produce an identical charge distribution on each conductor which differs only in sign. Consequently, it is apparent that the appropriate situation for railgun rails with equal but opposite current is to have equal but opposite vector potentials,  $A_z$ , on each rail. The analogy which has been established can now be exploited to find the rail surface current density,  $J_z$ .

From electrostatic theory, it is known that surface charge density for long conductors obeys the following integral equation:

$$V = \int \frac{\sigma(s', z')}{|\mathbf{r} - \mathbf{r}'|} da' \quad (2.5)$$

In this equation,  $\sigma(s,z)$  is the surface charge density, expressed as a function of arc length along the perimeter of the conductor cross-section,  $s$  in Figure 2.1, and position along the length of conductor,  $z$ . Physical constants have been absorbed into  $V$  for algebraic simplicity. Primes denote charge coordinates, and the integration is over the three dimensional surface of the rails (which is the location of the electrostatic charge). Near the middle of long conductors, the surface charge varies little with position  $z$ , and can be expressed as a line charge density,  $\sigma(s)$ . This does not eliminate integration over the  $z$  coordinate in equation 2.5. Once the electric potential is specified, the above integral equation can be numerically solved for  $\sigma(s)$  using the method of moments. As mentioned above, if  $V$  is specified as equal and opposite on the two rails,  $\sigma(s)$  (near the middle of the rails) will have the same distribution (multiplied by a constant) as would the surface line current near the middle of infinite-conductivity rails.

Numerical solution of equation 2.5 using the method of moments involves expanding  $\sigma(s)$  in terms of subsectional basis functions and forcing equation 2.5 to be satisfied in the weak or variational sense. A more complete discussion than that given below is provided by Harrington (1968).

Using a two-rail railgun as an example, only the upper half of the right rail need be considered due to symmetry. A unit length section from the middle of a long section of rail will be considered, since this will more readily provide inductance per unit length later. The perimeter of this portion of rail is divided into  $N$  sections,  $\Delta s$  (Figure 2.1). Each section represents a strip

# SQUARE-BORE RAILGUN GEOMETRY

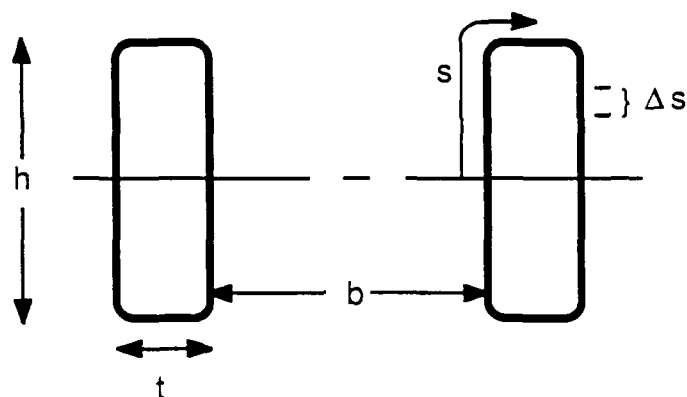


**FIGURE 2.1:** Cross-section of square-bore railgun. Dark lines show a two-rail railgun, defining the rail height ( $h$ ), rail thickness ( $t$ ), bore dimension ( $b$ ), the arc length along the rail perimeter ( $s$ ), and an increment of arc length,  $\Delta s$ . The arc length origin is at the inside center of the right rail. The current is equal and opposite on the two rails.



of charge, which extends into the paper one unit length. Now  $\sigma(s)$  can be expanded in terms of  $N$  basis functions,  $g_n(s)$ :

$$\sigma(s) \approx \sum_{n=1}^N a_n g_n(s) \quad (2.6)$$

where each basis function is defined to be nonzero on only one of the  $N$  sections. Therefore, a nonzero basis function is associated with each subsection,  $\Delta s_j$ , and the basis functions are such that  $g_j(s) = 0$  on all  $\Delta s_i$  for  $i \neq j$ . The result is that equation 2.5 becomes:

$$V = \int \frac{\sum_{n=1}^N a_n g_n(s')}{|r-r'|} da' \quad (2.7)$$

In the language of Becker, Carey, and Oden (1981; Chapter 1), Equation 2.7 is to be satisfied in the weak or variational sense by multiplying each side of the equation by testing functions,  $w_m$ , and integrating over the domain which, in this case, is over the rail surface. The result is:

$$\int w_m V da = \int w_m \int \frac{\sum_{n=1}^N a_n g_n(s')}{|r-r'|} da' da \quad (2.8)$$

where equation 2.8 is to be satisfied for each test function,  $w_m$ . It remains to choose the basis and test functions. If the test functions are chosen as Dirac delta functions,  $\delta(r-r_m)$ , and the basis functions are chosen as pulse functions,

$$\begin{aligned} P_n(s) &= 1 \text{ for } s = s_n \\ &\text{and} \\ P_n(s) &= 0 \text{ for } s \neq s_n \end{aligned} \quad (2.9)$$

the following equation for the potential at the midpoint of each  $\Delta s_m$  results:

$$V = \sum_{n=1}^N b_{mn} a_n \quad (2.11)$$

where

$$b_{mn} = \int \frac{1}{|r_m - r'|} da_n' \quad (2.12)$$

In equations 2.11 and 2.12, all subscripted positions refer to the charge segment midpoint. Since  $V$  is a known specified

constant, equation 2.11 represents a set of linear equations which can be solved for the  $a_n$  coefficients, once the  $b_{mn}$  are known. By equations 2.6 and 2.9, the  $a_n$  then represent the magnitude of the charge (current) density over strip  $\Delta s_n$ .

Equation 2.12 for the  $b_{mn}$  shows that they have a simple physical interpretation. Each  $b_{mn}$  is the potential at the center of strip  $\Delta s_m$  due to a uniform unit charge density over strip  $\Delta s_n$  (recall, the physical constants were absorbed into  $V$ ). These integrations are somewhat involved if done analytically. While they can be done numerically, considerable simplification results with very little loss in accuracy, by using expressions for the potential at the midpoint of  $\Delta s_m$  due to a unit length line charge of appropriate magnitude located at the midpoint of  $\Delta s_n$ . The accuracy of this approximation has been investigated. The answers for current densities obtained using a program based on a numerical integration scheme, and those obtained using a program based on the the line charge approximation formulas, differ by an amount which is roughly equal to or less than the error which is associated with the numerical integration.

The formulas for the  $b_{mn}$ , using the line charge approximation, are not difficult to derive and special case examples are available to help verify results (Paris and Hurd 1969). For  $m \neq n$ , they are of the form:

$$b_{mn} = \Delta s_n \ln \left( \frac{\frac{L}{2} + \sqrt{d^2 + (\frac{L}{2})^2}}{-\frac{L}{2} + \sqrt{d^2 + (\frac{L}{2})^2}} \right) \quad (2.13)$$

where  $L$  is the length of the conductors (unit length) and  $d$  is the distance between the midpoints of sections  $m$  and  $n$ . For  $m=n$ ,  $b_{mm}$  represents the potential at the surface of a strip of charge which is  $\Delta s$  wide. This can be integrated analytically to yield:

$$b_{mm} = 2 \left\{ \Delta s_m \sinh^{-1}\left(\frac{L}{\Delta s_m}\right) + L \sinh^{-1}\left(\frac{\Delta s_m}{L}\right) \right\} \quad (2.14)$$

where  $L$  is again the length of the conductors (unit length).

Due to symmetry, it is only necessary to solve for the  $a_n$  coefficients in the first quadrant. Each  $b_{mn}$  in the system of equations for a two-rail railgun then has four contributions, one from each quadrant, of the form shown in equations 2.12, 2.13, or 2.14.

For this dissertation, the method just described has been a primary computational tool. A FORTRAN program was developed which evaluates the  $b_{mn}$  coefficients using equations 2.13 and 2.14, to form an  $N \times N$  matrix. This is then inverted using a standard International Mathematical and Statistical Library (IMSL) routine to produce the  $a_n$  coefficients in equation 2.11. Typical results from this program are presented below.

Figure 2.2 shows the current density of the top half of the right rail of a two-rail railgun. Other half-rails have identical distributions. The rails have a rectangular cross-section and the bore is square. The dimensions are those of the "benchmark" square-bore railgun described in Chapter 1. Therefore, referring to Figure 2.1, the bore ( $b$ ) is 4.0 cm, the rail height ( $h$ ) is 4.0 cm, and the rail thickness ( $t$ ) is 1.0 cm. For this plot, all rail corners are rounded with a radius of 0.1 cm. The position scale,

**NORMALIZED CURRENT DENSITY**  
TWO-RAIL, SQUARE-BORE RAILGUN

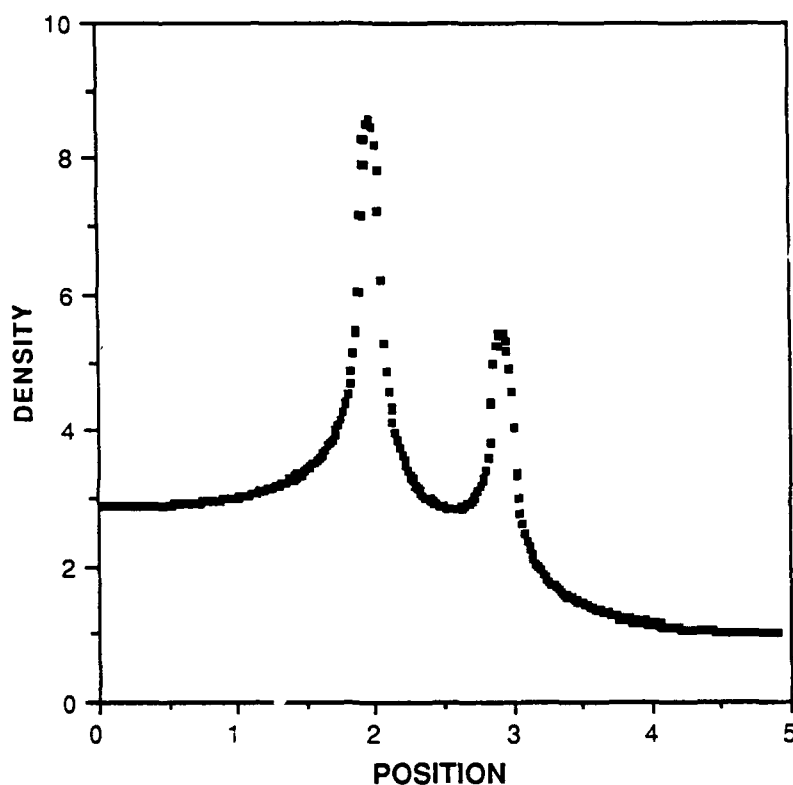


**FIGURE 2.2:** Normalized current density for a two-rail, square-bore railgun. Rail height = 4.0 cm. Rail thickness = 1.0 cm. Rail corner radii = 0.1 cm. Bore = 4.0 cm. The number of subsections used for this calculation was 300. The curve shown is composed of 300 square dots; each dot represents the current density of one subsection.

in cm, has its origin at the center of the inside face of the rail and proceeds around the top perimeter of the rail, ending at the center of the outside face of the rail. Current density has been normalized so that the density on the middle of the backside of the rail has a value of one. For this calculation, 300 subsections ( $\Delta s$  in Figure 2.1) were used and each square dot in the plot represents the normalized density at the center of one of these sections, i.e., at  $(\frac{\Delta s}{2}, \frac{L}{2})$ . **Unless otherwise mentioned, all current density plots in this dissertation have the position scale in centimeters, oriented as in this plot, and rail current densities are normalized, with the density on the middle of the rail backside being assigned a magnitude of one.**

When considering Figure 2.2, if the analogy between current and charge density is recalled, the shape of the current density plot is readily understood. The current density peaks occur at the corners of the rails, with the highest peak on the inside corner. The peak current density (position  $\approx 2.0$ ) is approximately three times the density on the center of the inside of the rails (position = 0.0) and approximately nine times the density on the backside of the rails (position  $\approx 4.9$ ).

Results obtained for current distribution using the computational technique developed for this dissertation have been extensively compared with those obtained using the previously mentioned techniques of Kerrisk and Leuer. In all cases, the three methods produce virtually identical results. Furthermore, Kerrisk showed his results to be in excellent agreement with the experimental results of Duke (1956), who

measured the high frequency current distribution of parallel conductors using segmented electrodes in an electrolytic tank.

It is appropriate at this point to briefly discuss the rounding of the rail corners, as was done for the results presented in Figure 2.2. Rounding is necessary because the charge distribution -- and, therefore the infinite conductivity current distribution -- at a sharp conductor corner is singular (Jackson 1975; Section 2.11). This, of course, does not pose a problem in physical conductors where ideal sharp corners do not exist. It should be pointed out that failure to round conductor corners does not cause numerical difficulties, since the  $b_{mn}$  coefficients represent the electric potential at the midpoint of a segment  $\Delta s$  and this midpoint generally does not lie precisely on a corner. However, failure to round corners causes uncertainties when interpreting results since the magnitude of the current density peaks calculated at the sharp corner would depend strongly on the smallness of  $\Delta s$  and how close the midpoint of  $\Delta s$  lies to the corner.

Convergence of the computational method discussed above remains to be addressed. Numerous trial runs have shown the method to converge relatively quickly as the number of subsections is increased, until answers change very little with further increases in the number of subsections. During the course of performing the calculations for this dissertation, convergence was checked for each new geometry encountered. However, in order to avoid redundancy, only one such check will be presented here. Figure 2.3 presents the variation of total calculated current with the number of subsections for the two-rail railgun calculation which was the subject of Figure 2.2.

Before integrating to find total current, the peak current density in Figure 2.2 was fixed at 1.0 MA/inch and the density elsewhere was scaled accordingly. After the number of subsections used has surpassed 125, increases in the number of subsections of approximately 30% produces less than a 0.1% change in the total current calculated. Careful scrutiny of Figure 2.3 also reveals very minor, slow oscillations for the calculated current in the level part of the curve. Review of the numerical output for Figure 2.3 shows these oscillations to be approximately 0.05% of the current magnitude. In all cases where this oscillation was noted, it remained extremely small and is a numerical effect. Such effects are common in numerical analysis and present no difficulty as long as the magnitude remains small.



## NUMERICAL CONVERGENCE

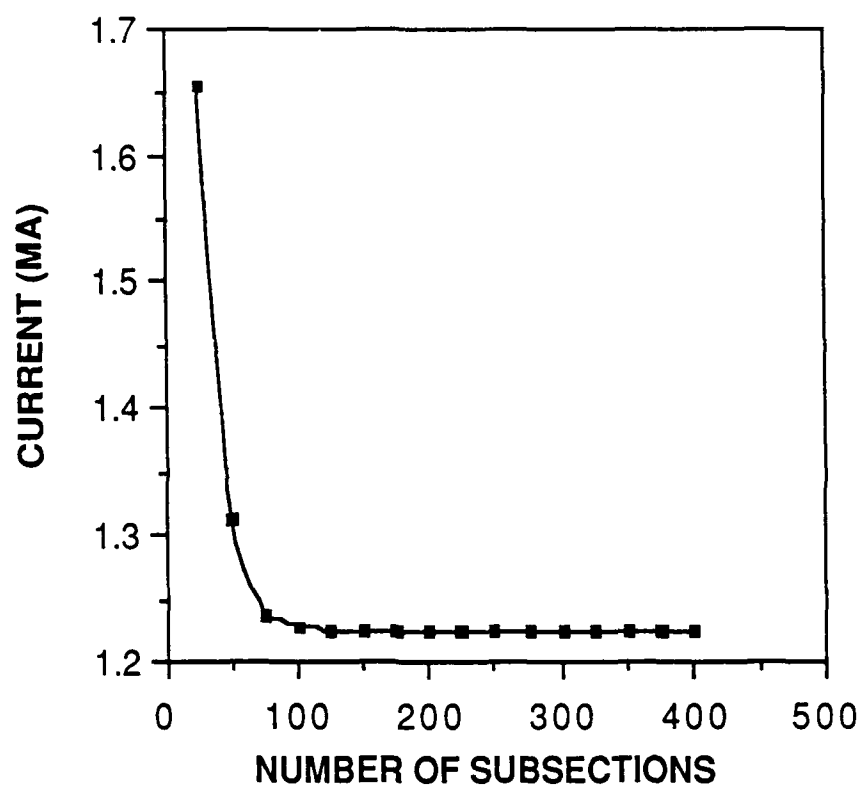


**FIGURE 2.3:** Numerical convergence of calculated current for the two-rail railgun. Rail height = 4.0 cm. Rail thickness = 1.0 cm. Rail corner radius = 0.1 cm. Bore = 4.0 cm.

### 2.3 Calculation of Railgun Inductance Gradient and Associated Force

After determining the current distribution of a unit length of rail, inductance per unit length,  $L'$ , (or inductance gradient where  $L' = \partial L / \partial z$ ) can be calculated. As mentioned previously, this could be accomplished by integrating the mutual inductance formulas for parallel line filaments, weighted with the local current densities, for each pair of line filaments existing over the surface of both rails. However, the expressions for the magnetic field energy provide a much simpler approach, as discussed below.

Before deriving the energy expressions which directly provide inductance, it is appropriate to briefly discuss two general approaches to the relationship between energy and inductance, a topic of interest to some readers. The discussion assumes a linear material, although it could be applied to nonlinear materials with some careful modifications.

Following the more common approach, most textbooks introduce inductance in terms of the magnetic flux from one circuit which links that circuit or another circuit. Inductance is then defined in terms of the flux through (closed) circuit 1 resulting from the current in (closed) circuit 2. For examples, see introductory college physics books such as Halliday and Resnick (1966), intermediate books on electromagnetic fields such as Ramo, Whinnery and Van Duzer (1984), or more advanced books such as Smythe (1950). From this beginning, the mutual energy between two circuits,  $W_m$ , is derived to be  $W_m = M_{12} i_1 i_2$ , where  $M_{12}$  is the mutual inductance,  $i_1$  is the current in circuit

1 and  $i_2$  is the current in circuit 2. Similarly, the self energy of a single circuit is found to be  $W_m = \frac{1}{2} Li^2$ , where  $L$  is the self inductance. Since this approach to inductance and energy is based on flux through closed circuits, application to portions of parallel conductors, such as railgun rails, without considering the remainder of the closed circuit, requires extensions to the theory which often seem somewhat inconsistent with the original definition of inductance. However, there is also another approach to the inductance concept which is, perhaps, more firmly based on fundamental quantities.

The second approach, as developed by Landau and Lifshitz in volume 8 of their series (1984; Sections 31-33), starts with a derivation of magnetic field energy as

$$W_m = \frac{1}{2} \int \mathbf{H} \cdot \mathbf{B} \, dv \quad (2.15)$$

where  $\mathbf{H}$  and  $\mathbf{B}$  are the magnetic field intensity and magnetic flux density vectors, respectively. The integration is over all space. This relation is derived assuming negligible displacement current and using the differential forms of Faraday's Law and the Ampere-Maxwell Law. From this beginning, the mutual energy between two currents is found to involve a constant of proportionality,  $M_{12}$ , and, again,  $W_m = M_{12}i_1i_2$ . Similarly, the self energy of a current is found to be  $W_m = \frac{1}{2} Li^2$ . At first, this may not seem different from the first approach, since Faraday's Law, which is the basis for

equation 2.15, was experimentally determined using closed circuits and, therefore, actually involves flux linkages through closed circuits. However, in volume 2 of their series, Landau and Lifshitz (1975) derive Maxwell's equations using only the theory of special relativity and variational principles. In this derivation, flux linkages are not necessary and, therefore, not used. The result is a consistent theory of electricity and magnetism in which the magnetic field energy can be considered without having to previously consider flux linkages through closed circuits. Therefore, inductance can be properly defined in terms of energy. Furthermore, inductance gradient (or inductance per unit length) calculations based on energy expressions for a finite length of parallel conductors, such as presented in Smythe (1950, pg 318), seem appropriate.

Following the second approach, a simple computation for inductance can be derived for use with the current density calculation discussed in the last section. First, an expression for magnetic energy,  $W_m$ , in terms of current density and the vector potential will be derived. Then, the inductance for a length of railgun can be found using  $W_m = \frac{1}{2} Li^2$ .

Beginning with equation 2.15, using  $\mathbf{B} = \mu_0 \mathbf{H}$  and the definition of the vector potential,  $\mathbf{A}$ , ( $\mathbf{B} = \nabla \times \mathbf{A}$ ) yields:

$$W_m = \frac{1}{2\mu_0} \int (\mathbf{B} \cdot \nabla \times \mathbf{A}) \, dv \quad (2.16)$$

where the integration is over all space. Now, following the derivation of Corson and Lorrain (1962), applying the vector

identity  $\nabla \cdot (\mathbf{A} \times \mathbf{B}) = \mathbf{B} \cdot (\nabla \times \mathbf{A}) - \mathbf{A} \cdot (\nabla \times \mathbf{B})$  and the divergence theorem results in the following equation:

$$W_m = \frac{1}{2\mu_0} \left\{ \int \mathbf{A} \cdot (\nabla \times \mathbf{B}) \, dv - \int (\mathbf{A} \times \mathbf{B}) \cdot d\mathbf{a} \right\} \quad (2.17)$$

where the first integral is a volume integral and the second integral is a surface integral over the surface surrounding the chosen volume. If the volume is all space, then  $\mathbf{B}$  is zero over the infinite surface (since  $\mathbf{B}$  diminishes with distance) and the second integral is zero. Now, using equation 2.1 produces the desired expression for magnetic energy:

$$W_m = \frac{1}{2} \int (\mathbf{J} \cdot \mathbf{A}) \, dv \quad (2.18)$$

where the integration includes all regions where the current density,  $\mathbf{J}$ , is not zero. This expression is valid for linear materials and, as shown in the next paragraph, is particularly easy to calculate after the current density calculation of Section 2.2 is completed.

Returning to the railgun discussed in the Section 2.2, recall that the vector potential,  $\mathbf{A}$ , was set to a constant,  $A_z$ , for the current density calculation and that the calculated current density,  $\mathbf{J}$ , is then a surface line current density. Therefore, taking  $\mathbf{A}$  outside the integral in equation 2.18 yields the following expression for the magnetic energy associated with *each* current carrying rail:

$$W_m = \frac{A}{2} \cdot \int J \, dv = \frac{A_z i}{2} \quad (2.19)$$

where  $i$  is the total rail current. The total rail current is easily calculated by adding the densities found using the method of moments (where the densities are the  $a_n$  in equation 2.6) and multiplying by two, since the densities were only calculated for the top half of the rail. The total magnetic energy associated with a length of railgun behind the projectile is twice that found with equation 2.19 for one rail. Once the energy in a length of railgun is calculated, the associated inductance is readily found from the expression  $W_m = \frac{1}{2} Li^2$ .

Continuing to work within the framework of the second approach to inductance (which does not involve flux linkages thru closed circuits), it is worthwhile to briefly mention the origin of the expression  $W_m = \frac{1}{2} Li^2$  which is often derived using flux linkages. For a known current distribution, the vector potential can be calculated using:

$$A = \frac{\mu_0}{4\pi} \int \frac{J}{|r-r'|} \, dv' \quad (2.20)$$

Substituting this expression into equation 2.18 produces the result that, if a current distribution is known, the magnetic energy associated with a current is proportional to the total current squared:

$$W_m = \frac{1}{2} L i^2 \quad (2.21)$$

where  $i$  is the total current (distributed in accordance with the known distribution) and the factor of proportionality,  $L$ , is defined to be the inductance. Of course this inductance can be related to flux in the usual manner, for those who are more accustomed to the "first approach" discussed at the beginning of this section.

The results of the preceding derivations make railgun force calculations extremely easy. If the current distribution calculated in accordance with the Section 2.2 is for a one meter length of railgun (where the rail separation is much less than 1 meter), equations 2.19 and 2.21 provide a means of readily calculating the inductance per unit length,  $L'$ , for the railgun. Then the projectile force is known to be (Woodson 1968):

$$F = \frac{\partial W_m}{\partial z} = \frac{L' i^2}{2} \quad (2.22)$$

Results are presented below for the square-bore, two-rail railgun which has the current density shown in Figure 2.2. The force and current calculations are made by assigning a maximum peak current density of 1.0 MA/inch (at position  $s \approx 2.0$  in Figure 2.2). Densities at other points on the rail are then scaled in accordance with Figure 2.2.

TABLE 2.1  
"BENCHMARK" SQUARE-BORE, TWO-RAIL,  
RAILGUN PERFORMANCE

Performance Parameter	Magnitude
Inductance Gradient	0.525 $\mu\text{H/m}$
Total Rail Current	1.224 MA
Projectile Force	0.393 MN



## Chapter 3

### Multiple Rails for Passive Current Management

#### Chapter Outline

3.1	Introduction. . . . .	38
3.2	Two- and Four-Rail, Square-Bore Railguns. . . . .	40
3.3	Four-Rail, X-Bore Railguns. . . . .	57
3.4	Four-Rail Railguns with Trapezoidal-Shaped Rails. . . . .	64
3.5	Multi-Rail Optimization. . . . .	71
3.6	Chapter Conclusion. . . . .	85

#### 3.1 Introduction

This chapter presents results of research seeking viable alternatives to conventional two-rail railguns which more evenly distribute outward forces exerted on the rail containment structure during projectile acceleration. This research objective leads to consideration of railguns with more than two rails which have the benefit of distributing the outward forces exerted on the rails over more than the single plane found in a two-rail railgun. This introductory section discusses the guiding tenets of the study.

A study of multi-rail alternatives necessarily involves investigating an assortment of railguns with different numbers of rails and different rail cross-sectional shapes. The only

candidate geometries investigated for this study incorporate symmetrical bore cross-sections with an even number of rails. Adjacent rails carry equal and opposite currents. Additionally, only accelerator capabilities, isolated from power supply and projectile considerations, were investigated. It has been assumed that a power supply exists which can drive the accelerators with any current desired.

The worthiness of potential multi-rail accelerator designs is determined by accelerator projectile force, which is compared with performance of the "benchmark" two-rail, square-bore railgun presented in Chapter 2. In all cases, peak current densities are limited to one MA/inch so that comparisons are made under conditions of similar rail damage. For the type of the comparisons made in this chapter, the actual magnitude of one MA/inch for the local current density limit is not important, as long as it remains unchanged for all comparisons.

In order to avoid comparing the force exerted by "big" guns with that of "small" guns, all geometries have the same cross-sectional bore area as the "benchmark" gun, i.e., 16 square centimeters. This also keeps armature weights roughly equal when comparing railguns.

Another somewhat subjective restriction to potential accelerator designs needs to be discussed. Recall that the infinite conductivity current distribution of Figure 2.2 is for a region of rail remote from the projectile. A remarkable feature of this distribution is the large proportion of rail current which flows on the top, bottom, and back surfaces of the rail. In the vicinity of the projectile, this current must flow over the rail

surfaces (around the rail perimeter in Figure 2.1) to reach the projectile. Although the three-dimensional current distribution near the projectile is not accurately known, indications are that this current flow around the perimeter of the rails occurs quite close to the projectile (Marshall 1984). This leads to the conclusion that in the portion of rail in electrical contact with the armature, the current density peak which exists on the rail inside corners ( $s \approx 2$  in Figure 2.2) is probably higher than indicated in Figure 2.2, due to the additional current coming from the top and back surfaces of the rail. In the search for multi-rail alternatives, rail cross-sectional shapes which would aggravate this effect were not considered. In other words, rail shapes with large surface areas on the rail back and top surfaces, i.e., the surfaces of the rails which do not make contact with the projectile, were not considered.

Finally, the ultimate utility of an accelerator was kept in mind -- at least to some degree. This eliminated some more radical geometries and also eliminated the need to consider an infinite number of rail cross-sectional shapes.

### **3.2 Two- and Four-Rail, Square-Bore Railguns**

This section presents current densities, inductance gradients, and forces for selected two- and four-rail railguns so that trends can be identified and appreciated. Only square-bore guns which have rails with rectangular cross-sections are considered. Figure 3.1 shows a square bore with four rectangular rails. The region exterior to the bore and the rails is occupied by dielectric material, which is not shown.

# FOUR-RAIL, SQUARE-BORE GEOMETRY

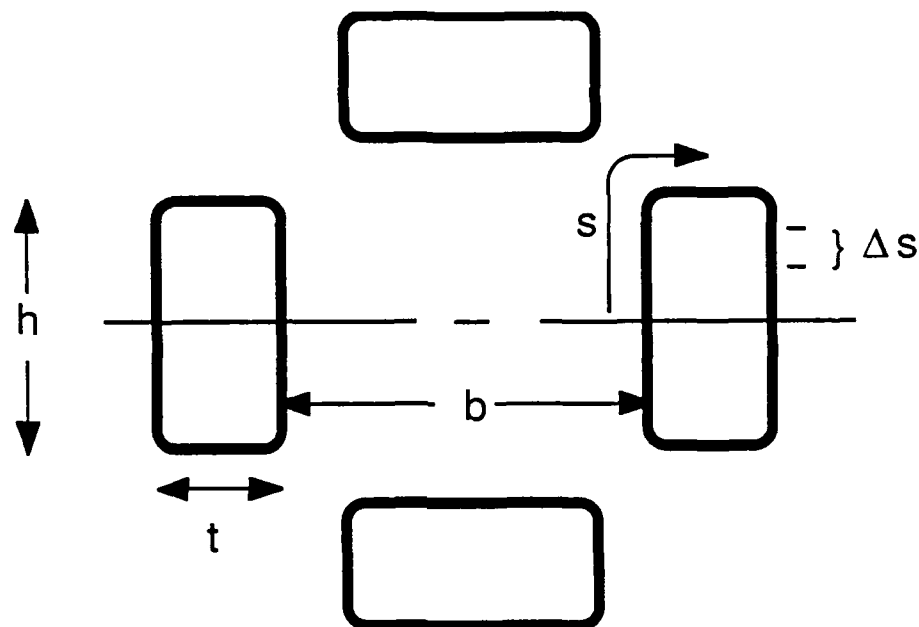


**FIGURE 3.1:** Square-bore, four-rail railgun. Dark lines show the rail cross-section, defining the rail height ( $h$ ), rail thickness ( $t$ ), bore dimension ( $b$ ) and arc length along the rail perimeter. The current in adjacent rails is in opposite directions. All rails have the same cross-sectional shape and all corners are rounded.

Necessary rail containment structures are also not shown. The diagram defines rail height, bore dimension, arc length along the rail perimeter, and rail thickness in the same manner as in Figure 2.1 for a two-rail railgun.

Figures 3.2 thru 3.6 present a group of related current density plots for similar two- and four-rail railguns. All railguns have bore dimensions of 4.0 cm and rail thicknesses of 1.0 cm, although rail heights differ among the plots. All plots depict the current distribution of the top half of the right railgun rail and all position scales have an origin at the inside center of the rails, as was done in Figure 2.2. All scales are identical to facilitate comparisons. The first three plots involve railguns with rail corner radii of 0.1 cm on all corners; the last two plots are for rails with a 0.45 cm radius on all corners. The significant features of these plots deserve some elaboration.

Figure 3.2 shows the current density of a two-rail railgun which has a rail height of only 3.2 cm, i.e., the rail does not completely span the bore. The relative size of the current density peaks at the rail corners, the ratio of rail inside current to backside current, and the general shape of the plot is not very different from that presented in Figure 2.2 in which the rails completely span the bore. Figure 3.3 presents a similar plot for a four-rail railgun with a rail height of only 1.2 cm. Allowing for the smaller rail perimeter, the general shape of this plot is not too different from that of Figure 3.2 or Figure 2.2. This is contrasted with Figure 3.4 in which the rail height is 3.2 cm, so the corners of adjacent rails are considerably closer together. Here, the effect of neighboring currents (the proximity effect)

# NORMALIZED CURRENT DENSITY TWO-RAIL, SQUARE-BORE RAILGUN

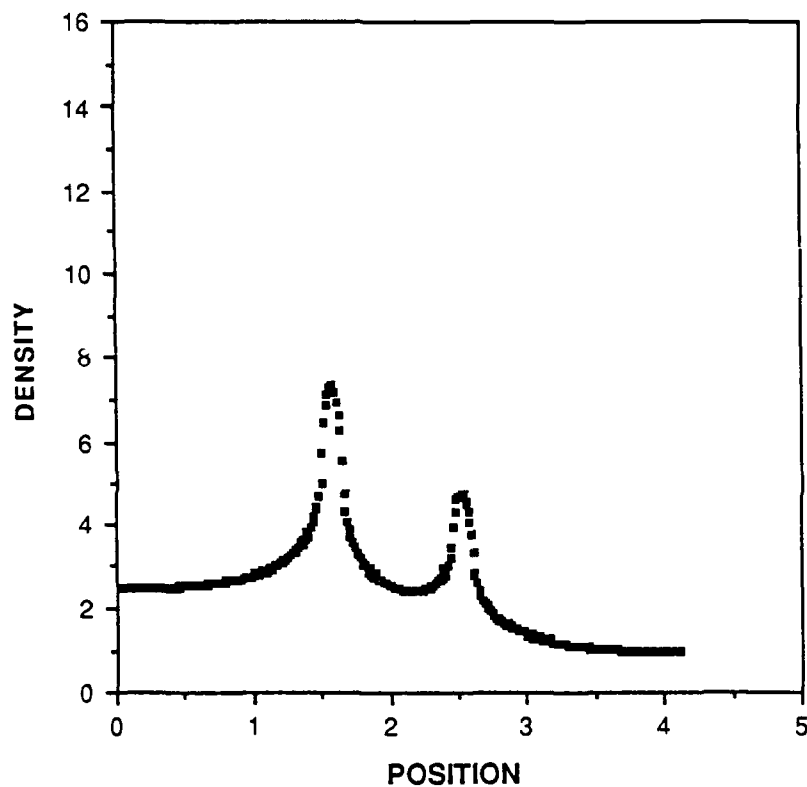


**FIGURE 3.2:** Normalized current density for a two-rail, square-bore railgun. Rail height = 3.2 cm. Rail thickness = 1.0 cm. Bore = 4.0 cm. All corner radii = 0.1 cm.

**NORMALIZED CURRENT DENSITY**  
FOUR-RAIL, SQUARE-BORE RAILGUN

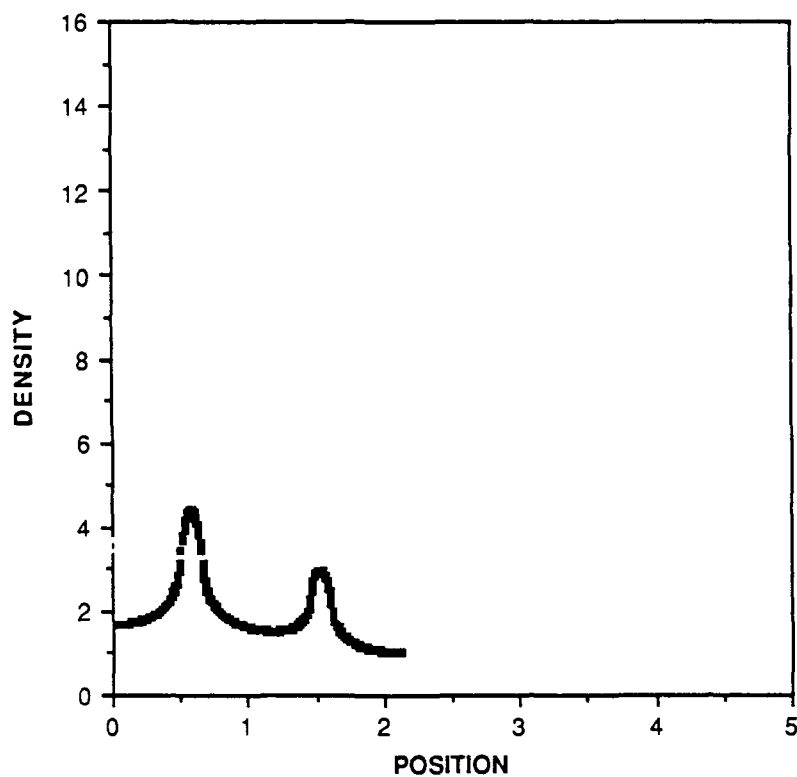


**FIGURE 3.3:** Normalized current density for a four-rail, square-bore railgun. Rail height = 1.2 cm. Rail thickness = 1.0 cm. Bore = 4.0 cm. All corner radii = 0.1 cm.

**NORMALIZED CURRENT DENSITY**  
FOUR-RAIL, SQUARE-BORE RAILGUN

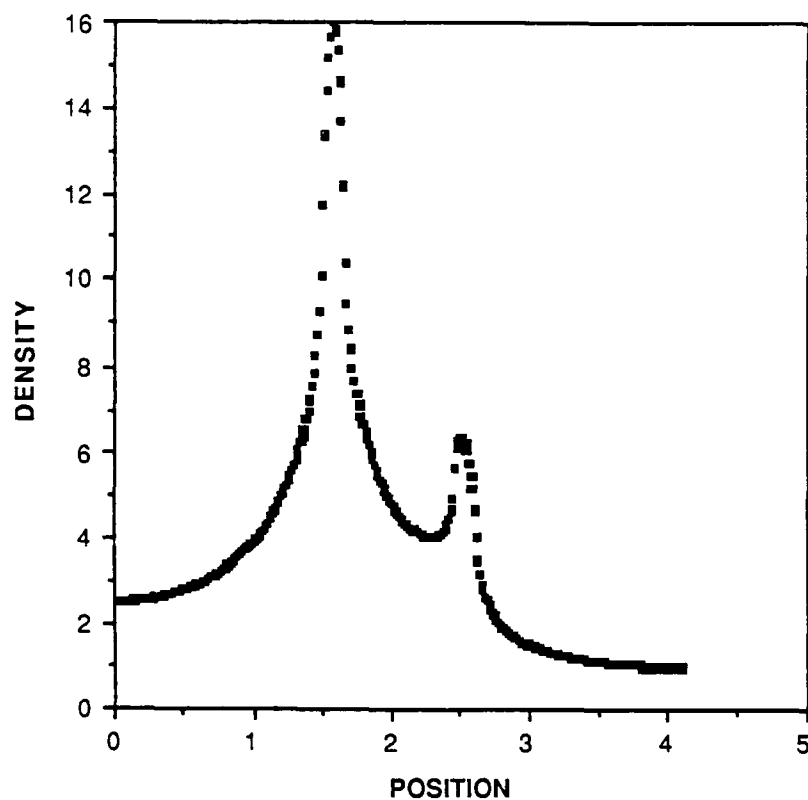


**FIGURE 3.4:** Normalized current density for a four-rail, square-bore railgun. Rail height = 3.2 cm. Rail thickness = 1.0 cm. Bore = 4.0 cm. All corner radii = 0.1 cm.



is very pronounced, as can be seen by the relative magnitude of the current density peak on the rail inside corner (position  $\approx 1.5$  cm in Figure 3.4).

Figures 3.5 and 3.6 display current densities for railguns which have corner radii of 0.45 cm. Since the rail is one centimeter thick, this means that the top of the rail is very nearly a complete semi-circle, with only a one millimeter flat spot. As expected, the peaks which were found on the previous plots have diminished in magnitude and sharpness and have nearly blended together. A current density plot for rails with completely rounded tops (not shown) has indistinguishable peaks that have merged into one smooth hump.

With the current distributions previously shown in this section as a background, the inductance gradients and force-producing capability of accelerators can be presented. The inductance gradient,  $L'$ , of the square-bore, four-rail railgun varies with rail height, as depicted in Figure 3.7. The plot is for railguns with four centimeter bores. Consequently, increased rail height means that a larger percentage of the bore surface is covered by rail and, as shown in Figure 3.4, the proximity effect becomes more dominant. While it would be possible to have a rail height of up to 4.0 cm, the plot only extends to approximately 3.25 cm. For this plot, all rail corner radii are 0.1 cm.

**NORMALIZED CURRENT DENSITY**  
**TWO-RAIL, SQUARE-BORE RAILGUN**

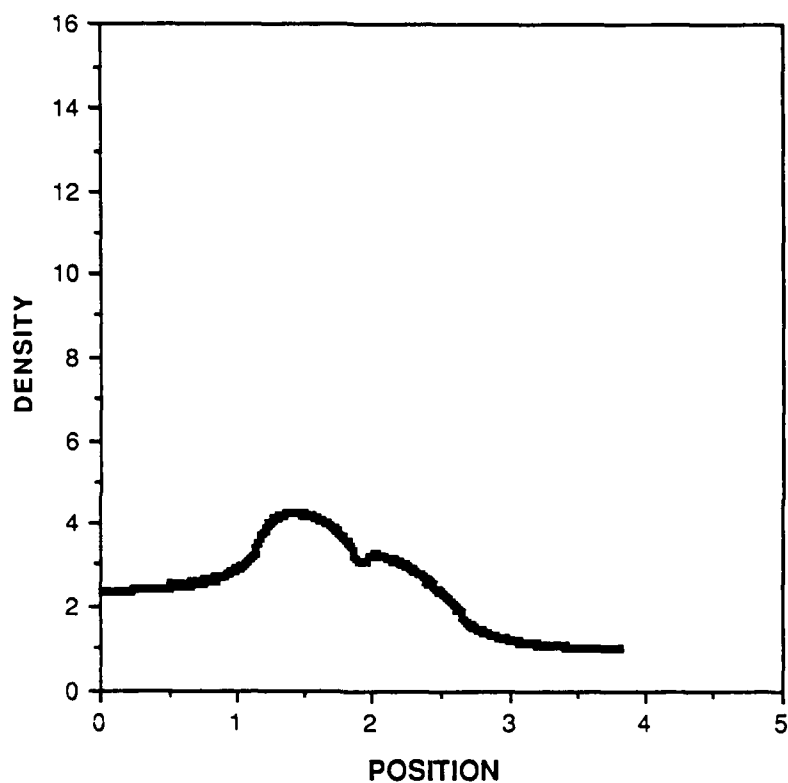


**FIGURE 3.5:** Normalized current density for a two-rail square-bore railgun. Rail height = 3.2 cm. Rail thickness = 1.0 cm. Bore = 4.0 cm. All corner radii = 0.45 cm.

**NORMALIZED CURRENT DENSITY**  
**FOUR-RAIL, SQUARE-BORE RAILGUN**

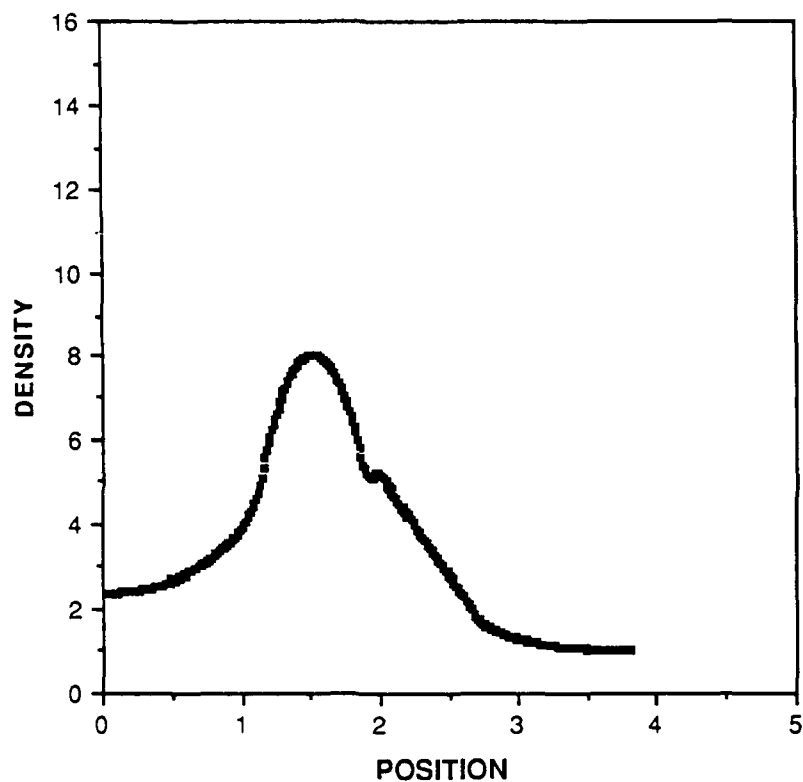


**FIGURE 3.6:** Normalized current density for a four-rail, square-bore railgun. Rail height = 3.2 cm. Rail thickness = 1.0 cm. Bore = 4.0 cm. All corner radii = 0.45 cm.

### INDUCTANCE GRADIENT

#### FOUR-RAIL, SQUARE-BORE RAILGUN

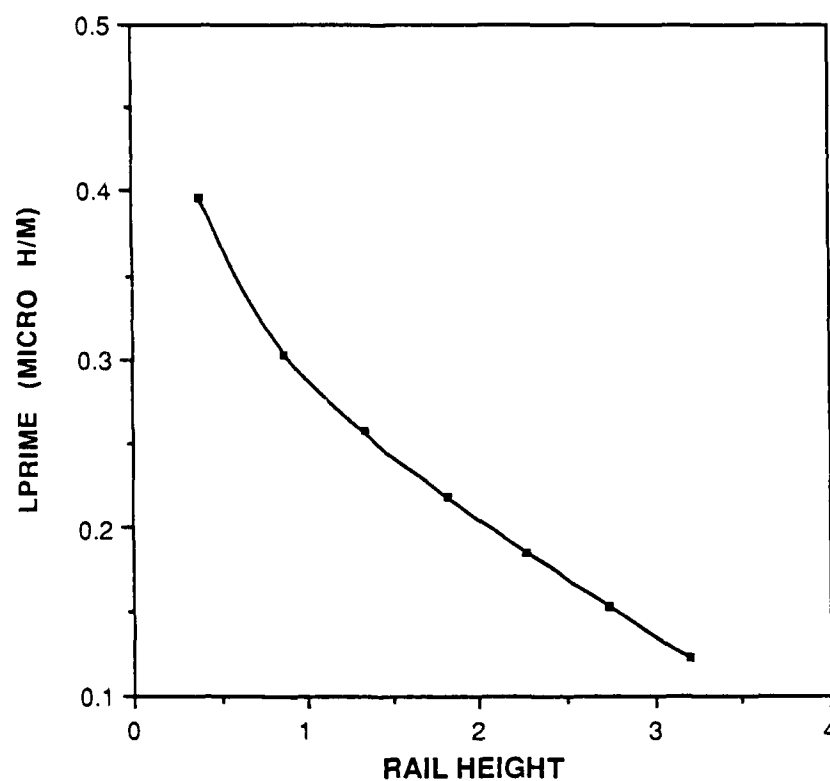


**FIGURE 3.7:** Inductance gradient versus rail height (in cm) for a four-rail, square-bore railgun. Bore = 4.0 cm. Rail thickness = 1.0 cm. All rail corner radii = 0.1 cm.

The effect of variations in current density and inductance with rail height is manifested in the allowable total current and resultant projectile force developed, as shown in Figure 3.8. For these calculations, the peak values of current densities (such as occurred at the inside corners in Figures 3.2 thru 3.6) were fixed at 1.0 MA/inch. Each enlarged dot on the plot represents the current or force, in mega-units, for a square-bore, four-rail railgun. As the rail height of a rail gun is increased, the current-carrying surface of the rails increases and total current initially increases. With a rail height of approximately 65% of the bore, the proximity effect becomes dominant and the result of fixing the peak current density is to actually reduce the total rail current with further increase in rail height. The only way to increase total current for these larger rail heights, is to accept higher peak densities and, therefore, greater rail damage. The effect of the decreasing inductance as rail height is increased (Figure 3.7) is to cause the projectile force to reach its maximum value with a rail height of only approximately 1.5 cm, even though the current has not yet peaked. This maximum force is only approximately 70% of the force developed by a 4.0 cm, two-rail railgun with 4.0 cm rails (the "benchmark" square-bore railgun). Peak current density for the two-rail railgun was fixed at the same level as for the four-rail railgun for this comparison.

### CURRENT AND FORCE

#### FOUR-RAIL, SQUARE-BORE RAILGUN

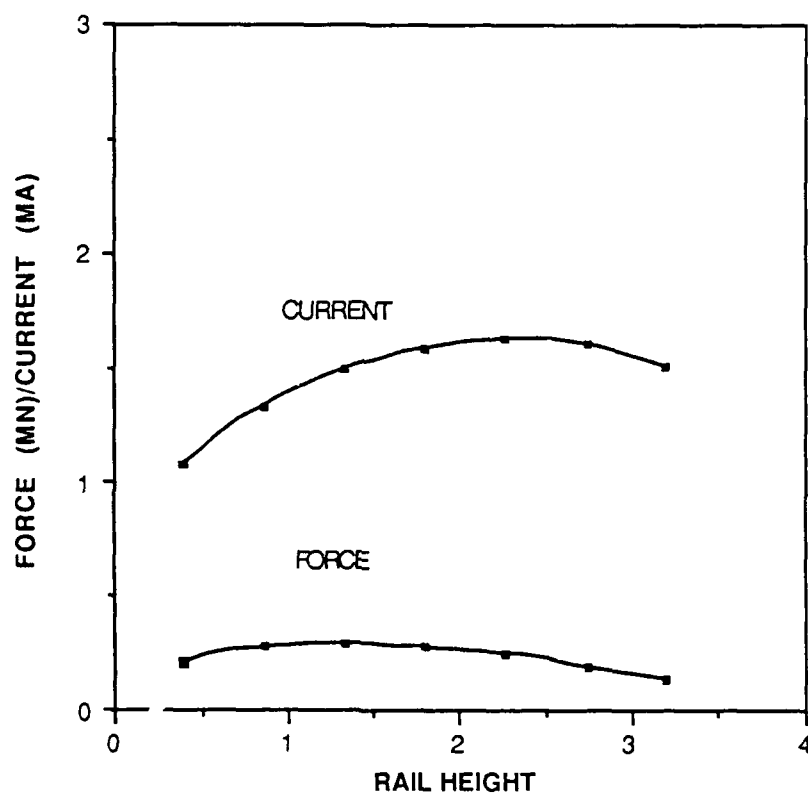


**FIGURE 3.8:** Current and force versus rail height (in cm) for a four-rail, square-bore railgun. Bore = 4.0 cm. Rail thickness = 1.0 cm. All rail corner radii = 0.1 cm.

As previously demonstrated in Figures 3.5 and 3.6, peak current densities can be considerably reduced by using a greater radius of curvature on the corners of the rails. To illustrate the effects of this change, additional plots of inductance gradient, total rail current, and projectile force are provided in Figures 3.9 and 3.10. For these plots, the rail corner radii were increased to 0.45 cm, rail thickness was kept at 1.0 cm, and the bore dimension was kept at 4.0 cm. The results are very similar to that found previously for rails with corner radii of 0.1 cm, except that the current and force curves are shifted upward. This shift is because the current density peaks, which are limited to one MA/inch, are much less sharp than in previous plots, e.g., those for rails with sharp corners. The rail height at which the maximum force occurs is relatively unchanged by the corner radius. As was previously done for railguns with small corner radii, the force produced by the four-rail railgun with large corner radii can be compared with the force produced by a two-rail railgun employing the same large corner radii. Again the four-rail railgun produces approximately 70% of the force produced by the two-rail counterpart. The two- and four-rail railguns have the same peak current densities for this comparison.

### INDUCTANCE GRADIENT

#### FOUR-RAIL, SQUARE-BORE RAILGUN

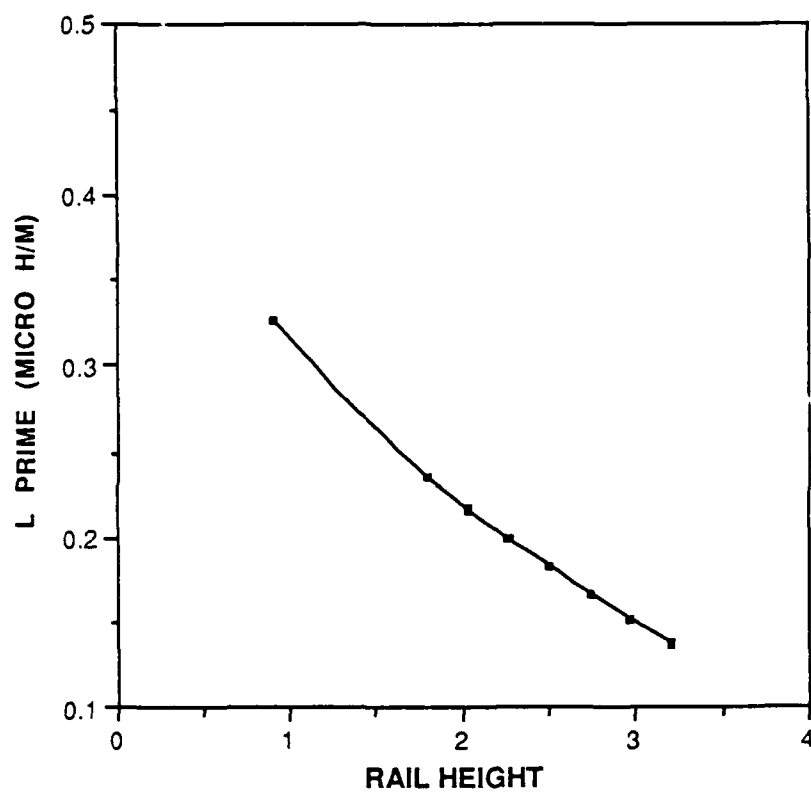


**FIGURE 3.9:** Inductance gradient versus rail height (in cm) for four-rail, square-bore railguns. Bore = 4.0 cm. Rail thickness = 1.0 cm. All rail corner radii = 0.45 cm.



### CURRENT AND FORCE

#### FOUR-RAIL, SQUARE-BORE RAILGUN

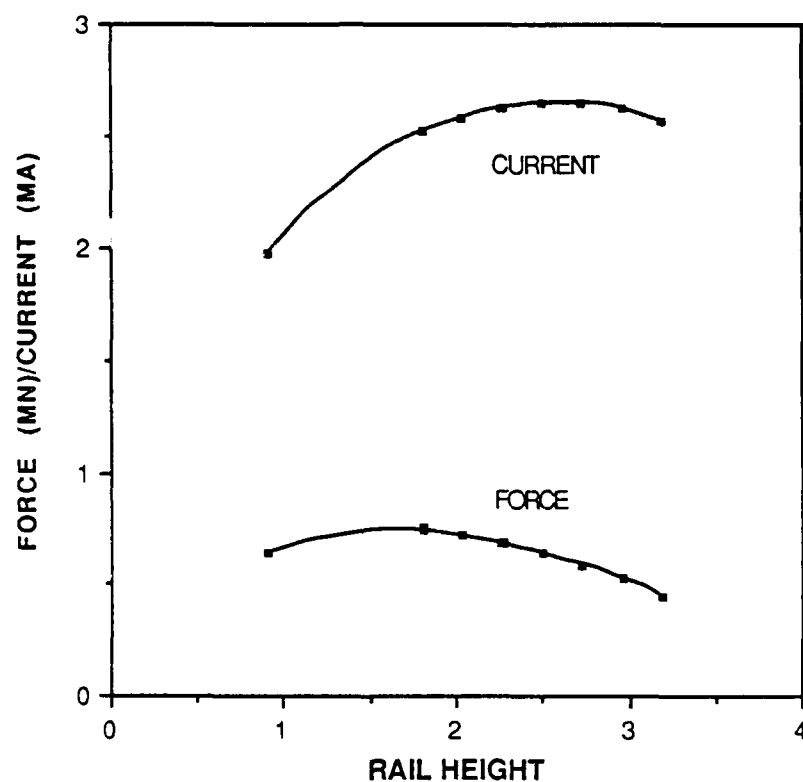


**FIGURE 3.10:** Current and force versus rail height (in cm) for a four-rail, square-bore railgun. Bore = 4.0 cm. Rail thickness = 1.0 cm. All rail corner radii = 0.45 cm.

The results of this section lead to the conclusion that an attempt to improve the distribution of outward rail forces in a square-bore railgun by using four rails with rectangular cross-sections exacts a price. To operate a four-rail, square-bore railgun at the same peak current levels as the two-rail counterpart, a 30% reduction in projectile force must be accepted. Operating at higher peak currents means accepting greater rail damage. Although this section addresses only square-bore railguns, it is apparent that four-rail, round-bore railguns have similar deficiencies. The proximity effect, which was the principle debilitating factor in four-rail, square-bore railguns, is not avoided. Additionally, rail inner corners, where the peak current densities are located, are sharper, i.e., have a smaller included angle, than for the rectangular rail cross-sections.

The factors discussed in the preceding paragraph lead to consideration of alternate, cross-sectional geometries which increase current-carrying surface area -- and total current -- without leading to an aggravated proximity effect. One such geometry involves rails with a triangular, or wedge-shaped, cross-section which creates an X-shaped bore and requires an X-shaped armature. Although an X-shaped armature may seem to have limited utility, this shape may be quite attractive for launching finned, long-rod, armor-penetrating, kinetic energy rounds. Figure 3.11 shows the rail shape and defines the variables of interest. The next section discusses this bore geometry.

## X-BORE GEOMETRY

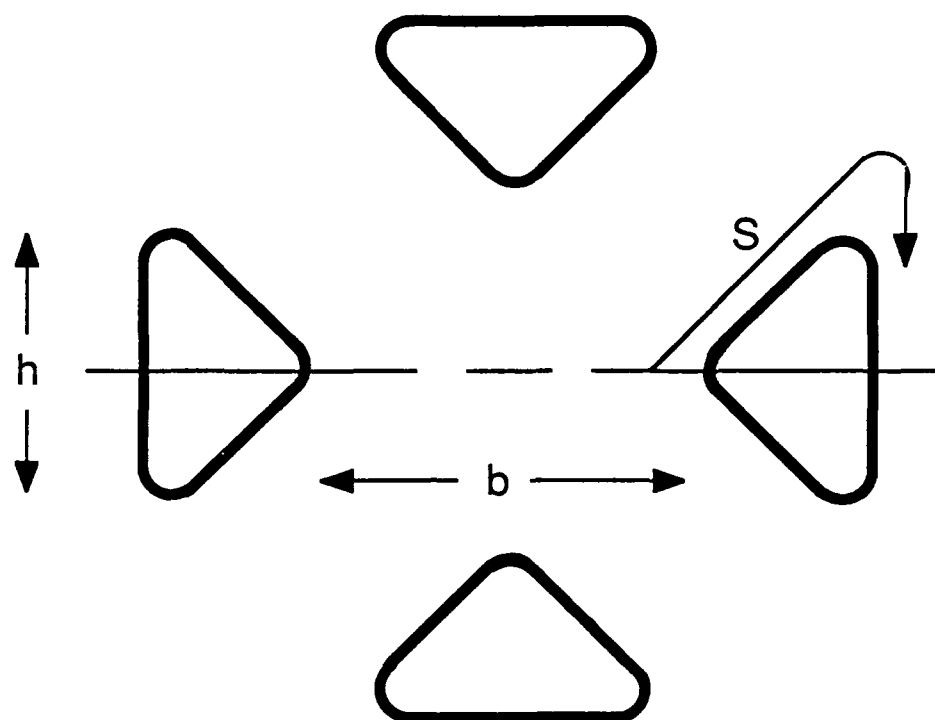


**FIGURE 3.11:** Railgun with wedge or triangular-shaped rails, defining rail height ( $h$ ), bore dimension ( $b$ ) and arc length along the rail perimeter ( $s$ ). The armature is X-shaped, and in contact with the entire length of the two inner sides of each triangular rail. Adjacent rails carry equal and opposite current. The corners are rounded, as they were in the rectangular-rail, square-bore railgun, to avoid current singularities.

### 3.3 Four-Rail, X-Bore Railguns

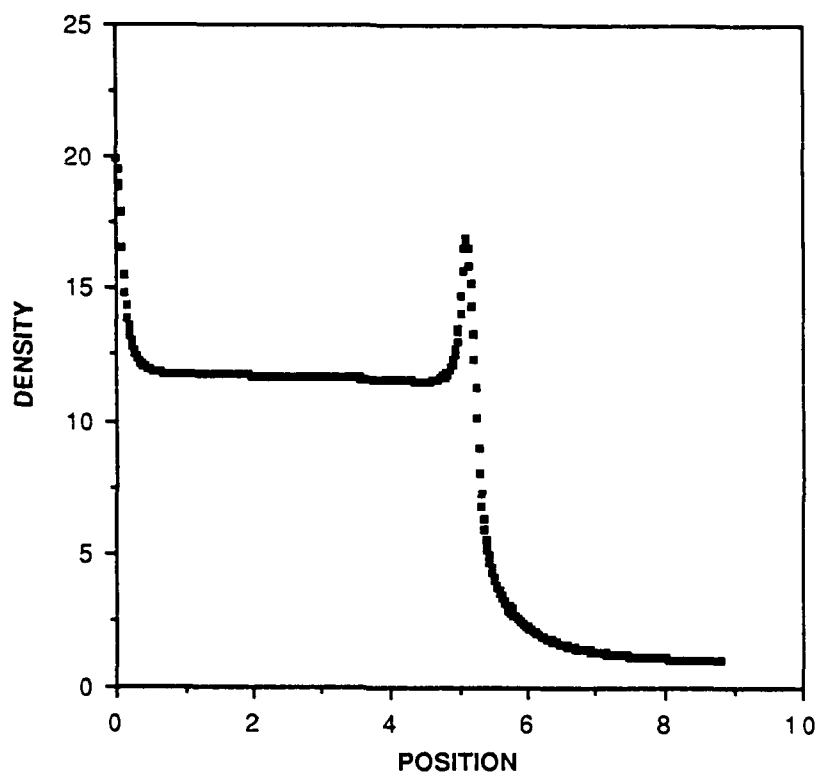
This section presents performance results for X-bore railguns. For these triangular, or wedge-shaped, rail calculations, the three rail corners are rounded with a 0.1 cm radius (Figure 3.11). To allow comparison with the two-rail, 4.0 cm, square-bore railgun results, all calculations are for railguns with a bore area of 16 sq. cm. Consequently, increasing rail height, which increases rail cross-sectional area, requires a reduction in rail separations.

Figure 3.12 shows a typical current density plot for one rail in a four-rail, X-bore railgun. The position origin is at the center of the inside surface of the rail, which places it at the corner of the triangle nearest to the center of the bore. As expected, this is the location of the maximum current density peak. For this particular plot, the rail height is 7.5 cm, which requires a rail separation ( $b$  in Figure 3.11) of 1.03 cm. This provides a cross-sectional bore area of 16 sq. cm. Figure 3.11 is representative of current density plots for X-bore railguns, regardless of the rail height. Interestingly, as the rail height is increased and rail separation is correspondingly decreased, the ratio of peak current density, on the inside corner of the triangle, to current density along the remainder of the inside of the rail, does not change significantly (this holds true for at least the range of rail heights investigated in this dissertation). Therefore, as will be shown later in Figure 3.14, continually increasing rail height causes a corresponding increase in rail total current. In contrast, for the four-rail, square-bore

railguns previously considered, increases in rail height eventually caused an aggravated proximity effect and reduced total rail current (see Figure 3.8).

The X-bore performance parameters are presented in Figures 3.13 and 3.14. Figure 3.13 depicts the variation of inductance gradient with rail height (bore cross-sectional area is still fixed at 16 sq. cm). Figure 3.14 shows the results of current and force calculations for several different rail heights. As rail height increases, projectile force exceeds that of the two-rail, square-bore "benchmark" railgun with a 4.0 cm bore, 4.0 cm rails and corner radii of 0.1 cm. Reviewing the data file for Figure 3.14 reveals that a four-rail, X-bore railgun with a rail height of approximately 4.0 cm produces equivalent force as the two-rail, square-bore counterpart. The bore dimension, (b in Figure 3.11) for this gun is approximately 1.8 cm. In order to provide some perspective, Figure 3.15 provides a drawing of this railgun with approximately a 1:1 scale. For this drawing the rail corner radii, which are 0.1 cm, are not shown. Further increases in rail height produce larger projectile forces and larger rails which are closer together, so the legs of the "X" are longer and thinner. While the X-bore railgun may be useful for launching long rod penetrators, it should be recognized that most of the force on the armature will be concentrated in the legs of the "X". There may be difficulties in accommodating stresses at the base of the legs, which become more severe as the length of the legs is increased.

**NORMALIZED CURRENT DENSITY**  
FOUR-RAIL, X-BORE RAILGUN



**FIGURE 3.12:** Normalized current density for four-rail, X-bore railgun. Rail height = 7.5 cm. Bore area = 16 sq. cm. Corner radii = 0.1 cm.

# INDUCTANCE GRADIENT

## FOUR-RAIL, X-BORE RAILGUN

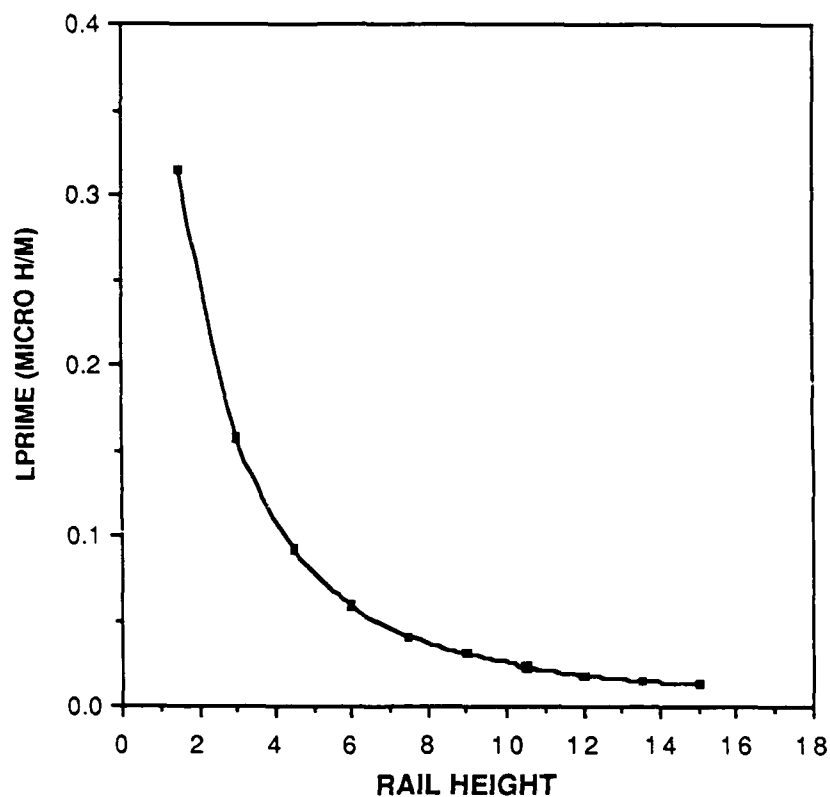


**FIGURE 3.13:** Inductance gradient versus rail height (in cm) for a four-rail, X-bore railgun. Bore area = 16 sq. cm. Corner radii = 0.1 cm.

# CURRENT AND FORCE FOUR-RAIL, X-BORE RAILGUN

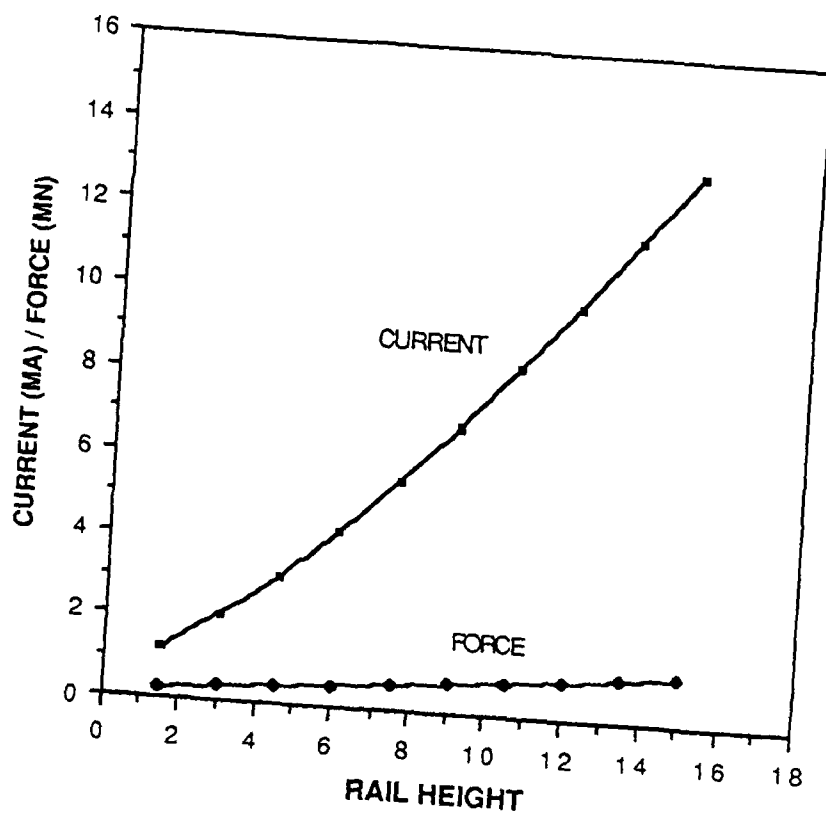


**FIGURE 3.14:** Current and force versus rail height (in cm) for a four-rail, X-bore railgun. Bore area = 16 sq. cm. Corner radii = 0.1 cm.



**X-BORE RAILGUN**  
EQUAL FORCE AS TWO-RAIL RAILGUN

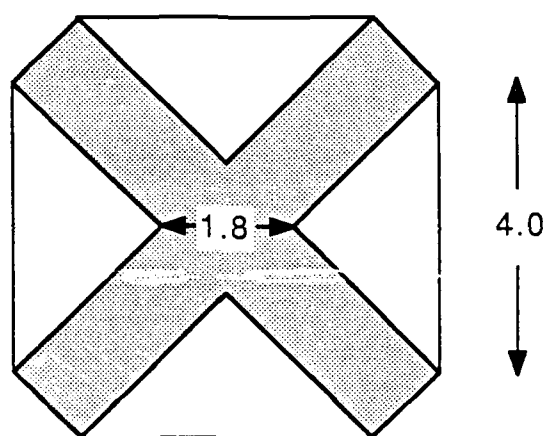


**FIGURE 3.15:** Drawing of X-bore railgun which produces approximately the same force as the "benchmark" two-rail, square-bore railgun. Drawing is full scale, except for slight enlargements or reductions resulting from reproduction processes. Dimensions are in centimeters. The corners of the railgun have a 0.1 cm radii which are not shown. The shaded area is the bore interior and has an area of 16 sq. cm.

The square-bore and X-bore results presented in Sections 3.2 and 3.3 indicate serious drawbacks for multi-rail railguns. Although square-bore, four-rail railguns distribute the outward forces on rails better than two-rail railguns, this advantage is obtained at a cost of a 30% reduction in projectile force. Four triangular rails have a different disadvantage. Although Figure 3.14 indicates that an X-bore railgun can produce more force than its two-rail counterpart -- or it can produce the same force with lower peak current densities -- the bore cross-sectional area is not useful for many types of projectiles.

It is appropriate at this point to briefly mention the results for railguns composed of six triangular-shaped rails, which have bores with six legs instead of four. The plots are not important in the overall development of this chapter and are, therefore, not included. As rail height is increased, the total surface area for the six rails -- and, therefore, total current -- increases more rapidly than with the four-rail railguns. However, in order to maintain a constant bore cross-sectional area with the six legs, rail spacing must be closer than for the four-rail, X-bore railgun. Additionally, the inductance gradient falls off much more rapidly than in the four-rail case (previously shown in Figure 3.13). Therefore, although the total force continues to rise with increased rail height, as did the four-rail case, previously shown in Figure 3.14, it rises more slowly than the four-rail case. The bore geometry very quickly becomes impractical, consisting of six rather long, thin legs.

The key to the better force-producing capabilities of four-rail, X-bore railguns, is that the rail current-carrying surface is increased in a manner which aggravates the proximity effect of

currents in neighboring rails to a lesser degree than in the square-bore, four-rail case. This permits offsetting lower inductances with larger total currents, without increasing local current densities. To increase the bore dimension ( $b$  in Figure 3.11), and improve the railgun utility, rail corners on the bore interior can be rounded or flattened (blunting the apex of the triangle). This leads to consideration of trapezoidal-shaped rails which are discussed in the next section.

### 3.4 Four-Rail Railguns with Trapezoidal-Shaped Rails

This section briefly summarizes results of computations involving many different trapezoidal rail geometries. Figure 3.16 shows the trapezoidal rail geometry and defines the variables of interest. Note that the projectile is in contact with the rail on three sides. This is in contrast to the two- or four-rail, square-bore railguns discussed in section 3.2. Accordingly, the effect of current from the back surfaces of the rail adding to the current peaks on the inside rail corners, as discussed in section 3.1, is less severe than for the square-bore railguns.

From the discussion in the previous section, it is apparent that the goal of rail geometric design is to increase current carrying surface area while keeping peak current densities low. In order to acquire an appreciation for the impact of the trapezoidal geometric variables on the achievement of this goal, results are presented for several combinations of variables. In all cases, the bore cross-sectional area is equal to that of the "benchmark" railgun. Additionally, rail thickness, the distance between the two parallel sides of a rail in Figure 3.16, is fixed

# FOUR-RAIL RAILGUN WITH TRAPEZOIDAL RAILS

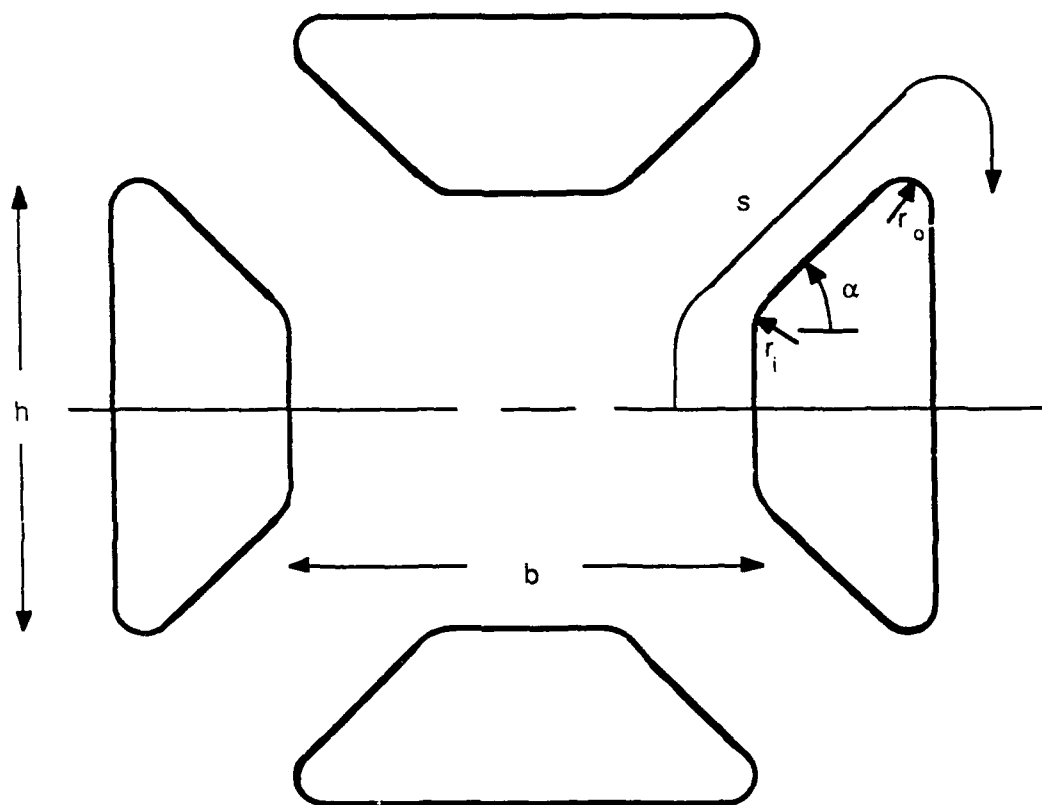


**FIGURE 3.16:** Four-rail railgun with trapezoidal rails. Rail outline is shown, defining rail height ( $h$ ), bore dimension ( $b$ ), rail inside radius ( $r_i$ ), rail outside radius ( $r_o$ ), rail top angle ( $\alpha$ ), and arc length along the rail perimeter ( $s$ ). The armature is in contact with the three inner surfaces of the rails, filling the bore interior.

at 1.0 cm, as for the "benchmark" railgun. This is to avoid progressing toward final designs with long, thin legs, as in the X-bore railgun discussed in the previous section. Peak current densities are again limited to one MA/inch for all force calculations.

Figures 3.17 thru 3.19 each provide a series of curves for a family of railguns. Figure 3.17 shows six plots of force versus rail height for railguns with trapezoidal rails. For all six cases, the inside corner radius is large (0.25 cm) and the outside corner radius is small (0.1 cm). Each curve applies to railguns with different rail top angles ( $\alpha$  in Figure 3.16). The legend identifies the curves with the angle  $\alpha$ , which is expressed as a fraction of  $\pi/4$ . The magnitude of  $\alpha$  places a limit on the minimum rail height possible while still having a 1.0 cm thick rail. In Figure 3.17, for railguns with sharp outer corners, the maximum force produced is for a trapezoidal rail shape with  $\alpha=0.4 \pi/4$ . Figure 3.18 presents similar plots for trapezoidal rail shapes which have both inner and outer corner radii of 0.25 cm and the maximum force is for  $\alpha=\pi/4$ . In Figure 3.18, the maximum force is greater than for the case depicted in Figure 3.17. Figure 3.19 presents the plots for trapezoidal rails which have small, inner corner radii of 0.1 cm and large, outer corner radii of 0.25 cm. Following the trend of the previous two plots, the maximum force for Figure 3.19 is for a rail shape with an even larger angle,  $\alpha=1.2\pi/4$ . These trends are consistent with the inner and outer corner radii associated with each plot and the tendency for current to concentrate at sharp corners. Each maximum force geometry is seen to also be a high-current configuration in which the rail angle,  $\alpha$ , offsets the combined

consequences of sharp corners and proximity effects between neighboring rails, to reduce local current density peaks. Note that Figures 3.17 thru 3.19 each provide numerous railgun alternatives with projectile forces which exceed the 0.393 MN force of the "benchmark" square-bore railgun.

While the previous three sections have been very useful in identifying and understanding trends, it is apparent that a more systematic method of testing geometries in an attempt to reach an optimum is required. The next section, following Figures 3.17 through 3.19, discusses such an optimization process and the results obtained.

# FORCE FOR RAILGUNS WITH TRAPEZOIDAL RAILS FOUR-RAIL RAILGUN

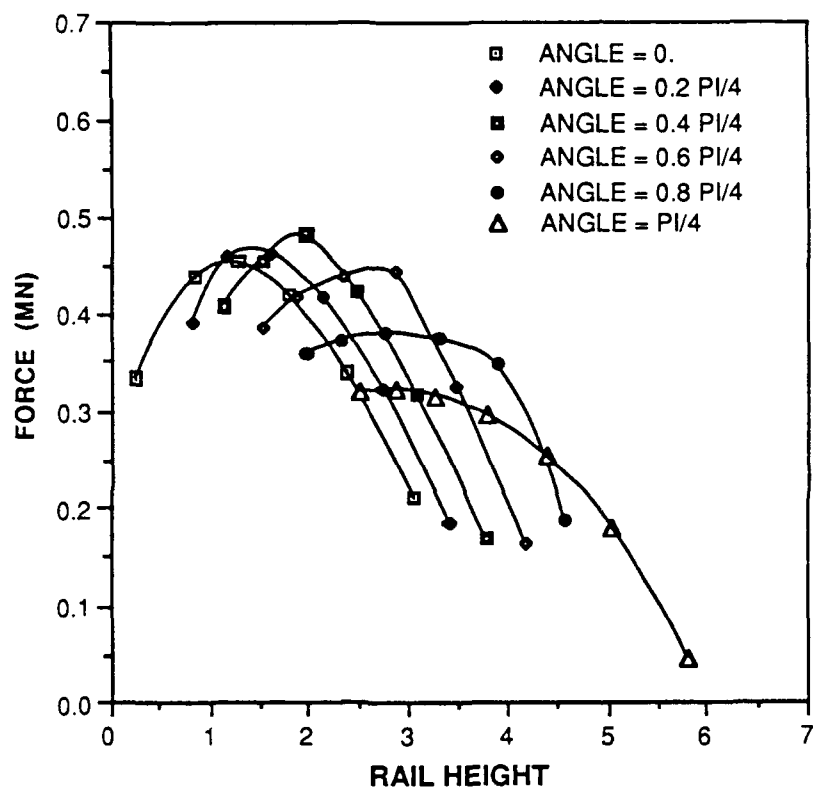


**FIGURE 3.17:** Force versus rail height (in cm) for a four-rail railgun with trapezoidal rails. Bore area = 16 sq. cm. Inside corner radius = 0.25 cm. Outside corner radius = 0.1 cm. Each curve represents the results for a railgun with a different top angle,  $\alpha$ , from Figure 3.16.

# FORCE FOR RAILGUNS WITH TRAPEZOIDAL RAILS FOUR-RAIL RAILGUN

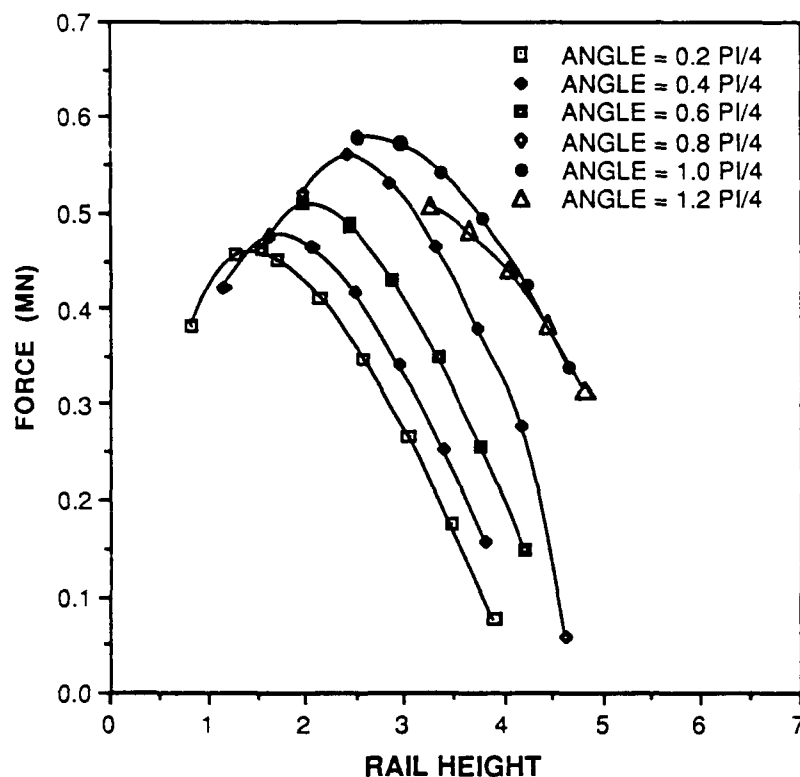


**FIGURE 3.18:** Force versus rail height (in cm) for a four-rail railgun with trapezoidal rails. Bore area = 16 sq. cm. Inside corner radius = 0.25 cm. Outside corner radius = 0.25 cm. Each curve represents the results for a railgun with a different top angle,  $\alpha$ , from Figure 3.16.



# FORCE FOR RAILGUNS WITH TRAPEZOIDAL RAILS FOUR-RAIL RAILGUN

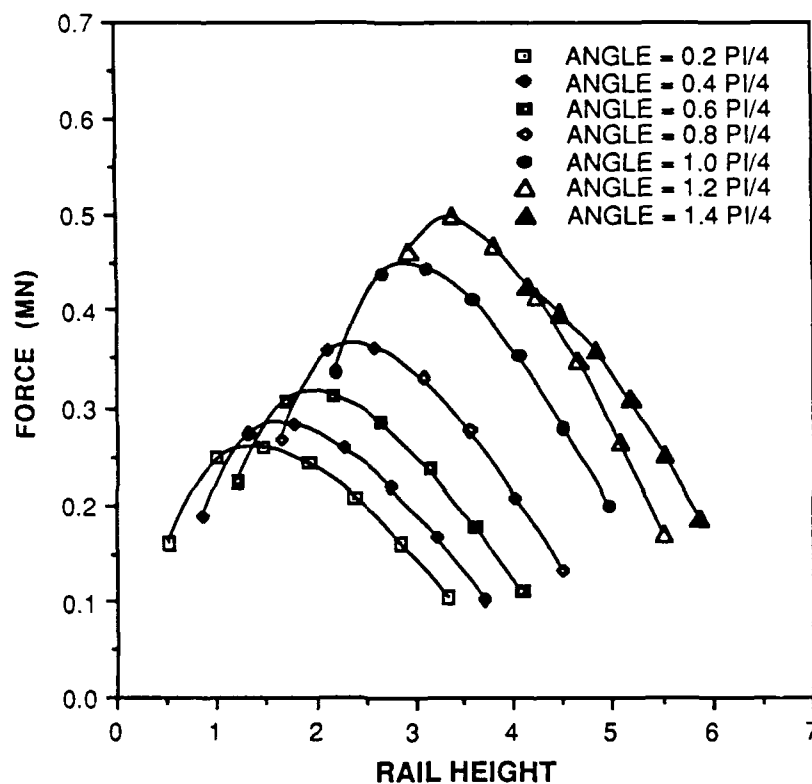


**FIGURE 3.19:** Force versus rail height (in cm) for a four-rail railgun with trapezoidal rails. Bore area = 16 sq. cm. Inside corner radius = 0.1 cm. Outside corner radius = 0.25 cm. Each curve represents the results for a railgun with a different top angle,  $\alpha$ , from Figure 3.16.

### 3.5 Multi-Rail Optimization

This section concludes the search for multi-rail alternatives which improve the outward force distribution of railguns. The results of an optimization study on multi-rail railguns are discussed and several multi-rail railgun designs are presented.

The first step in an optimization study is to determine how to quantify "goodness," which variables are to be optimized to maximize goodness, and what constraints, if any, are to be put on these variables. In accordance with previous sections of this dissertation, accelerator goodness is quantified by the force exerted on the projectile while the rail peak current density is limited to one MA/inch. As before, the bore cross-sectional area is held constant at the sixteen square centimeter value of the "benchmark" railgun, which represents a geometric constraint imposed during optimization. The variables which directly affect the projectile force are the number of rails and the parameters which define rail cross-sectional shape. An appropriate set of geometric variables for optimization is found by noting that the trapezoidal rail shape of Figure 3.16, with appropriate values selected for the variables shown in the figure, encompasses a wide variety of shapes. The possible geometries include, but are not limited to, the triangular and rectangular rail cross-sections discussed previously in this chapter. Therefore, the geometric variables selected for optimization were those of the trapezoidal rail. However, as discussed in the following paragraph, not all the trapezoidal geometric parameters were allowed to vary.

The goal of the optimization study was to find multi-rail alternatives which do not involve the long, thin legs of the X-bore railgun. Therefore, for this optimization, the rail thickness was not allowed to vary and was set to 1.0 cm, which is the same rail thickness as the "benchmark" railgun. Additionally, the outside radius ( $r_o$  in Figure 3.16) was not allowed to vary but was fixed at 0.1 cm, which is the same rail corner radius used in the "benchmark" railgun. Rationale for this restriction is found by considering Figure 3.20. Figure 3.20 illustrates three possible designs for the region of a two-rail railgun where the moving armature, the right rail, and the top insulator intersect. Because this is the region of highest rail current density, it is important to have a close mating between the rail and armature to reduce arcing and rail damage. All three designs in Figure 3.20 have distinct disadvantages and, in all three cases, the disadvantages are made more severe by increasing the curvature of the rail corner. Design "a" has a protrusion on the armature which is difficult to machine. During firing, the protrusion will quickly overheat and erode, causing gaps and arcing. Design "b" has a protrusion in the dielectric material which will also quickly overheat and erode, leaving gaps for arcing and rail damage on subsequent shots. For a plasma armature railgun, these gaps are especially bothersome since they allow plasma to leak by the projectile. Design "c" doesn't suffer either of the shortcomings of "a" or "b," but the rail extends beyond the projectile and beyond the bore area. This lowers inductance and decreases performance. Similar design problems exist for the trapezoidal-rail railgun at the rail outside corners (the location of  $r_o$  in Figure 3.16). Consequently, the rail outside corner

## RAIL CORNER DESIGNS

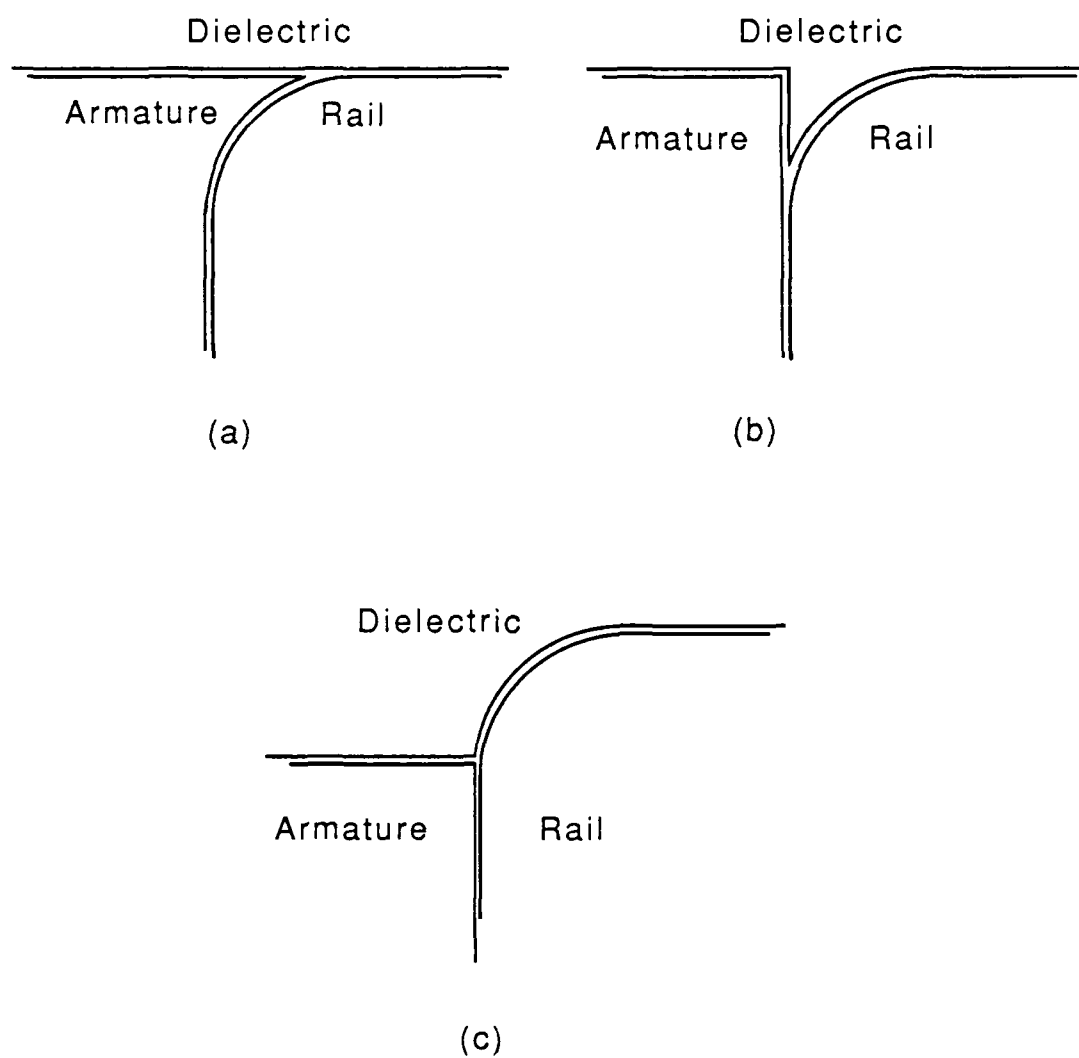


**FIGURE 3.20:** Enlarged views of three possible designs for the intersection of armature, rail, and dielectric material in a railgun.

radius for the trapezoidal rail was fixed at 0.1 cm, which is the same as the rail corner radii on the "benchmark" two-rail railgun. Accordingly, both the multi-rail and the two-rail railgun designs have sharp rail corners at the intersection of rail, armature, and dielectric thereby causing both types of railguns to suffer from the aforementioned engineering problems to a similar degree. This facilitates comparisons between the designs.

Due to the factors previously discussed in this section, the four variables listed below were selected for optimization; the constraints appropriate for each variable are also specified:

- (1) The number of rails -- constrained to be even and greater than two
- (2) The rail top angle ( $\alpha$  in Figure 3.16) -- constrained such that  $0.0 \leq \alpha < 90^\circ$
- (3) The rail inner radius ( $r_i$  in Figure 3.16) -- constrained such that  $0.1 \text{ cm} \leq r_i \leq r_{\max}$ , where  $r_{\max}$  is the maximum radius consistent with the top angle,  $\alpha$ , and the rail thickness
- (4) The rail height ( $h$  in Figure 3.16) -- constrained such that  $h_{\min} \leq h \leq h_{\max}$ , where  $h_{\min}$  and  $h_{\max}$  are the minimum and maximum rail heights consistent with the rail thickness and the rail top-angle,  $\alpha$

The actual optimization procedures used are of interest to some readers so they will be discussed in the next few paragraphs. Since several multi-variable, functional minimization routines are available in references and in the

standard math libraries on most mainframe computer systems, such as the International Mathematical and Statistical Library, (IMSL), it was determined that minimization of the negative of railgun force would be the best approach. Available routines generally require the user to provide a subroutine which calculates the function value when provided with the variable values. The program which had already been developed to calculate railgun force (as discussed in Chapter 2) became the required subroutine. Most available minimization programs also require an initial guess for the set of variable values which will minimize the function. Then, the program searches for a *local* minimum in the vicinity of the initial guess. If the function has several local minima, the answer provided for the optimum set of variables can be sensitive to the initial guess. The final requirement for some minimization programs is the input of expressions for functional partial derivatives. Programs requiring partial derivatives were not considered for use.

The first minimization program tried was available in the IMSL. This routine converged very quickly to a local minimum, which proved to be disadvantageous. Several runs with different sets of initial guesses resulted in very different answers. This revealed the fact that if railgun force, as a function of the four variables picked for optimization, were plotted as a surface in hyperspace, the surface would be quite dimpled, with several local minima. Many of these local minima are caused by interactions of imposed constraints on the optimization variables. To combat this situation, a minimization program which was less sensitive and converged more slowly was sought. The search resulted in a program based on the "downhill

simplex method" contained in Numerical Recipes (Press et.al. 1986; Section 10.4), which worked exceedingly well for this minimization problem. The method requires five initial guesses for a four-variable minimization problem. Then, the optimization program seeks a minimum in the vicinity of the five guesses and in the region of hyperspace defined by the five guesses. Consequently, the program is less easily fooled by local minima, although convergence is slower than the IMSL routine. The reader is referred to the cited reference for further information.

Enforcing constraints on the variables which are to be optimized requires considerable ingenuity for many minimization programs. Since the optimization programs automatically adjust variables in their search for a minimum, they will often select variable values outside the desired range of values. Furthermore, many of the available optimization programs compute numerical partial derivatives in order to assist in selecting the next guess for the optimum variable values. This makes it very difficult to enforce constraints without inadvertently causing an infinite derivative. However, the downhill simplex method does not rely on the computation of derivatives. Constraints are easy to enforce from within the user subroutine which computes the value of the function to be optimized (the routine which computes the negative of railgun force, in this case). The user subroutine merely needs to check the values of the variables, as provided by the optimization program. A large, positive value for the function, i.e., force, is then returned if the variables are outside specified limits. The

optimization program then "knows" that a local minimum was not found using that particular set of variable values.

With this minor diversion into the optimization procedure completed, the results will now be presented. The optimum set of variables produces a railgun which is drawn to scale in Figure 3.21. The railgun has four rails, a relatively large inside radius of  $r_i = 0.612$  cm, a rail height of  $h = 2.40$  cm, and a top angle of  $\alpha = 0.0^\circ$ . The projectile force developed is 0.674 MN, compared with 0.393 MN for the "benchmark" square-bore railgun with small corner radii.

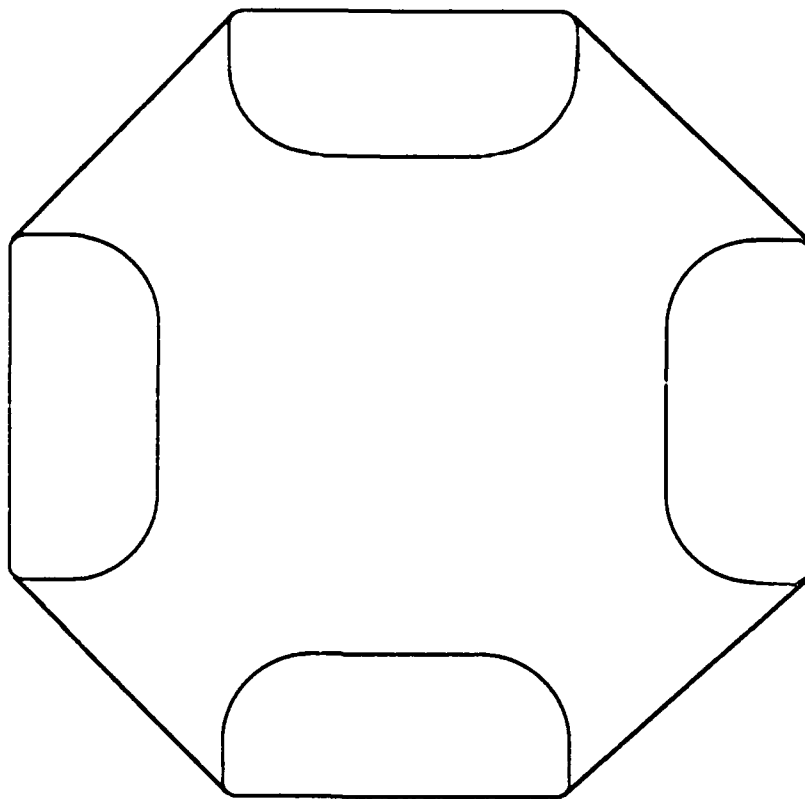
That the optimum number of rails is four (the smallest allowed) is not surprising based on the previous results concerning six triangular-shaped rails. In section 3.3, it was found that four triangular rails were better than six. The magnitude of the rail angle,  $\alpha$ , of zero degrees may seem surprising. However, additional calculations using all the above optimized parameters except the angle  $\alpha$ , which was varied from zero, support this result. Additionally, optimizations using different sets of initial guesses produce the same results.

Figure 3.22, depicting the current distribution for the optimized geometry, provides some understanding of the maximum force geometry. The optimum set of variables offsets the proximity effect -- which would normally be somewhat dominant for four rails with a rectangular cross-section and a rail height of 2.4 cm -- by increasing the rail inner radius. Simultaneously, the current density peaks at the two rail corners are balanced for maximum total current. Now the zero rail angle seems reasonable since a larger angle would produce a



sharper, outer corner and a higher, relative current density spike on this outer corner.

Not apparent from Figure 3.22 is the significance of the 2.4 cm optimum rail height. Although rail height affects the local current density on the inside corner of the rails, an increased height could have been accommodated by increasing the inner radius (the inner radius had not yet reached the maximum permissible value within the geometric constraints of the specified rail thickness and specified outer radius). The quantities most affected by increasing rail height are a decreasing inductance gradient and an increasing total current, due to the increased rail surface area. Therefore, the rail height primarily represents a balancing of total current and inductance gradient to achieve a maximum force.

**OPTIMUM MULTI-RAIL RAILGUN****GEOMETRY:**

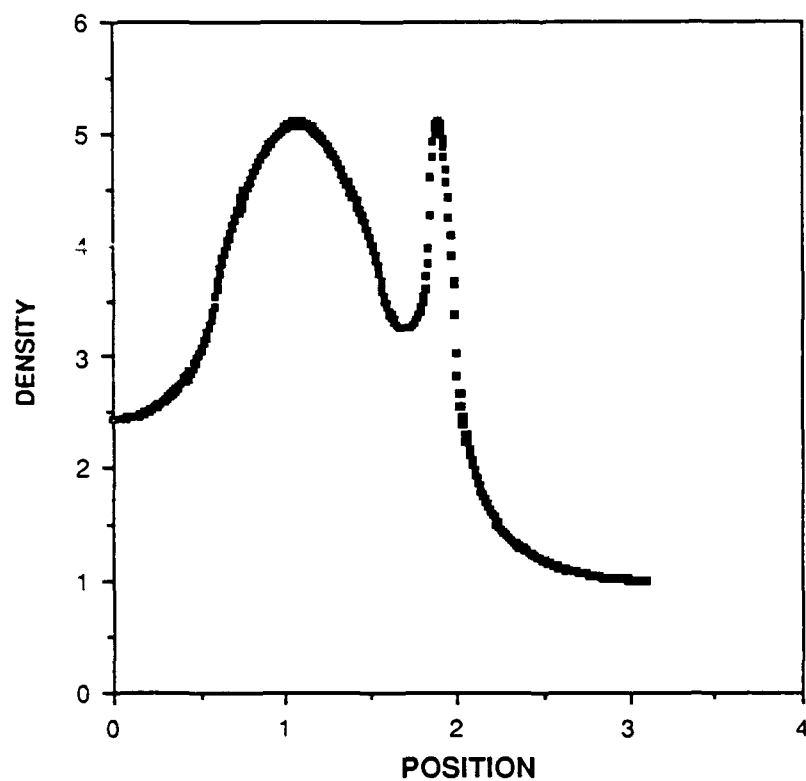
Inner radius = 0.61197 cm  
Outer radius = 0.1 cm  
Rail height = 2.3974 cm  
Bore = 3.4786 cm  
Area = 16 sq cm

**PERFORMANCE:**

Current = 2.834 MA  
 $L' = .168$  micro H/M  
FORCE = .674 MN

**FIGURE 3.21:** A scale drawing of the multi-rail railgun which optimizes force. Scale is approximately 2:1.

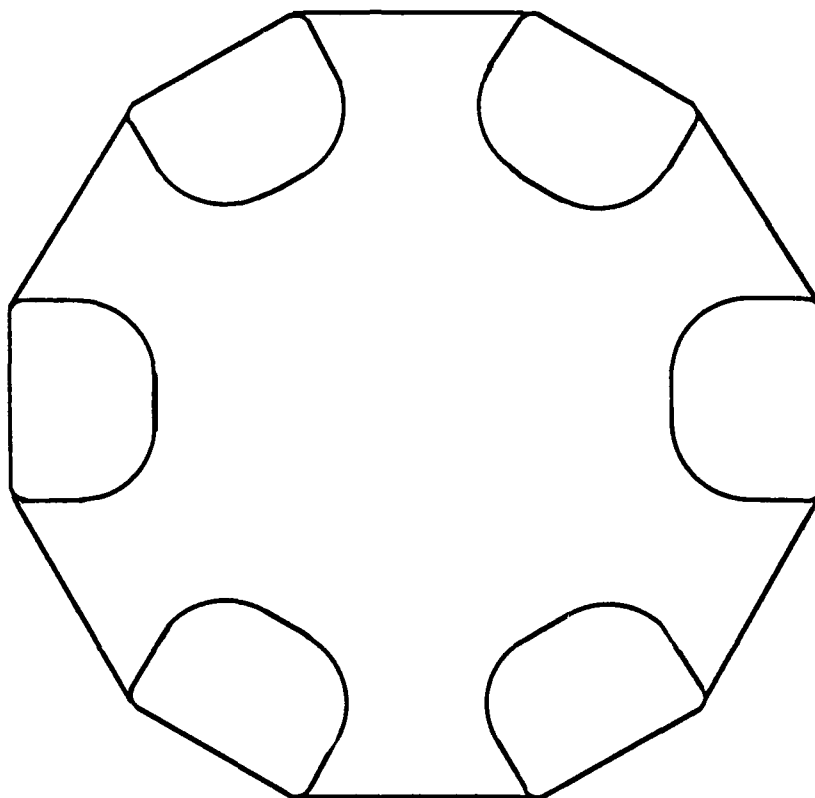
**NORMALIZED CURRENT DENSITY**  
FOUR TRAPEZOIDAL RAILS: MAXIMUM FORCE GEOMETRY



**FIGURE 3.22:** Normalized current density for the railgun of Figure 3.21.

Figures 3.23 and 3.24 are drawn to the same scale as Figure 3.21 and show the results of optimization with the number of rails fixed at six and eight, respectively. Both optimizations result in a railgun which produces less projectile force than the optimum four-rail design. Considering the distribution of the outward forces exerted on the rails, the increase from two to four rails is a tremendous improvement. The increase from four to six or eight rails represents a less significant, incremental improvement at the expense of a somewhat reduced projectile force. But more important than the reduction in projectile force, may be the distribution of the forces on the projectile. Recognizing that the magnetic field in the center of a symmetrical, multi-rail railgun is zero, it is apparent that the projectile force in Figures 3.24 and 3.25 is concentrated more toward the perimeter of the projectile than in the four-rail case of Figure 3.21. For some projectiles, this may be detrimental; for some, it may allow reduction of armature parasitic mass by removal of material from the center of the armature. Finally, Figure 3.26 is the "benchmark" railgun, drawn to the same scale as the other figures. It is provided for convenient comparison.

### OPTIMUM SIX-RAIL RAILGUN

**GEOMETRY:**

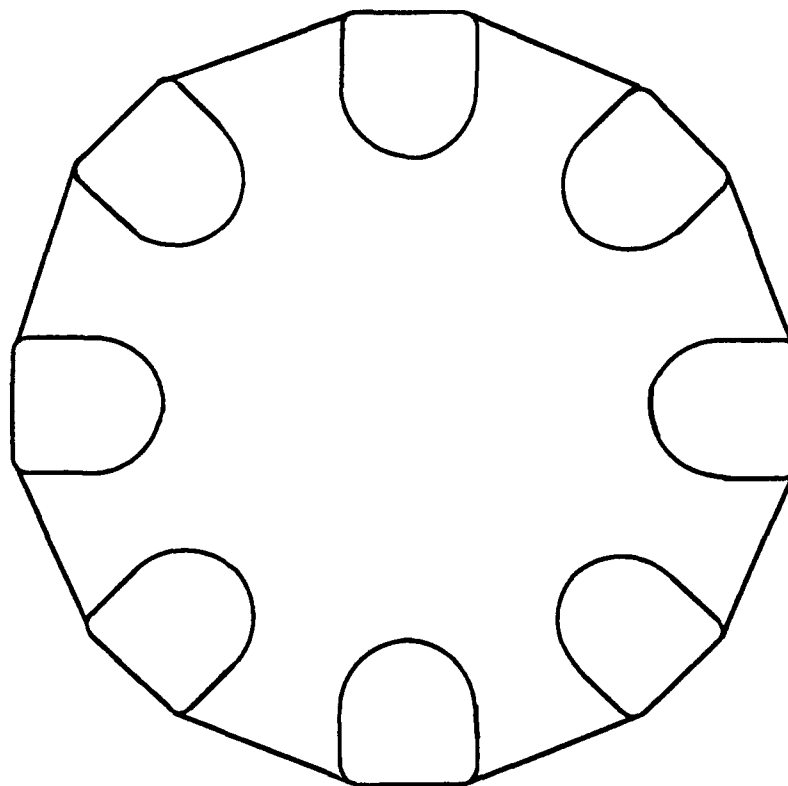
Inner radius = 0.5284 cm  
Outer radius = 0.1 cm  
Rail Height = 1.3755 cm  
Bore = 3.4761 cm  
Area = 16 sq cm

**PERFORMANCE**

Current = 3.342 MA  
 $L' = .108$  micro H/M  
Force = .602 MN

**FIGURE 3.23:** A scale drawing of the six-rail railgun which optimizes force. Scale is approximately 2:1.

### OPTIMUM EIGHT-RAIL RAILGUN

**GEOMETRY:**

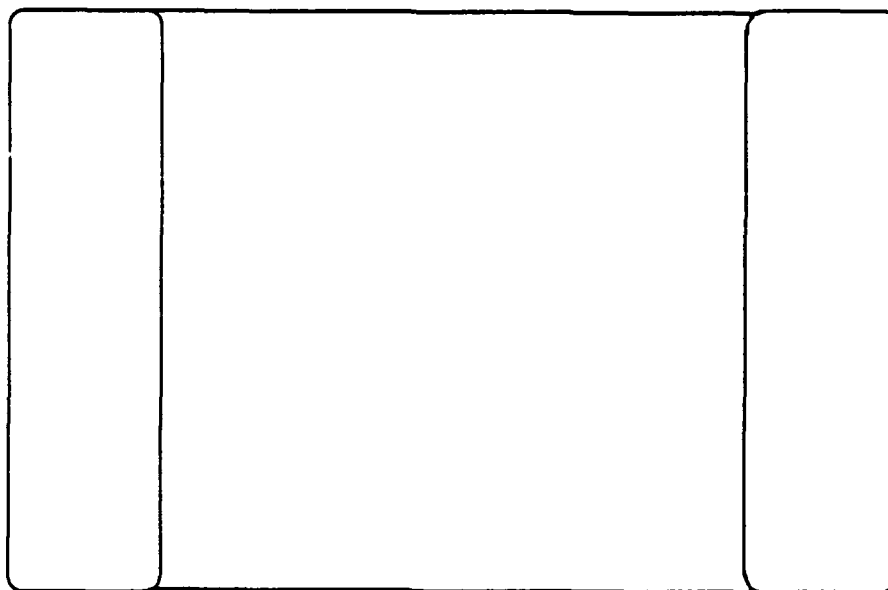
Inner radius = 0.50211 cm  
Outer radius = 0.1 cm  
Rail height = 1.0042 cm  
Bore = 3.2809 cm  
Area = 16 sq cm

**PERFORMANCE:**

Current = 3.920 MA  
 $L' = .0729$  micro H/M  
Force = .560 MN

**FIGURE 3.24:** A scale drawing of the eight-rail railgun which optimizes force. Scale is approximately 2:1.

## TWO-RAIL, SQUARE-BORE RAILGUN



### GEOMETRIC:

Corner Radii = 0.1 cm  
Rail Height = 4.0 cm  
Bore = 4.0 cm  
Area = 16 sq cm

### PERFORMANCE:

CURRENT = 1.225 MA  
 $L' = .525$  micro H/M  
Force = .394 MN

**FIGURE 3.25:** A scale drawing of the "benchmark two-rail railgun. Scale is approximately 2:1.

### 3.6 Chapter Conclusion

The objective of research for this portion of the dissertation was to manipulate the geometry of the current-carrying surfaces of railguns to develop viable alternatives to the conventional two-rail railgun, which do not pose some of the disadvantages of the two-rail railgun. Two alternatives were developed. The four-railed, X-bore railgun distributes outward forces on rails better than the two-rail railgun. Furthermore, it can produce more force than the two-rail railgun or, at least, equal force with lower peak current densities. The X-bore railgun is suitable for finned, long-rod, penetrator-type projectiles, although the stresses at the base of the fins may be difficult to manage. The optimized four-rail railgun of Figure 3.21 also distributes outward forces and develops more projectile force than comparable two-rail railguns. This design provides much more usable space than the X-bore for projectile payload. It also appears to be generally more useful than a square-bore gun -- and nearly as useful as a round-bore gun -- for launching practical projectiles.

The next chapter investigates improvements to two-rail railgun performance which can be obtained by using nearby current-carrying conductors to shape the current distribution in railgun rails.



## Chapter 4

### Active Shaping of Rail Current

#### Chapter Outline

4.1	Introduction. . . . .	86
4.2	Force, Current Distribution, and Inductance Gradient Calculations. . . . .	89
4.3	Current Density Limits on Conductors Other Than the Accelerator Rails. . . . .	97
4.4	Square-Bore Current Guard Plates. . . . .	105
4.5	Round-Bore Railguns: Baseline Performance. . . . .	127
4.6	Force-Optimized Round-Bore Guard Plates. . . . .	135
4.7	Current-Optimized Round-Bore Guard Plates. . . . .	148
4.8	Chapter Conclusion. . . . .	159

#### 4.1 Introduction

This chapter presents results of research seeking to develop techniques for using auxiliary current-carrying conductors to actively shape railgun currents into a more favorable distribution on the rails. A more favorable distribution has reduced peak current densities and generates high projectile forces. In this dissertation, the term "rail" is meant to designate those conductors which are in electrical contact with the armature. The auxiliary conductors are not in contact with the armature (which distinguishes this approach from the multi-rail railguns of previous chapters); therefore,

their current does not increase armature current. The auxiliary currents do, however, produce fields which affect projectile force and the auxiliary conductors are considered part of the accelerator. These accelerators are members of the "augmented" class of railguns.

In this introductory section, the guiding tenets of the study of railguns with auxiliary conductors are discussed. To facilitate comparisons with railguns discussed in previous chapters, the guidelines of this study are nearly identical with those of Chapter 3 (see Section 3.1). In particular, the following guidelines apply:

- (1) Accelerators, including the auxiliary conductors, are studied in isolation from power supplies. It is assumed that power supplies exist to independently drive the rails and the auxiliary conductors with any currents required
- (2) All force calculations, unless otherwise specified, are made with *rail* local peak current densities of one MA/inch. Section 4.3 discusses appropriate local peak current densities for the auxiliary conductors
- (3) All railgun geometries have the same cross-sectional bore area as the "benchmark" railguns, i.e., 16 square centimeters.

The objective of this research was to investigate the potential improvements offered by active current shaping. Therefore, passive current-shaping measures were not applied

to railgun rails. The only railgun geometries studied during this investigation were square-bore and round-bore, two-rail railguns with sharp rail corners (corner radii = 0.1 cm). There are three reasons for limiting consideration to these railgun geometries: 1) the sharp rail corners minimize disadvantages associated with possible designs of the rail-armature-dielectric interface, as discussed with respect to Figure 3.20; 2) the high current density peaks associated with the sharp rail corners present the greatest challenge to active current shaping; and 3) these bore shapes, especially the round bore, are the most useful geometries for launching traditional projectiles, such as larger tactical Army projectiles. Limiting consideration to square-bore and round-bore, two-rail railguns also limits the cross-sectional shapes which must be considered for the auxiliary conductors. The symmetrical rail current distributions found in these railguns result in the need for auxiliary conductors to be symmetrically shaped and symmetrically positioned with respect to the bore center.

Before results concerning the active shaping of rail current can be presented, two additional topics need to be discussed. First, the techniques developed in Chapter 2 to calculate railgun current distributions, inductance gradients, and forces must be extended to include the situations presented by the addition of auxiliary conductors. Second, an appropriate local current density limit for the auxiliary conductors, relative to the one MA/inch limit imposed in the rails, must be established. As will become evident later, the actual magnitudes of the current density limits in the rails and auxiliary conductors are not important for the comparative

studies of this dissertation. Only the relative magnitudes of these current density limits are important. Once these two topics are addressed in Sections 4.2 and 4.3, various results will be presented in the remaining sections of Chapter 4.

#### **4.2 Force, Current Distribution, and Inductance Gradient Calculations**

The objective of this section is to extend the techniques developed in Chapter 2 to include situations presented in this chapter -- which pertain to parallel railgun rails with neighboring, symmetrically positioned, current-carrying, parallel conductors. To aid in this discussion, the railgun with auxiliary current-carrying conductors depicted in Figure 4.1 will be used as an example. Although not necessary for the discussion at hand, it is worth mentioning that the configuration shown in Figure 4.1 is that of a typical "augmented" railgun -- a two-rail railgun with additional "augmenting" conductors. The geometric proportions were chosen to be similar to those contained in the literature (see Kotas, Guderjahn, and Littman 1986, for example). The augmenting conductors are meant to increase magnetic fields in the railgun bore, which increases projectile force without increasing the total rail or armature current. It is common to connect the rails and augmenting conductors in series so that only one power supply is required, although this is not necessary. For generality, it will be assumed that  $i_1$  and  $i_2$  in Figure 4.1 are not equal.

# AUGMENTED RAILGUN GEOMETRY

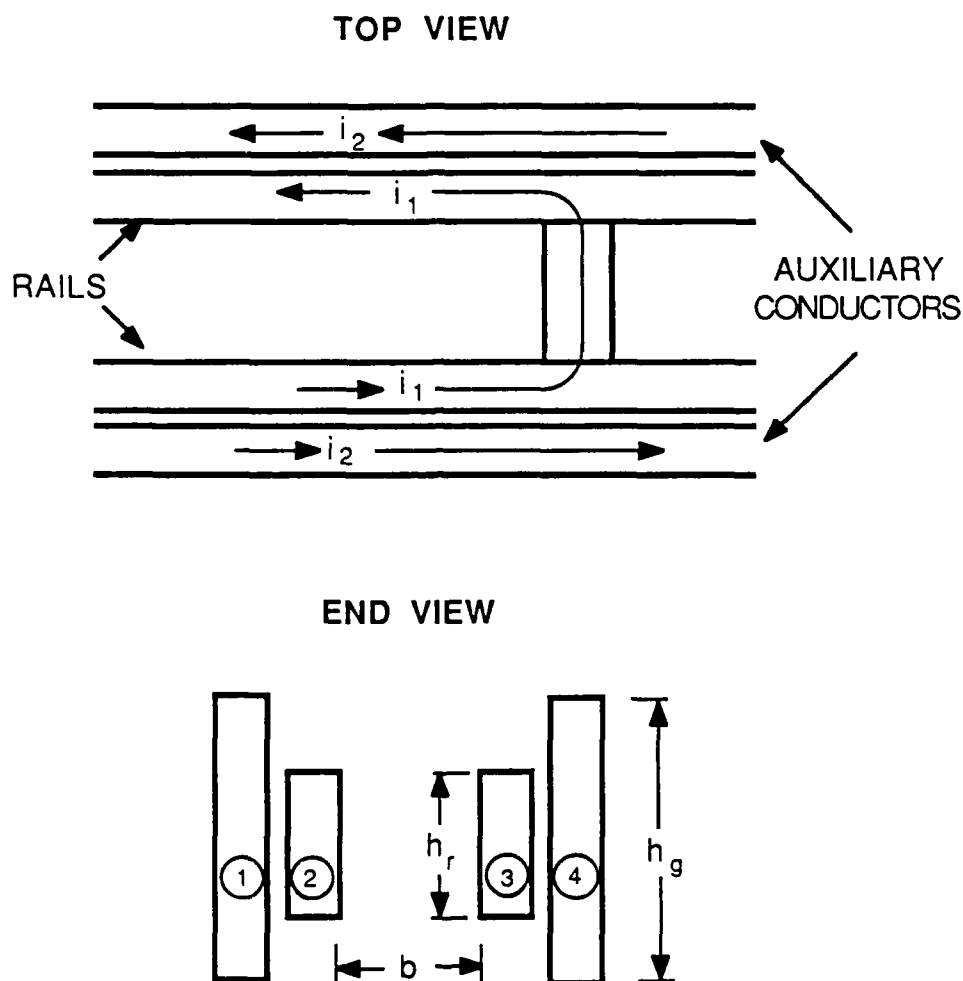


**FIGURE 4.1:** Typical geometry of an augmented, square-bore railgun. Rail and augmenting conductors are shown, defining the bore dimension ( $b$ ), the rail and augmenting conductor heights ( $h_r$  and  $h_g$  respectively), and the direction of current flow in the conductors ( $i_1$  and  $i_2$ ). Conductors are numbered in the end view for future reference.

The first topic in this section will be the force calculation. For this discussion, it is assumed that required current densities for all conductors have been calculated by means similar to those discussed in Chapter 2. Next, the required modifications to the current density calculation of Chapter 2 will be discussed; here it is assumed that the vector potentials for each conductor are known. Finally, the proper specification of vector potentials for each conductor will be discussed.

The force calculation will now be addressed. If the magnetic co-energy,  $W_m$ , is known, the projectile force can be calculated from the equation:

$$F = \frac{\partial W_m}{\partial z} \quad (4.1)$$

This expression proves to be very convenient. Using the methodology of Chapter 2 to calculate current distributions results in a knowledge, at the end of a calculation, of the vector potential,  $\mathbf{A}$ , and line current density,  $\mathbf{J}$ , on the surface of all conductors. The magnetic energy associated with each conductor is then easily calculated by integrating  $\mathbf{J} \cdot \mathbf{A}$  over the conductor surface, as in equation 2.19 which is repeated below:

$$W_m = \frac{\mathbf{A}}{2} \cdot \int \mathbf{J} \, dv = \frac{\mathbf{A}_z \, i}{2} \quad (2.19)$$

For simple two-rail railguns, magnetic energy in front of the armature, i.e., on the muzzle side of the armature, is zero.

In accordance with equation 4.1, force can be taken to be equal to the energy in a unit length of railgun behind the armature, i.e., on the breech side of the armature. In a railgun with auxiliary conductors, such as in Figure 4.1, it is necessary to compute the energy in a unit length of railgun behind the armature, as well as in a unit length of railgun in front of the armature. Force can then be taken as the difference between the two energies.

Calculation of the current distributions on rail and auxiliary conductors will now be discussed. The basic approach to this calculation is the same as in Chapter 2, using the electrostatic-magnetostatic analogy. The surfaces of *all* conducting surfaces are divided into segments,  $\Delta s_m$ , and the potential at the midpoint of each segment is calculated using equations 2.11, 2.13, and 2.14, which are repeated below.

$$V = \sum_{n=1}^N b_{mn} a_n \quad (2.11)$$

where

$$b_{mn} = \Delta s_n \ln \left( \frac{\frac{L}{2} + \sqrt{d^2 + (\frac{L}{2})^2}}{-\frac{L}{2} + \sqrt{d^2 + (\frac{L}{2})^2}} \right) \quad (2.13)$$

$$b_{mn} = 2 \left\{ \Delta s_m \sinh^{-1} \left( \frac{L}{\Delta s_m} \right) + L \sinh^{-1} \left( \frac{\Delta s_m}{L} \right) \right\} \quad (2.14)$$

Equation 2.11, as applied to any particular segment,  $\Delta s_m$ , now includes contributions from all segments,  $\Delta s_n$ , on all conducting surfaces. Again, equation 2.11 is formulated into a matrix equation which is inverted using standard matrix routines. As in Chapter 2, symmetry allows modelling of one quarter of the accelerator geometry. Nevertheless, due to the additional conductors, the size of the matrixes involved for situations of interest in this chapter, are at least twice as large as for the symmetrical, multi-rail cases considered in Chapter 3.

A major additional consideration for the present application is proper specification of the vector potential. This will now be addressed. The vector potential,  $\mathbf{A}$ , (or the analogous electric potential,  $V$ ) is required by equation 2.11 at the midpoint of each segment,  $\Delta s_m$ . As before, because the calculation is for  $z$ -directed, infinitely-conducting conductors, the vector potential has only a  $z$  component, which is constant everywhere in and on the surface of each conductor. An appropriate value for the constant  $A_z$ , must be specified for each conductor before the calculation of current densities can proceed. For the simple two-rail railgun discussed in Chapter 2,  $A_z$  was specified as equal and opposite in the two rails to produce equal but opposite currents on the two rails. Similarly, for the present situation, conductors which are symmetrically positioned with respect to the bore center have equal but opposite vector potentials. This information by itself, however, is not sufficient for the force calculations described at the beginning of this section. It is necessary to specify vector potentials to achieve desired total current flows in certain conductors. For example, the augmented railgun of Figure 4.1



has nonzero net rail current,  $i_1$ , behind the armature (breech side of the armature) and zero net rail current in front of the armature (muzzle side of the armature). Net auxiliary current,  $i_2$ , in front of the armature equals net auxiliary current behind the armature. To calculate the appropriate magnetic energy in front of the armature, it is necessary to specify the ratio of rail and auxiliary conductor vector potentials in this region, such that net current in each rail is zero and net current in the auxiliary conductors is nonzero. These vector potentials -- and resulting currents -- can then be linearly scaled so that net current in the auxiliary conductors in front of the armature is the same as behind the armature, while net rail current remains zero. In general, eddy currents can exist in both rail and auxiliary conductors.

There are two methods of determining the required vector potentials. One approach is to iteratively determine the appropriate ratio of vector potentials to produce the total currents -- or ratio of total currents -- desired on the rail and auxiliary conductors. This computational scheme involves making an initial guess for the vector potentials on each conductor; calculating the current densities and total currents, using the methods of Chapter 2 (based on equations 2.11, 2.13, and 2.14); and adjusting the ratio of potentials by adjusting the vector potential in one conductor, such as the rail. Standard equation-solver routines, such as available in the IMSL, can be used to adjust the vector potentials by solving for the required ratio of vector potentials (which produces a net rail current of zero, for example). Using standard equation-solvers often results in rapid convergence, with only three iterations

required. The reason for the three iterations will become apparent in the following discussion.

The iterative scheme described above is very easy to incorporate in a manner which is applicable to a large class of problems. A second approach, which is more case dependant, is suggested by the electrostatic-magnetostatic analogy<sup>1</sup>. Referring to the end view in Figure 4.1, the conductors are considered as four separate conductors to be treated using electrostatic theory. Numbering the conductors from left to right as one through four and using coefficients of self- and mutual capacitance, the following equations can be written (for a discussion of self- and mutual capacitance for the multi-conductor problem, see Smythe 1950, Sections 2.15-2.16):

$$\begin{aligned}
 Q_1 &= c_{11}V_1 + c_{12}V_2 + c_{13}V_3 + c_{14}V_4 \\
 Q_2 &= c_{21}V_1 + c_{22}V_2 + c_{23}V_3 + c_{24}V_4 \\
 Q_3 &= c_{31}V_1 + c_{32}V_2 + c_{33}V_3 + c_{34}V_4 \\
 Q_4 &= c_{41}V_1 + c_{42}V_2 + c_{43}V_3 + c_{44}V_4
 \end{aligned}
 \tag{4.2}$$

where the  $Q_i$  and  $V_i$  are the charge and electrostatic potential associated with each conductor. The  $c_{ij}$  are the coefficients of capacitance associated with each pair of conductors. The above equations result from linearity and uniqueness properties of the

---

<sup>1</sup>Kerrisk (1981) describes a method of specifying vector potentials for use with his current distribution calculational technique which is equivalent to the method described in this paragraph.

Laplace equation, which governs electric potential in charge free regions. The  $c_{ij}$  are strictly geometric quantities and have the property that  $c_{ij} = c_{ji}$ . Additionally, by the symmetry in Figure 4.1,  $c_{11} = c_{44}$ ,  $c_{33} = c_{22}$ ,  $c_{21} = c_{34}$ , and  $c_{31} = c_{24}$ . Using the electrostatic-magnetostatic analogy, identical equations can be written for four current carrying conductors where the  $Q_i$  are replaced by total conductor currents  $i_i$ , and the  $V_i$  are replaced by the magnetic vector potentials (z components),  $A_i$ . Then two successive computational runs can determine the independent unknown  $c_{ij}$  (which are no longer coefficients of capacitance, but are still geometric parameters). The first run is made with  $A_1$  equal to 1.0 and all other  $A_i$  equal to 0.0. The four currents which are obtained from this computation determine the coefficients  $c_{i1}$ , by substituting into equation 4.2 as follows (since the  $A_{i \neq 1}$  are zero):

$$\begin{aligned}
 i_1 &= (c_{11})(1.0) \\
 i_2 &= (c_{21})(1.0) \\
 i_3 &= (c_{31})(1.0) \\
 i_4 &= (c_{41})(1.0)
 \end{aligned}
 \tag{4.3}$$

Similarly, a second run with  $A_3 = 1.0$  and all other  $A_{i \neq 3} = 0.0$ , yields the two remaining independent, unknown coefficients,  $c_{23}$  and  $c_{33}$ . Once the  $c_{ij}$  are known, appropriate vector potentials required to achieve any desired total current in each conductor,  $i_i$ , can be determined. Now it is apparent why the iterative

scheme of the previous paragraph often only requires three iterations. Most equation solvers solve linear problems in two iterations. A third iteration verifies the solution and, in this case, also calculates the current distribution which is associated with the desired total currents for each conductor (the  $i_j$ ).

#### **4.3 Current Density Limits on Conductors Other Than the Accelerator Rails**

It has already been stated that the purpose of this study is to investigate the potential for using auxiliary currents near railgun rails to actively shape current distributions in the rails. In order to optimize effects, it is necessary to know what maximum current density limits are appropriate for the auxiliary conductors. It has also already been mentioned that the sources of rail-damaging heat during projectile acceleration are: 1) resistive Joule heating from the current in the rails; 2) heat generated across the rail-armature interface due to the contact voltage drop; and 3) friction heating. Since the auxiliary conductors are not in contact with the armature and, therefore, do not suffer the effects of friction and contact voltage drop, it is apparent that larger current density peaks can be sustained on these conductors than on the rails. The objective of this section is to present a simplified thermal analysis so that appropriate current density limits can be set for auxiliary conductors, relative to the current density limit used for the rails. For this purpose, approximate expressions for the heat generated by the primary sources of rail heating are presented. These

calculations are made for a segment of the inner surface of a rail which extends the length of the railgun and has a height along the inner rail perimeter of  $h$ . The expressions developed are for the heat generated per unit height,  $Q/h$ . For a more detailed discussion of thermal issues with solid armatures, see Barber (1986).

Joule heating in the rails can be expressed as:

$$Q_1 = \int_0^{t_f} i^2 R \, dt = \int_0^{t_f} \frac{i^2 (\text{length})}{\sigma (\text{area})} \, dt \quad (4.4)$$

where  $i$  is the total current on the segment of rail, "length" is the length of rail behind the projectile,  $\sigma$  is conductivity, and the "area" is the cross-sectional area of the current carrying portion of the rail. Both the area and length terms are functions of time. The cross-sectional area can be taken as the product of  $h$  and the current skin depth. The skin depth,  $\delta$ , is a function of time. A suitable expression for  $\delta$  is provided by Knoepfel (1970; Eqn 3.32).

$$\delta = \frac{1}{.88623} \sqrt{\frac{t}{\sigma \mu}} = .13217 \sqrt{t} \quad (4.5)$$

where  $t$  is time and  $\mu$  is magnetic permeability. The calculation, which yielded the value of .13217, was done for copper. This skin depth is the magnetic skin depth associated with a conducting half-space when a DC current step is applied. The skin depth is defined such that the total diffused magnetic flux

is equal to surface flux density,  $B$ , multiplied by the skin depth. Now considering the length term in equation 4.4, the length of railgun behind the armature increases with time. For simplicity, the railgun's driving current is assumed to be a step function at time zero<sup>1</sup>. Then the projectile acceleration,  $a$ , is constant and the length term in equation 4.4 is equal to  $\frac{1}{2}at^2$ . Consequently, the heat generated by Joule heating in the rails, per unit height  $h$ , can be expressed as:

$$\frac{Q_1}{h} = \frac{J^2 a}{(2)(\sigma)(.13217)} \int_0^{t_f} t^{1.5} dt \quad (4.6)$$

where  $J$  is the surface current density magnitude ( $J = i/h$ ).

The heat dissipated in the rails as a result of contact voltage between the rails and armature can be approximated by considering an armature with constant velocity and assuming part of the generated heat goes to the rails and the remainder to the armature. Research done by Jaeger (1942), involving uniformly moving sources of heat and resultant temperatures at the contact between a slider and a semi-infinite medium, indicate that the portion of heat absorbed by the semi-infinite medium and the portion absorbed by the slider is velocity dependant. As could be expected, at low velocities (below 20 m/s), approximately 50% of the heat is absorbed by the semi-infinite medium and 50% is absorbed by the slider. At typical

---

<sup>1</sup>The goal of this section is to develop simple equations leading to reasonable approximations. A detailed, more general analysis of current diffusion and Joule heating in rails is provided by Long (1987).

railgun velocities, approximately 75% of the heat generated at the interface is absorbed by the semi-infinite medium. Applying these results to railguns, the heat dissipated in the rails as a result of contact voltage drop can be expressed as:

$$Q_2 = 0.75 \int_0^{t_f} V i \, dt \quad (4.7)$$

where  $V$  is the voltage drop across one rail-armature interface. Expressing the current,  $i$ , as the surface current density  $J$  times  $h$  yields an expression for contact voltage heating per unit height:

$$\frac{Q_2}{h} = 0.75 \int_0^{t_f} V J \, dt \quad (4.8)$$

A reasonable approximation for the voltage drop is to assume it is constant at approximately 75 volts which is typical when the projectile speed exceeds a few hundred meters per second (Barber 1986).

The heat dissipated in the rails from friction can be approximated by again assuming 75% of the generated heat goes to the rails. Then the heat dissipated in the rails can be expressed as:

$$Q_3 = 0.75 \int_0^{t_f} \mu_k F_n v \, dt \quad (4.9)$$

where  $\mu_k$  is the coefficient of friction,  $F_n$  is the normal force exerted by the armature on the rails, and  $v$  is the projectile speed.  $F_n$  can be expressed as magnetic pressure times an area, which yields :

$$F_n = \frac{\mu_o H^2 \text{ Area}}{2} = \frac{\mu_o J^2 \text{ Area}}{2} \quad (4.10)$$

where the second expression results from boundary conditions on the magnetic field,  $H$  (recall that  $J$  is a surface current density)<sup>1</sup>. If an armature similar to that in Figure 4.2 is assumed, the area term in Equation 4.10 is  $\frac{b h \cos\theta}{2 \sin\theta}$ , and the heat generated by friction per unit height,  $h$ , is:

$$\frac{Q_3}{h} = 0.75 \int_0^{t_f} \frac{\mu_k \mu_o J^2 b a t}{4 \tan\theta} dt \quad (4.11)$$

In equation 4.11, velocity was replaced by the acceleration,  $a$ , multiplied by time. A typical value for  $\mu_k$  is .3 or .4 (Craddock et al. 1988).

---

<sup>1</sup>It is common to design armatures so that they must be pressed into the railgun bore. However, normal forces on the rails from this tight fit are usually much smaller than normal forces of electromagnetic origin between the rail and armature during acceleration.



## REPRESENTATIVE ARMATURE DESIGN

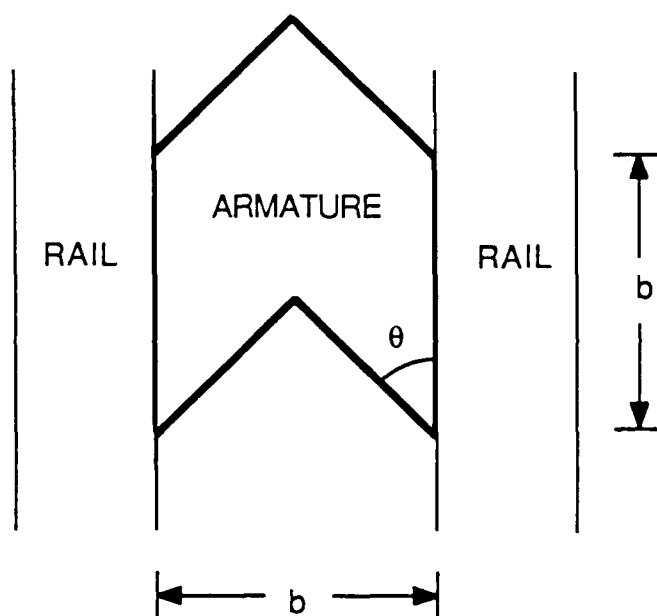


**FIGURE 4.2:** A sample armature for use in estimating frictional losses.

Using the approximations in equations 4.6, 4.8, and 4.11 with some typical railgun data yields approximations for the appropriate relative current density limits for railgun rails and auxiliary conductors. For example, consider a railgun with copper rails which have an imposed limit of one MA/inch, as used in this dissertation. If the railgun has a round bore with a 2.257 cm radius (bore area equals 16 sq. cm), the armature angle is  $45^\circ$  ( $\theta$  in Figure 4.2), and the projectile accelerates at a constant rate to 2000 m/s in approximately 4 feet, then the total heat generated from all three sources of heat, per unit height of rail,  $h$ , is approximately  $1.29 \times 10^7$  (Joules/m). Equation 4.6 indicates that an equivalent amount of heat can be generated by Joule heating alone, with a current density of 1.96 MA/inch. Therefore, if calculations are made using one MA/inch as the peak current density limit for railgun rails, an appropriate peak density limit on the neighboring conductors not in contact with the armature is 1.96 MA/inch. This enables comparisons between different railguns under conditions of similar rail and auxiliary conductor heating. The table below provides the results of several calculations using the same geometrical parameters as in the example just discussed. The conductor material is copper and the peak rail current density is one MA/inch, as above. The table illustrates the effects of the maximum permissible current density in the auxiliary conductors on projectile acceleration.

**TABLE 4.1**  
**CURRENT DENSITY LIMITS**  
**FOR AUXILIARY CONDUCTORS**

Auxiliary Conductor Maximum Current Density	Projectile Exit Velocity	Railgun Length
2.03 MA/in	2000 m/s	1.0 m
1.91 MA/in	2000 m/s	1.4 m
1.82 MA/in	2000 m/s	1.8 m
1.76 MA/in	2000 m/s	2.2 m
1.71 MA/in	2000 m/s	2.6 m
1.67 MA/in	2000 m/s	3.0 m

Although the actual numerical results depend on assumptions and on the railgun under study, the relative ratio obtained for the peak current density on auxiliary conductors to the peak rail current density usually lies between 3:1 and 1:1. The estimates made in this section are undeniably rough approximations, but the results appear reasonable. In the absence of more accurate general guidelines, or until a specific railgun geometry is studied and refined, these estimates are adequate for the comparative studies of this dissertation.

Current density limits for auxiliary conductors, relative to rail current densities, can now be specified. In accordance with the results of this section, force calculations for railguns with auxiliary conductors will incorporate a current density limit of 1.0 MA/inch for railgun rails, as done previously, and successive limits of 1.0, 1.5, 2.0, and 3.0 MA/inch for auxiliary conductors. This provides an appropriate range of data for each accelerator geometry, and avoids the need to accurately model rail-armature heating. Since current distributions on rails and auxiliary conductors are not independent, imposing the two density limits also cannot be done independently. Often, the current distributions are such that the imposition of one limit, on the rails or on the auxiliary conductors, causes the other limit to be automatically satisfied. In these cases, force calculations are based on the more restrictive of the two limits.

#### **4.4 Square-Bore Current Guard Plates**

With sections 4.1 through 4.3 as background, the main topic of current management in rails through the use of active auxiliary conductors can now be addressed. The analogy between charge distribution in a parallel-plate capacitor and current distribution on a pair of parallel conductors, leads to the realization that techniques used in capacitor design to combat high charge densities should have analogous counterparts in railgun design. In particular, the use of capacitor guard rings -- charged conducting rings around the perimeter of a capacitor plate used to lower the charge concentrations at the plate edges -- are common. In order to reduce local peak charge densities on

capacitor plates, guard rings are charged with the same polarity as the capacitor plate they surround. This leads to the concept of adding current-carrying conductors adjacent to railgun rails to reduce rail current density peaks. The rails and adjacent auxiliary conductors have the same "polarity," i.e., they carry current in the same direction.

To investigate the potential improvements offered by using auxiliary currents to influence the rail current distribution, numerous square- and round-bore configurations have been analyzed. Most of this effort was devoted to optimization studies involving round-bore geometries, which have greater utility. These round-bore results are presented in subsequent sections. This section addresses square-bore railguns only, and is intended to illustrate the more salient effects of the auxiliary currents on rail current distribution and on railgun performance.

Several different square-bore accelerator designs were investigated and will be briefly described before proceeding to the design which calculation shows to be the most promising. Auxiliary currents on conductors above and below the rails ("above" and "below" refer to directions with respect to the rail orientation of Figure 1.3) were considered in an attempt to lower the current peaks on the rail corners. Calculations show that the primary effect of this design is to reduce the current density between the two peaks ( $2 < s < 3$  in Figure 2.2), while leaving the peaks themselves and the amount of current on the rail back surface relatively unchanged. Similarly, adding conductors behind the rails, as in Figure 4.1 which represents the usual design for augmented railguns, reduces backside rail

current but does not reduce current density peaks on rail inside corners. Nevertheless, this design is very common and is discussed in a later paragraph. This leads to consideration of the wrap-around design of Figure 4.3, which is shown with exaggerated sizes to allow room for labeling. This shape was found to be most useful for influencing rail current density peaks and rail back surface currents; it is discussed in considerable detail later in this section. For the wrap-around design, a fully diffused (DC) current is less beneficial than a pulsed current. If the auxiliary conductors are driven in a pulsed mode (as would be the case for conductors connected in series with the rails, for example), the auxiliary current density peaks are located in those places where they have the most effect on the rail peak current densities. Consequently, only pulsed auxiliary conductors will be considered in this dissertation.

To facilitate discussion, it is useful to define terms to identify certain accelerator configurations. The term "augmenting" will refer to the common design in which the auxiliary conductors are positioned behind the rails, as in Figure 4.1. The wrap-around conductors of Figure 4.3, which are analogous to capacitor guard rings, are designated as current "guard plates" or "guard rails."

Before discussing wrap-around guard plates, it is of interest to present some performance results for the common augmented railgun of Figure 4.1. Current density plots for the rails and the augmenting conductor, often referred to as the augmenting "turn," are presented in Figures 4.4 and 4.5. Results presented are for a railgun identical to the "benchmark" square-bore railgun, with the exception that augmenting conductors are

## SQUARE-BORE GUARD PLATES

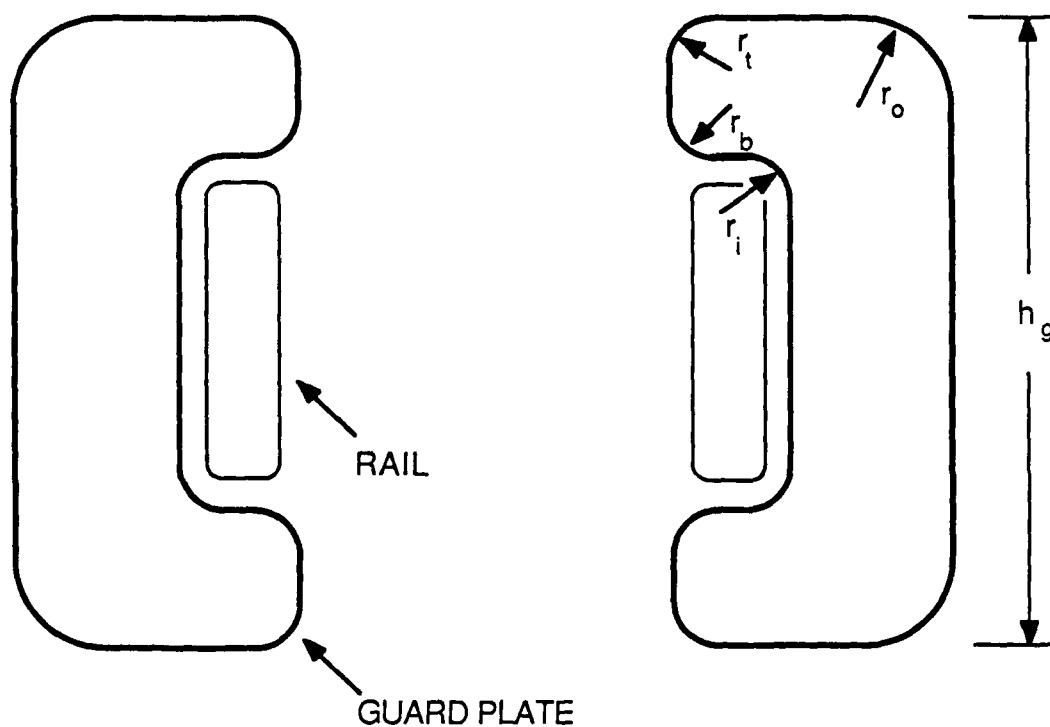


**FIGURE 4.3:** "Benchmark" square-bore railgun with the addition of wrap-around guard plates. Rail variables are the same as defined in Figure 2.1. This figure defines the guard plate height ( $h_g$ ), the top radius ( $r_t$ ), the bottom radius ( $r_b$ ), the inner radius ( $r_i$ ), and the outer radius ( $r_o$ ). Guard plate size has been exaggerated to allow room for labels.

added in the manner of Figure 4.1, i.e., referring to Figure 4.1,  $b = 4.0$  cm,  $h_r = 4.0$  cm,  $h_g = 8.0$  cm, and conductor thickness = 1.0 cm. Separation between the rails and augmenting turn is two millimeters to allow for insulation. For these current density calculations, the ratio of rail to augmenting conductor vector potentials was adjusted so that the rail and augmenting total currents are equal; this corresponds to the common series connection for augmented railguns. Figure 4.4 depicts the rail current distribution for this augmented railgun. To see the effects of auxiliary (augmenting) currents on the rail current, compare Figure 4.4 with Figure 2.2, the current density plot for the "benchmark" railgun without augmenting conductors. The reduction of the rail back surface current ( $s > 3$ ) is very apparent and the current density peak on the rail back corner is nearly eliminated. However, there is little effect on rail top or front surface current. In fact, the ratio of the rail current on the middle of the front of the rails ( $s=0$ ) to that on the inside corner ( $s=2$ ) is relatively unchanged. Figure 4.5 presents the augmenting current distribution. Here it is seen that a negative (eddy) current is induced on the portion of the augmenting turn adjacent to the rail and that this current is quite small. As will become apparent in other plots contained in this dissertation, small, negative, induced current densities on rails or guard plates are common. Which conductor, if any, has the negative current depends on the relative magnitudes of vector potentials and the accelerator geometry. It should be noted that figures 4.4 and 4.5 indicate that rail and augmenting currents both have approximately the same maximum, normalized peak current density ( $\approx 35$ ). Therefore, the maximum current density on the



rail and augmenting turn were both assigned magnitudes of approximately one MA/inch when making force calculations. For these calculations, all conductor corners have radii of 0.1 cm. Performance parameters, compared with the nonaugmented, "benchmark" two-rail railgun follow:

**TABLE 4.2**  
**AUGMENTED, SQUARE-BORE RAILGUN PERFORMANCE**

Parameter	Augmented Railgun	Nonaugmented Railgun
Rail Current	0.961 MA	1.224 MA
Force	0.543 MN	0.393 MN
Inductance Gradient	1.175 $\mu\text{H/m}$	0.525 $\mu\text{H/m}$

Two observations concerning these performance parameters deserve mention. First, the inductance per unit length is an effective quantity calculated from the force and current numbers. It is meaningful in this situation because the rail and augmenting conductors have identical currents. Second, the usual attractiveness of an augmented railgun is that force can be increased while keeping the same total rail current. Using this approach, it is normal to compare the nonaugmented force with the force which could be obtained with the augmented railgun when operated with the same total rail

**NORMALIZED RAIL CURRENT DENSITY**  
TWO-RAIL, SQUARE-BORE, AUGMENTED RAILGUN

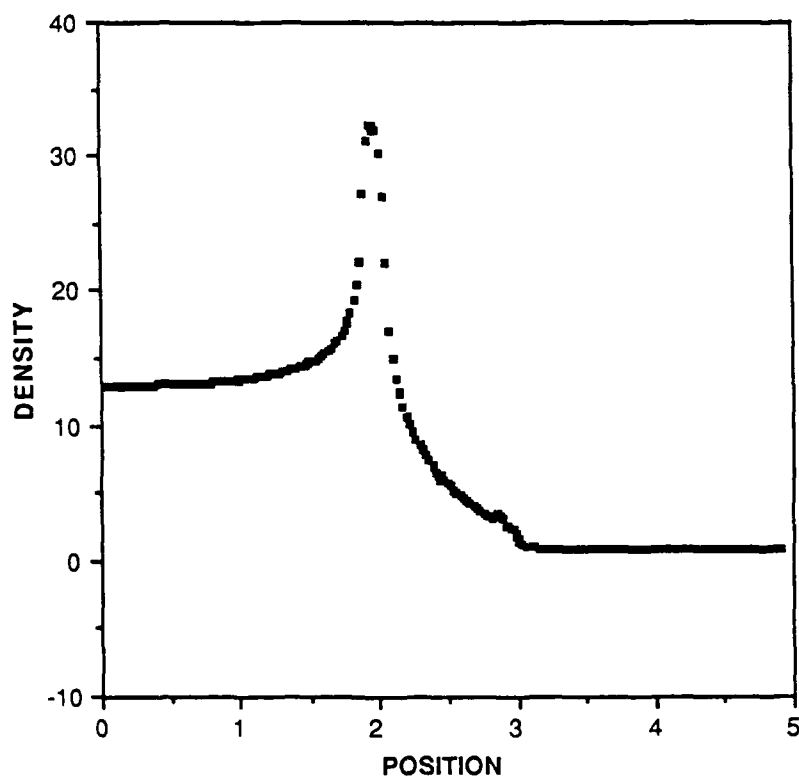


**FIGURE 4.4:** Normalized rail current density for a two-rail, square-bore railgun with the augmenting turn of Figure 4.1. Referring to Figure 4.1,  $b = 4.0$  cm,  $h_r = 4.0$  cm, and  $h_g = 8.0$  cm. The rail and augmenting conductors are both 1.0 cm thick and the separation between the rail and augmenting turn is 2.0 mm. The plot is normalized so that the current density is 1.0 on the center of the back of the rail (position  $\approx 5.0$ ). All conductor corners have a 0.1 cm radius.

# NORMALIZED AUGMENTING CURRENT DENSITY

TWO-RAIL, SQUARE-BORE, AUGMENTED RAILGUN

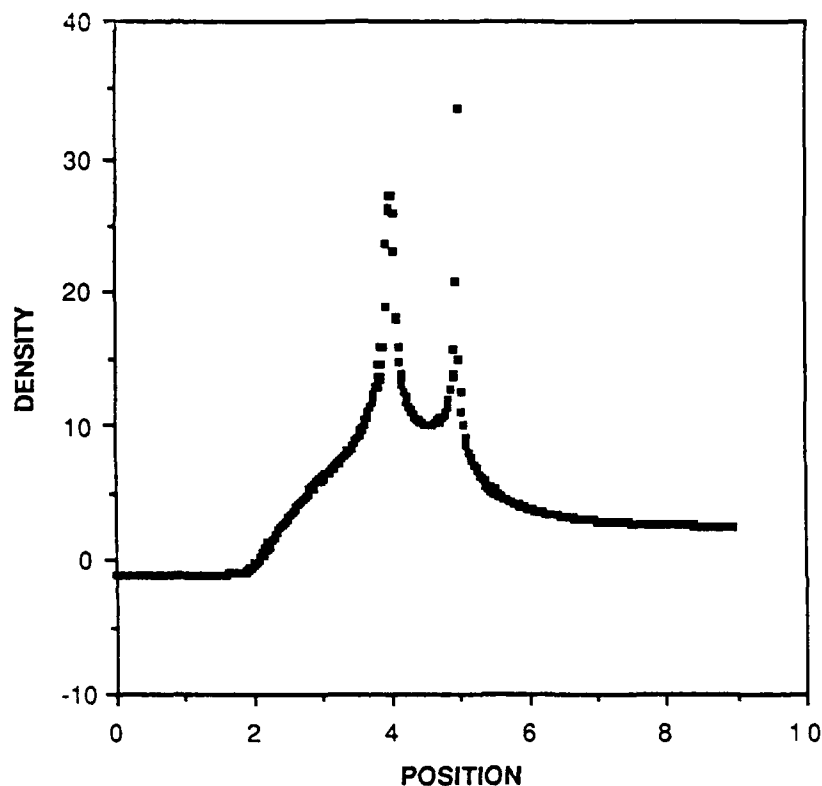


**FIGURE 4.5:** Normalized current density for the augmenting turn of the railgun shown in Figure 4.1. This plot is the companion plot of Figure 4.4 and is normalized by the same normalizing factor. As for rail current density plots, this plot is for the top half of the right augmenting conductor. The position axis is similar to that for the rail conductors, with the origin corresponding to the center of the inside of the augmenting conductor. Position proceeds around the top of the conductor, ending at the center of the back surface. The scale on the position axis is different than that in Figure 4.4, due to the increased perimeter of the augmenting conductor.

current as for the nonaugmented gun. In this case, if the augmented gun were operated with the total current of 1.224 MA (see Table 2.1), the force would be 0.880 MN. However, due to changes in rail current distribution imposed by the augmenting conductors, this would result in local peak current densities higher than previously allowed in this dissertation.

Having discussed results for the common augmented railgun, the wrap-around guard plate design will now be considered. Figures 4.6 through 4.9 form a sequence which illustrates the effectiveness of wrap-around guard plates in influencing rail current distribution and the relative importance of various guard plate geometric parameters. The plots and diagrams have been reduced so that the accelerator diagram and corresponding current density plots fit on one page for viewing convenience. Most variables are identical for all four figures, so that comparisons can be made. In all four figures, the rail geometries are identical to those of the "benchmark" two-rail, square-bore, railgun (bore = 4.0 cm), so the rails have sharp corners with 0.1 cm radii. In all cases, vector potentials of the rails and guard plates behind the armature are equal; this generally results in unequal guard plate and rail currents. Both plots in each figure are identically normalized, so that the current density on the center of the back surface of the rails has a magnitude of one.

Figure 4.6, which involves conductors with only sharp corners (radii = 0.1 cm), provides a good reference current distribution for discussion. The rail current distribution has only one peak ( $s \approx 2.0$ ) which corresponds to the rail inside corner. The rail current density peak which would normally

occur at  $s \approx 3$ , associated with the rail outside corner, is too small to be reflected on the scale of the plot. The first peak to be visible on the guard plate current density plot ( $s \approx 3.2$ ) is associated with the corner which has been labeled  $r_b$  in Figure 4.3. The next two peaks are associated with the guard plate top corners,  $r_t$  and  $r_o$  in Figure 4.3. At the one interior guard plate corner,  $r_i$  in Figure 4.3, a reduction in guard plate current density would be expected. This does occur, but the effect is too small to be visible on the scale of this plot. Similar comments relating current density peaks to conductor corners also apply to Figures 4.7 through 4.9.

Looking at all four figures, the most obvious feature is the degree to which rail current density can be altered by wrap-around guard plates. In all cases, rail backside and topside current densities are reduced to approximately  $1/2000^{\text{th}}$  of the front surface current. This is typical when the vector potentials of the rail and guard plates are very close to equal and the conductors are close together. Additionally, the ratio of rail peak current density ( $s \approx 2$ ) to the density on the center of the inside of the rail ( $s=0$ ) is less than 2:1, whereas railguns without guard plates, or railguns with conventional augmentation, have approximately 3:1 ratios (see Figures 2.2 and 4.4). While it would also be possible, with the conventional augmented railgun of Figure 4.1, to reduce rail back surface current to a very small magnitude by adjusting conductor vector potentials, it would not be possible to significantly affect the peak rail current density, which occurs on the rail front corners, or the rail topside current density.

Three additional observations concerning Figures 4.6 through 4.9 deserve mention. First, the guard plate geometric parameter which most influences the rail peak current density is the amount by which the guard plate extends beyond, or overhangs, the inside edge of the rail (two millimeters in Figure 4.9, zero in Figures 4.6 through 4.8). Second, imposing the one MA/inch limit to the rail peak current density causes the rails of Figure 4.9 to carry substantially more total current than the rails of Figures 4.6 through 4.8. This is because the portion of rail carrying the majority of the current ( $s < 2$ ) has a higher current density relative to the peak (at  $s \approx 2$ ) for Figure 4.9. Third, the radii of curvature for most guard plate corners have little effect on the guard plate's ability to influence rail current distribution. The one influential guard plate corner is adjacent to the inside corner of the rail (labeled  $r_b$  in Figure 4.3). Increasing the curvature of this corner is essentially equivalent to reducing guard plate overhang, since it reduces the amount of guard plate current located in the immediate vicinity of the rail inside corners, and the effect is significant. Guard plate corner radii are important, however, because they do affect the guard plate current density.

## RAIL AND GUARD PLATE CURRENT DENSITIES

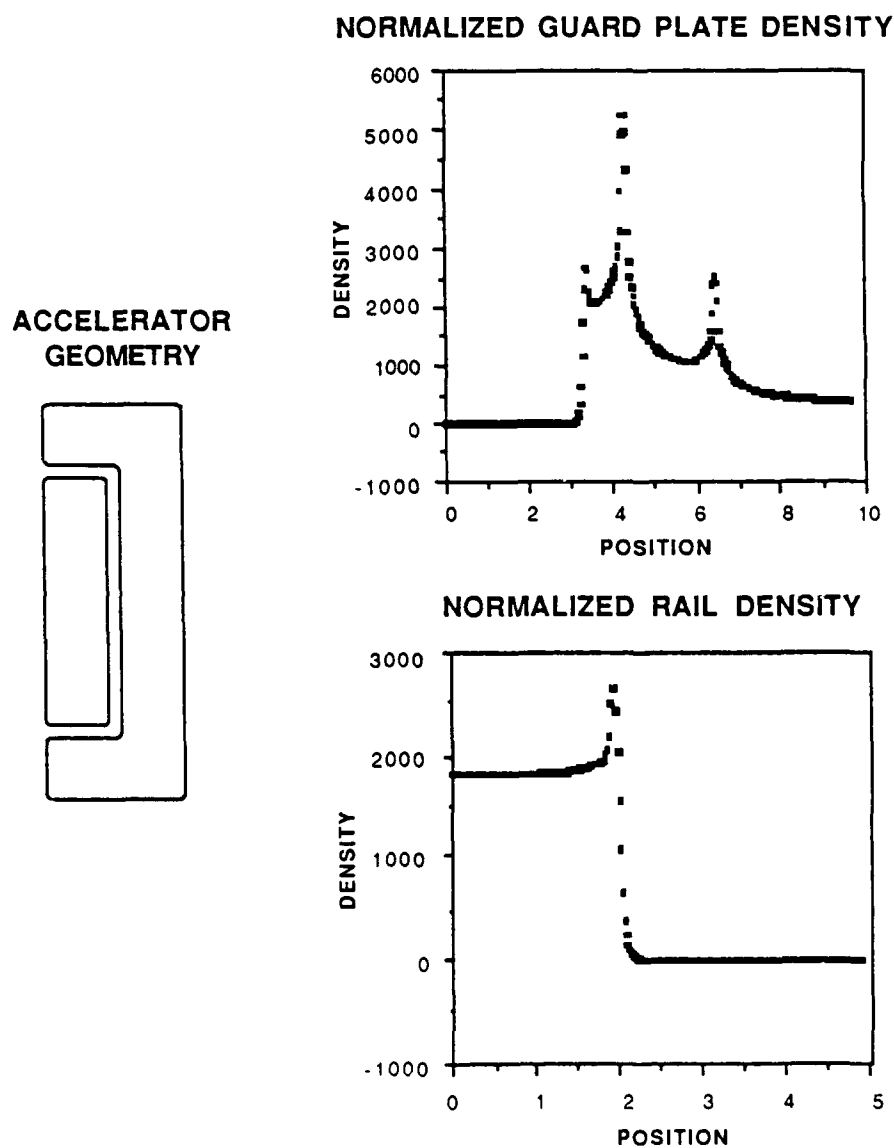


**FIGURE 4.6:** Guard plate and rail current densities for the accelerator geometry shown. The accelerator geometry shows a scale drawing of the right rail and guard plate conductors.

## RAIL AND GUARD PLATE CURRENT DENSITIES

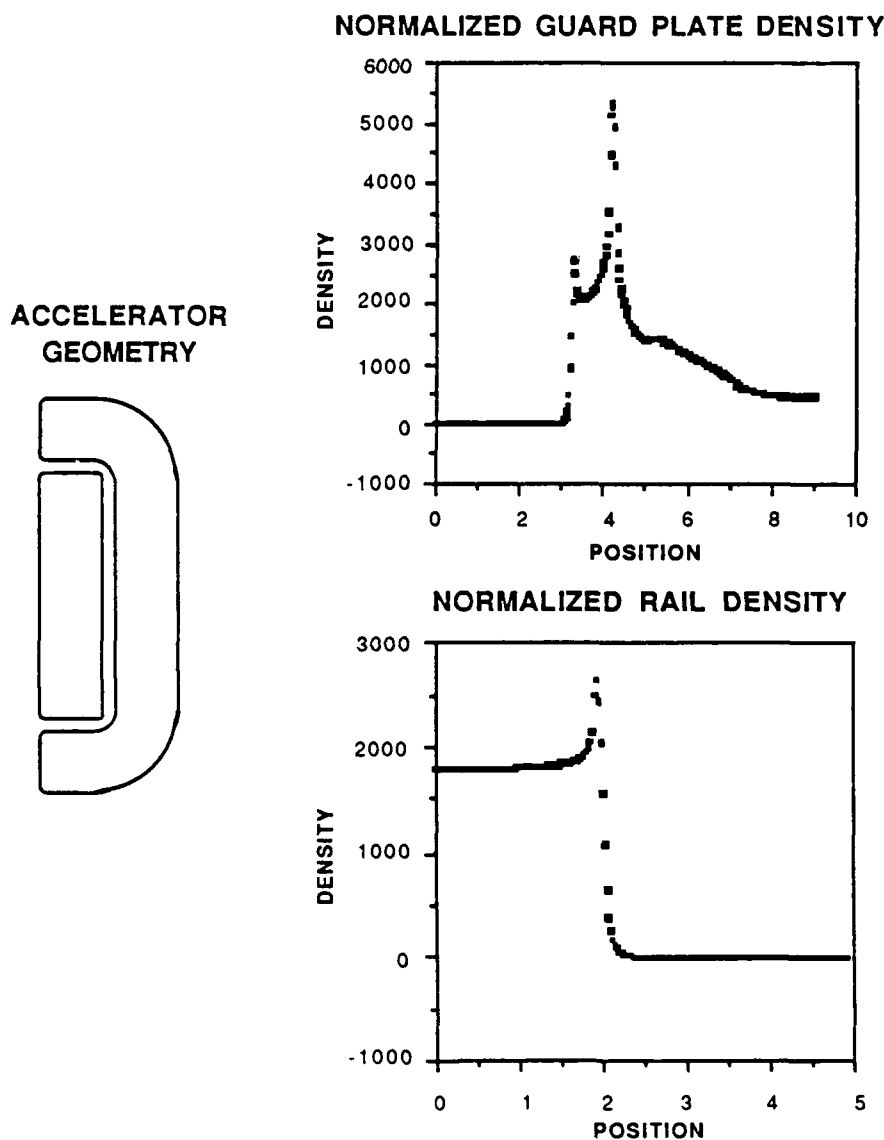
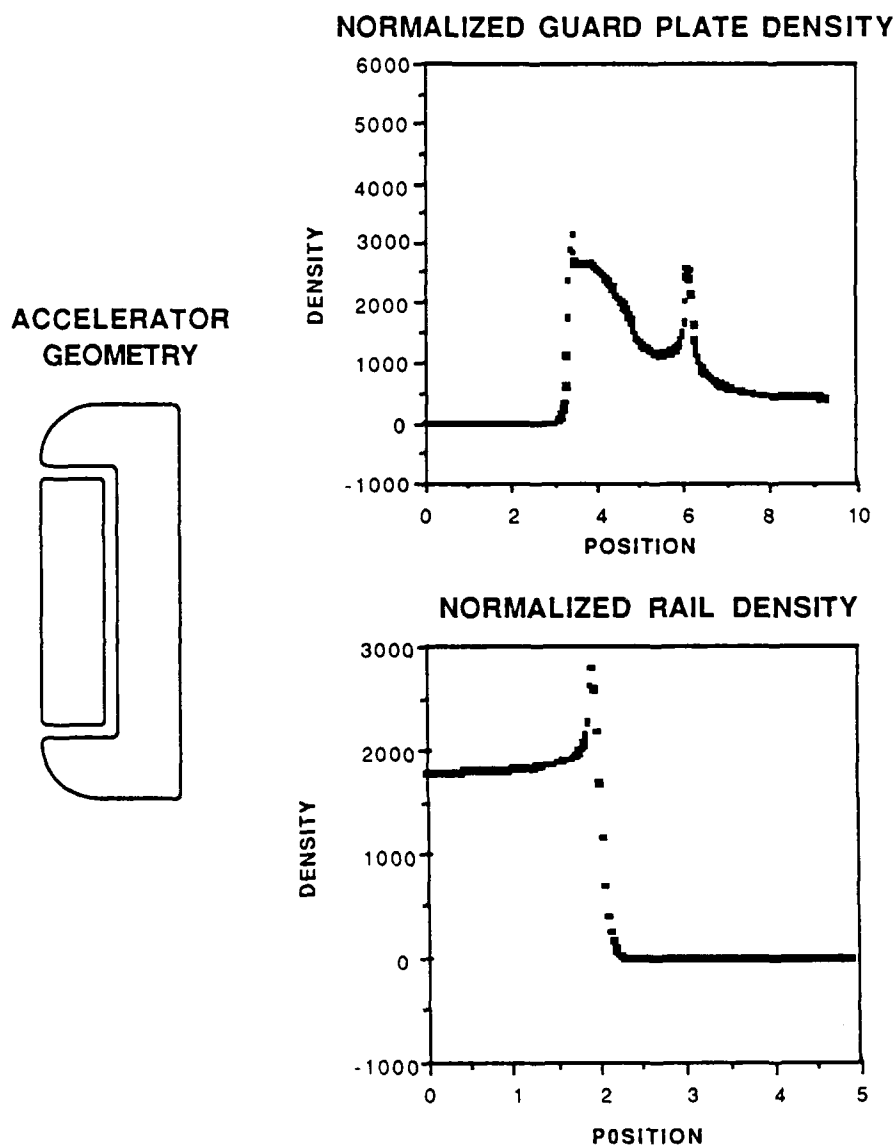


FIGURE 4.7: Guard plate and rail current densities for the accelerator geometry shown. The accelerator geometry shows a scale drawing of the right rail and guard plate conductors.



## RAIL AND GUARD PLATE CURRENT DENSITIES



**FIGURE 4.8:** Guard plate and rail current densities for the accelerator geometry shown. The accelerator geometry shows a scale drawing of the right rail and guard plate conductors.

## RAIL AND GUARD PLATE CURRENT DENSITIES

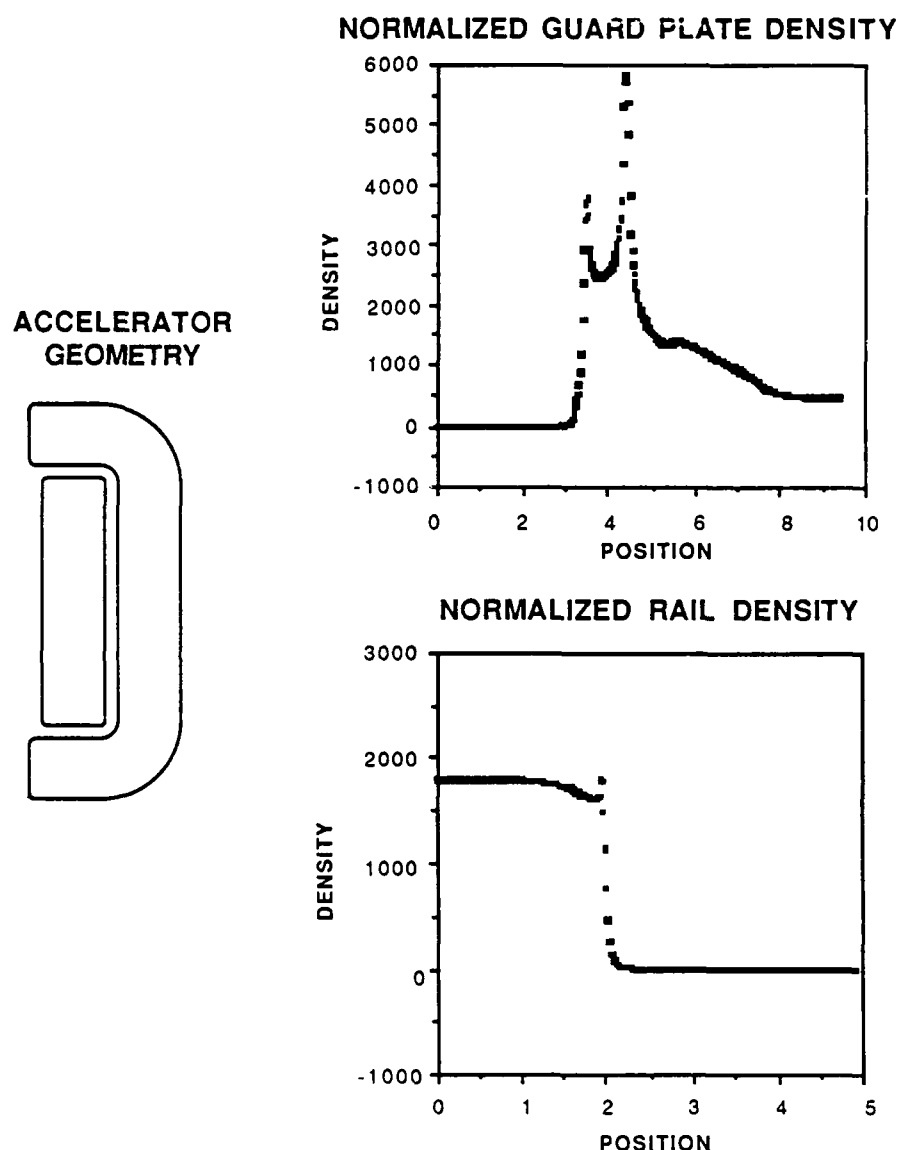


**FIGURE 4.9:** Guard plate and rail current densities for the accelerator geometry shown. The accelerator geometry shows a scale drawing of the right rail and guard plate conductors. For this figure, the guard plate overhangs the rail by 2.0 mm.

Figures 4.6 through 4.9 all involve rail and guard plates with equal vector potentials; these result in rail current distributions which, with the exception of a narrow spike at the front rail corner, closely resemble a step. However, the effects of vector potentials and guard plate geometry on projectile force has not been mentioned. Figure 4.10 presents typical results for the variation of projectile force with the ratio of rail-to-guard plate vector potentials. This particular plot is for the accelerator geometry of Figure 4.7. Both rail and guard plate peak current densities were restricted to be less than or equal to one MA/inch for these calculations, i.e., the magnitude of the greater of the rail or guard plate peak densities was set at one MA/inch, and the remaining portions of rail and guard plate distributions were scaled accordingly. Although the ratio of rail to guard plate vector potentials is 1:1 for Figures 4.6 through 4.9, Figure 4.10 highlights the fact that this does not produce maximum force. Two additional observations can be made from the plot: a low vector potential ratio can actually result in a net, negative, induced current in the rails (and a negative projectile force); and the curve is relatively flat in the vicinity of the peak force.

Figure 4.10 provides motivation to optimize guard plate design for maximum projectile force. Although most guard plate optimization efforts for this dissertation were devoted to round-bore railguns, some square-bore results were obtained and are presented here. Discussion of the actual optimization procedure is deferred until section 4.6, where it is discussed with respect to round-bore railguns.

## FORCE VS. VECTOR POTENTIAL RATIOS

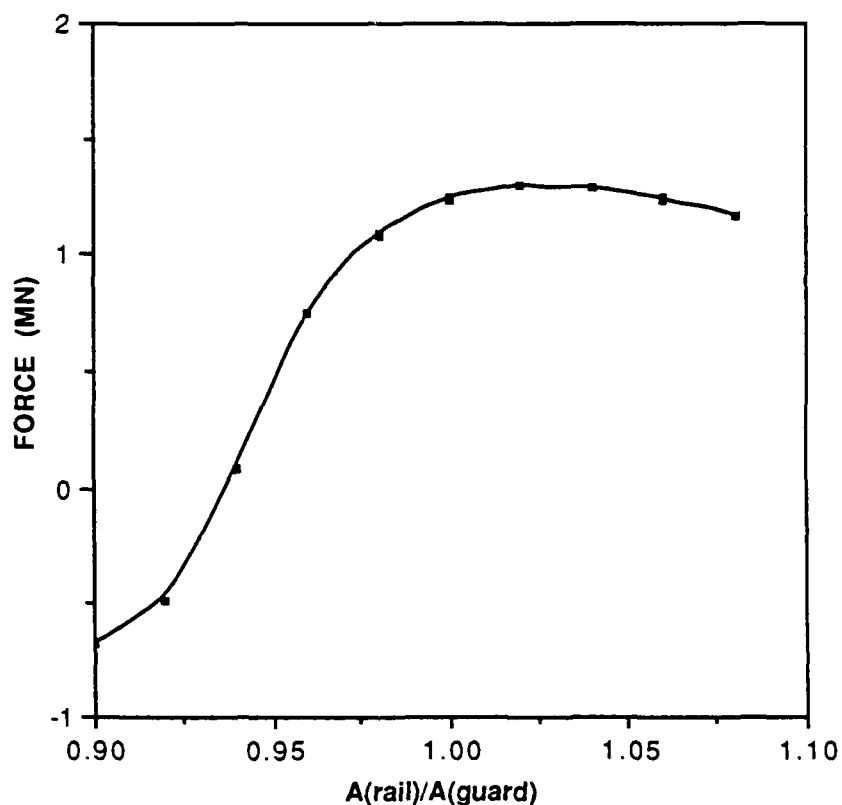


**FIGURE 4.10:** Projectile force versus the ratio of rail vector potential to guard plate vector potential. The accelerator geometry is that of Figure 4.7. Both the rail and guard plates have a peak current density less than or equal to 1.0 MA/inch.

Figures 4.11 through 4.13 present the results of optimizing the guard plate geometry for maximum projectile force. The performance results, compared to the "benchmark" square-bore railgun and the augmented, square-bore railgun discussed earlier in this section are presented below:

**TABLE 4.3**  
**FORCE OPTIMIZATION RESULTS**  
(SQUARE BORE)

Performance Parameter	Railgun with Guard Plates	Augmented Railgun	Benchmark Railgun
Rail Current	2.535 MA	0.961 MA	1.224 MA
Guard Current	2.311 MA	0.961 MA	—
Force	3.240 MN	0.543 MN	0.393 MN

The variables which were optimized to obtain the guard plate geometry were the top and bottom guard plate corner radii ( $r_t$  and  $r_b$ ) of Figure 4.3, the amount by which the top of the guard plate overhangs the rail and the ratio of rail-to-guard plate vector potentials. Other variables were fixed at the values indicated in Figure 4.11, a scale drawing of the optimized geometry. Referring to the discussion of Section 4.3, the guard plate current density was kept less than or equal to two MA/inch and the rail current density was kept less than or equal to one MA/inch for this optimization. Figures 4.12 and 4.13

show the rail and guard plate current densities. Comparing Figure 4.7 with 4.12, it is apparent that Figure 4.7 does not represent a high force configuration. This is because much of the rail surface has a very low current density, so total rail current is low.<sup>1</sup> In Section 4.8, there is further discussion on the relative merits of rail current distributions like those of Figure 4.7 and 4.12. One final, interesting result is that force optimization with guard plate current density limited to 1.5 MA/inch (instead of 2.0 MA/inch) produces a similar guard plate shape, but the projectile force is reduced to 2.370 MN.

It is now apparent that there will be complications when attempting to apply the square-bore results to the round-bore geometry. With curved rails and guard plates in a round-bore configuration, the proximity effect on the top, inside, guard plate corners ( $r_t$  in Figure 4.3) becomes more important. This is especially significant since Figures 4.6 through 4.9 show this guard plate corner to be a critical region of guard plate peak current densities. Additional complications arise from sensitivity of the rail peak current density to the guard plate overhang. In the round-bore railgun, an overhang, i.e., extension beyond the inside edge of the rails, requires the guard plates to protrude into the bore. The round-bore geometry, however, has more recognized practical applications and is of greater interest. This greater interest dictates that the round-bore

---

<sup>1</sup> Recall, all plots are normalized so that there is a density magnitude of 1.0 on the center of the back of the rail. However, it is the peak local rail current density which is fixed at one MA/inch. Therefore, a very large density on the rail front surface, relative to the density on the back (which is 1.0), does not mean that the total rail current is high.

# FORCE OPTIMIZED SQUARE-BORE RAILGUN

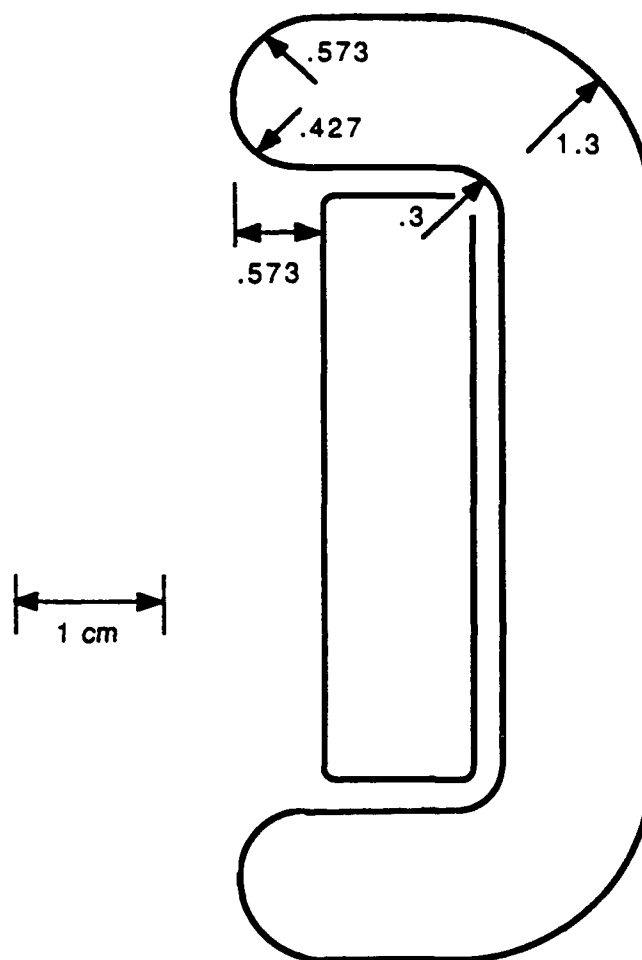


**FIGURE 4.11:** Geometry of square-bore railgun with guard plates which have been optimized for force. Drawing is to scale. Rail corners have a 0.1 cm radius, rail height and bore width are 4.0 cm, separation between guard plate and rail is 2.0 mm and all conductors are 1.0 cm thick.  $A_{\text{rail}}/A_{\text{guard}} = 1.058$ . All dimensions on the drawing are in centimeters.

## NORMALIZED RAIL CURRENT DENSITY

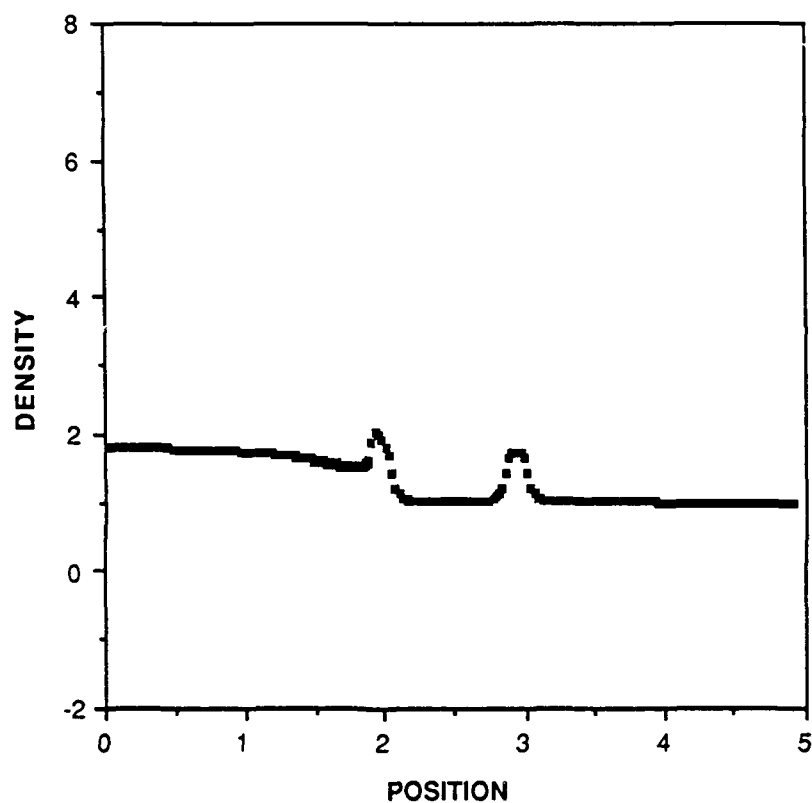


**FIGURE 4.12:** Normalized rail current density for the accelerator of Figure 4.11. The number of increments spanned by each axis were chosen to correspond to that of Figure 2.2 to assist in comparison with the "benchmark" railgun.



## NORMALIZED GUARD PLATE CURRENT DENSITY

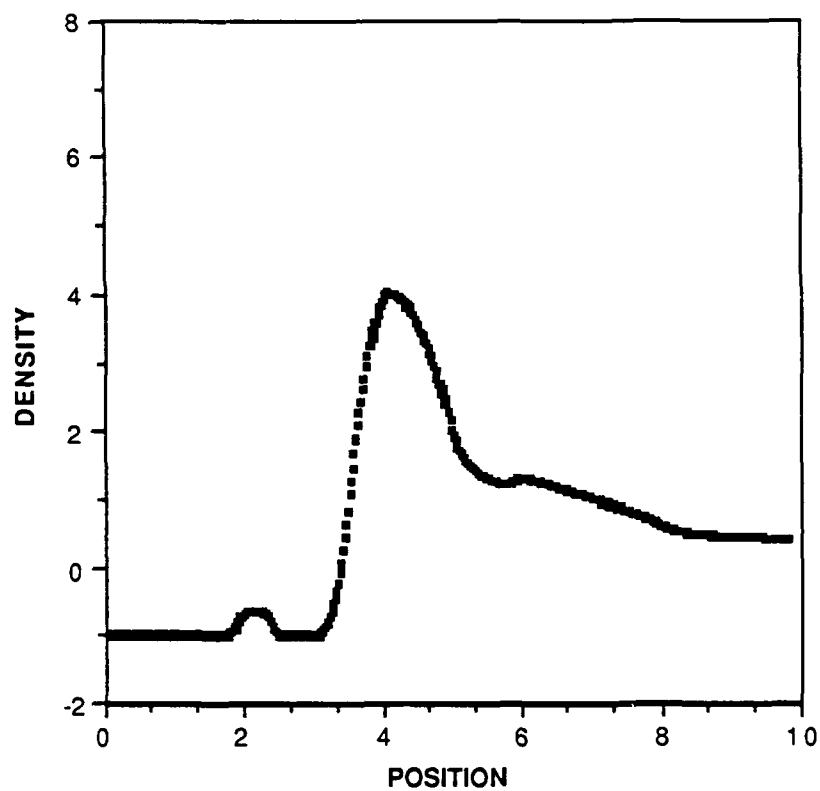


**FIGURE 4.13:** Normalized guard plate current density for the accelerator of Figure 4.11. The position axis has a different scale than that of Figure 4.12, due to the larger perimeter of the guard plates.

geometry receive most of the guard plate analysis. For this reason, optimization studies, which involve considerable computer time, to determine guard plate geometry and current distributions were primarily oriented toward round-bore railguns. These results, and discussions concerning optimization procedures, are presented in section 4.6. To provide a baseline reference, results for a typical round-bore simple, railgun and the results for a typical, round-bore, augmented railgun are first presented in the next section.

#### **4.5 Round-Bore Railguns: Baseline Performance**

This section provides current density plots and performance parameters for a two-rail, round-bore, simple railgun and a typical, round-bore, augmented railgun. To allow comparison with results presented previously in this dissertation, bore areas for all round-bore railguns considered in this chapter are 16 square centimeters, which is the same as for the "benchmark" square-bore railgun.

The two-rail railgun geometry and current distribution are provided in Figures 4.14 and 4.15. As for square-bore railguns, the origin of the position scale on current density plots corresponds to the center of the inside of the rails. Position,  $s$ , proceeds around the upper rail perimeter, ending at the center of the back surface of the rail. Additionally, current density plots are again normalized so that the density on the center of the back rail surface is 1.0. Figure 4.15 reveals that the ratio of the current density peak on the inside rail corner ( $s \approx 1.75$ ) to the density on the center of the inner rail surface ( $s=0$ ) is

## ROUND-BORE RAILGUN

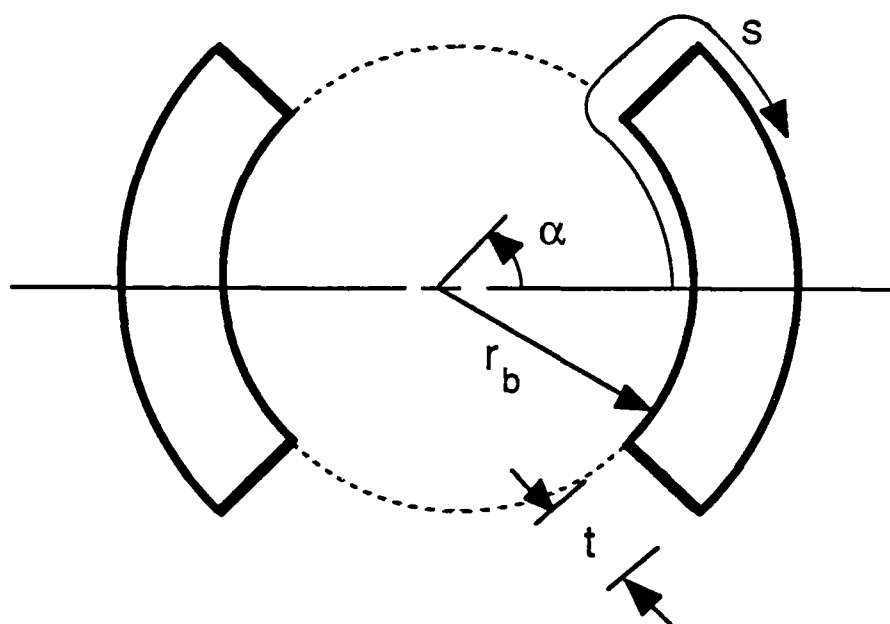


**FIGURE 4.14:** Round-bore railgun geometry. Cross-section of a two-rail, round-bore railgun is shown, defining the arc length along the perimeter ( $s$ ), the rail thickness ( $t$ ), the bore radius ( $r_b$ ), and the angle subtended by the half-rail ( $\alpha$ ). Although not shown, the rail corners are rounded with a radius of 0.1 cm. The dotted line encloses the railgun bore.

**NORMALIZED RAIL CURRENT DENSITY**  
**TWO-RAIL, ROUND-BORE RAILGUN**

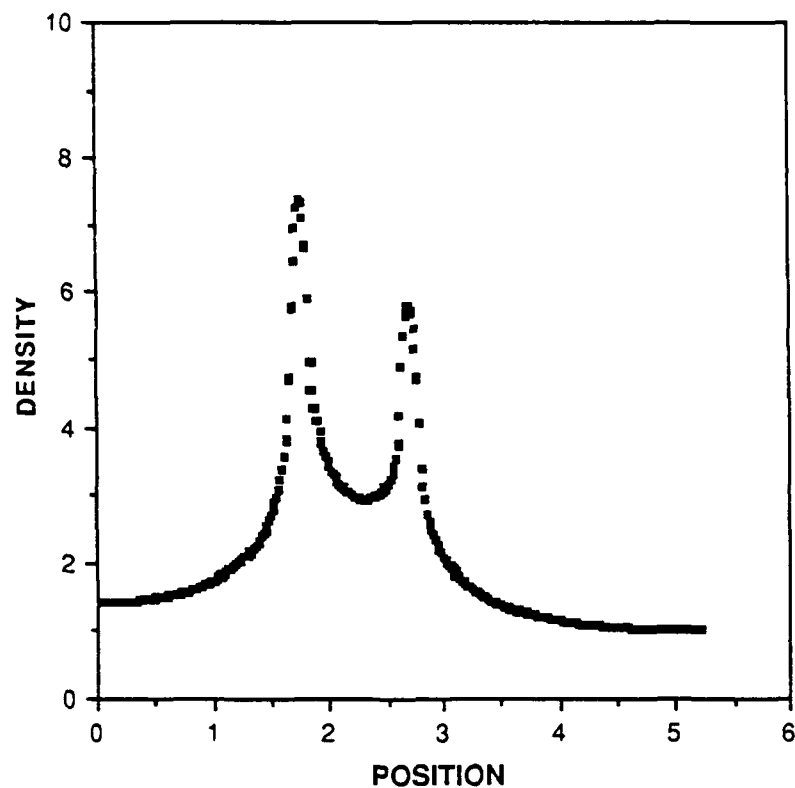


**FIGURE 4.15:** Normalized current density for the two-rail, round-bore railgun of Figure 4.14. For this plot  $r_b = 2.257$  cm (bore area = 16 sq. cm),  $\alpha = 45^\circ$ ,  $t = 1.0$  cm, and all corner radii = 0.1 cm. This railgun produces a projectile force of 0.346 MN with a current of 1.184 MA..

approximately 5:1. As shown in Figure 2.2, the ratio of the inside corner peak density to the density on the center of the inner rail surface for the square-bore railgun is only 3:1. This would indicate that localized rail heating, and rail damage, is more severe in the round-bore railgun. The force developed by this round-bore railgun is 0.346 MN, with a current of 1.184 MA and an inductance gradient of 0.494  $\mu\text{H/m}$ .

Since Chapters 3 and 4 of this dissertation are intended to be independent, it is worth re-emphasizing that the current distribution in Figure 4.15 is for a region of rail some distance behind the armature. Considerations such as those discussed by Marshall (1984) and mentioned in Section 3.1, lead to the conclusion that the current peaks on the inner rail corners at the temporary location of the moving armature are probably worse than depicted in Figure 4.15. This is because current on the top and back rail surfaces ( $s > 1.75$  in Figure 4.15), which accounts for 60% of the rail current, must flow over rail surfaces (around the rail perimeter in Figure 4.14) to reach the armature. These considerations also lead to the conclusion that, in order to provide maximum total current with minimum local density peaks near the armature, the ideal current distribution would be one with high uniform levels of current on inside rail surfaces ( $s < 1.75$  in Figure 4.15) and zero current on the top and back rail surfaces ( $s > 1.75$ ). The rail current distributions of Figures 4.6 through 4.9, for square-bore railguns, are actually close to such an ideal current distribution.

The geometry and rail current distribution for a typical two-rail, round-bore augmented railgun are presented in Figures 4.16 and 4.17. The railgun of Figure 4.16 is identical to that of

Figure 4.14, with the exception that one centimeter thick, augmenting conductors have been added. If railgun peak current densities are limited to one MA/inch, the augmented railgun develops a projectile force of 0.316 MN, which is less than that of the railgun without augmentation. This calculation assumes that the rail and augmenting conductors are in series, i.e., carry the same current. The force reduction stems from an increase in the relative magnitude of the current peak on the inside rail corner ( $s \approx 1.75$ ) caused by the augmenting current. The ratio of current density on the inside rail corner to that on the center of the front of the rail for the augmented railgun is approximately 6:1, compared to 5:1 for the nonaugmented railgun (Figure 4.15). The effect of defining the magnitude of this heightened peak as one MA/inch is to reduce total rail current. The peak augmenting current density (plot not provided) is less than the rail peak density; therefore, it is not necessary to impose limits on the augmenting distribution of 1.0, 1.5, 2.0, or 3.0 MA/inch.

The force reduction for the round-bore, augmented railgun is contrasted with the increase found for square-bore, augmented railguns. For the square-bore, augmented railgun, extending the augmenting conductors above the rails (see Figure 4.1) has the effect of offsetting the tendency for an increased current density peak on the inner rail corner. Such an extension is not possible for the round-bore geometry without significantly aggravating the proximity effect between opposing augmenting conductors.

The inductance gradient of the augmented railgun in Figure 4.16 is  $1.252 \mu\text{H/m}$  (compared with  $0.494 \mu\text{H/m}$  for the nonaugmented gun). Based on this inductance gradient, if the

augmented railgun is driven with the same total current as the railgun of Figure 4.14, the force would increase to 0.878 MN. Although larger force for the same total current is usually cited as the major benefit of augmented railguns, this requires accepting higher rail peak current densities than previously allowed in this dissertation. A summary of results for the square- and round-bore railguns, with and without augmentation, is provided below for convenience:

**TABLE 4.4**  
**SQUARE-BORE AND ROUND-BORE**  
**RAILGUN PERFORMANCE SUMMARY**

Railgun type	Force (MN)	Current (MA)	Inductance Gradient ( $\mu\text{H}/\text{m}$ )
Square-Bore	0.393	1.224	0.525
Augmented, Square	0.543	0.961	1.175
Round-Bore	0.346	1.184	0.494
Augmented, Round	0.316	0.710	1.252

## ROUND-BORE, AUGMENTED RAILGUN

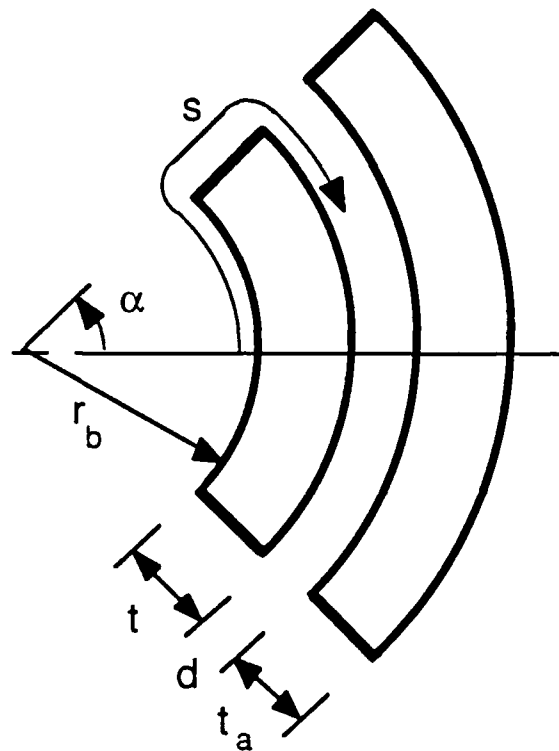


**FIGURE 4.16:** Round-bore, augmented railgun geometry. Only one rail, with augmenting conductor is shown. The usual rail variables are shown, as is the separation between augmenting conductor and rail ( $d$ ), and thickness of the augmenting conductor ( $t_a$ ).



**NORMALIZED RAIL CURRENT DENSITY**  
**TWO-RAIL, ROUND-BORE, AUGMENTED RAILGUN**

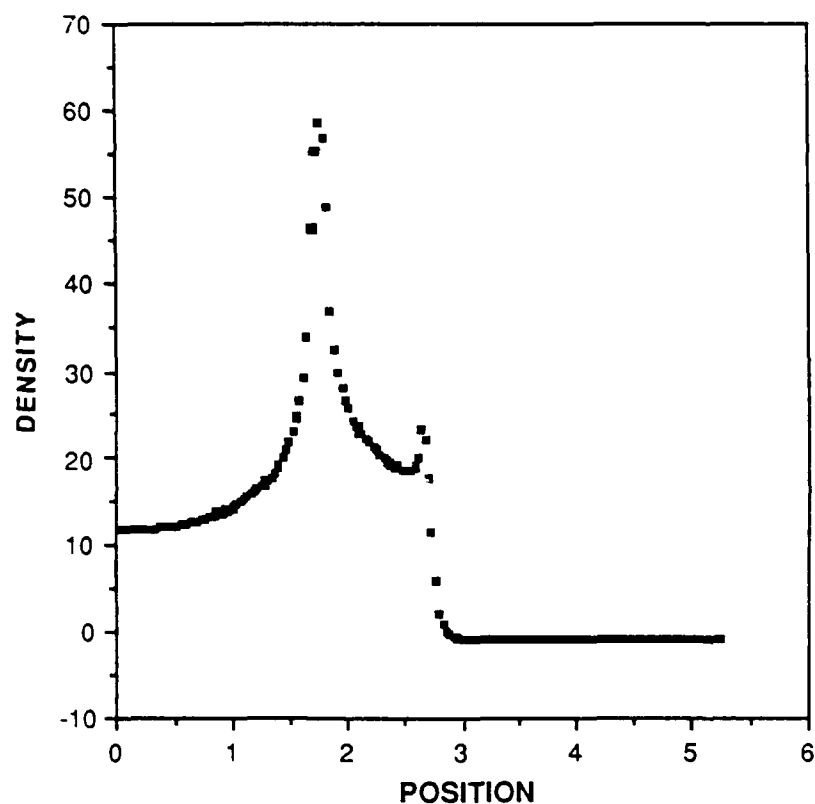


**FIGURE 4.17:** Normalized rail current density for the two-rail, round-bore, augmented railgun of Figure 4.16. For this plot  $r_b = 2.257$  cm (bore area = 16 sq. cm),  $\alpha = 45^\circ$ ,  $t = 1.0$  cm,  $t_a = 1.0$  cm,  $d = 2.0$  mm, and all corner radii = 0.1 cm. This railgun produces a force of 0.316 MN with a current of 0.710 MA.

#### 4.6 Force Optimized Round-Bore Guard Plates

Now that round-bore, two-rail, augmented and nonaugmented railgun results have been presented for reference, wrap-around guard plates will be addressed. Figure 4.18 depicts the round-bore railgun of Figure 4.14, with the addition of guard plates. The figure also defines the guard plate variables which will be used throughout this section and the next. Rail variables are as depicted in Figure 4.14 and have not been repeated. Rail and guard plate currents are in the same direction as their respective vector potentials, which are shown as into the paper.

This section and Section 4.7 are devoted to optimization of round-bore guard plates. Optimization procedures, based on a downhill simplex, functional minimization routine (see Section 3.5 of this dissertation, as well as Press et al. 1986; Section 10.4) were utilized to determine good guard plate designs. Two cases were considered: 1) design was optimized to produce maximum projectile force with current density limits of 1.0 MA/inch on the rails and 1.0, 1.5, 2.0, or 3.0 MA/inch on the guard plates. 2) design was optimized to produce as close to an ideal current distribution as possible with the same imposed current density limits. This section discusses optimization procedures and the results of force optimizations. Section 4.7 presents the results of current distribution optimization. As mentioned in Section 4.3, by considering four different guard plate current densities, an appropriate range of results is provided. For both force and current optimizations, the same set of variables was optimized.

The variable set used for optimization was determined after completing several current density calculations, intended to investigate the relative effect of geometric variables on rail and guard plate current distributions. Results obtained were consistent with those displayed in Figures 4.6 through 4.9 for the square-bore railgun and are not repeated here. The variables selected (shown in Figure 4.18) were the radius of curvature on the top, inside, guard plate corner,  $r_t$ ; the radius of the top portion of guard plate,  $r_p$ ; the half-angle subtended by rail,  $\alpha$ ; and the relative magnitude of magnetic vector potentials for the rails and guard plates behind the projectile (which determines the total current in each.) All other geometric variables were fixed at appropriate values as follows:

- 1) remaining guard plate corner radii were set large enough to insure that local current density peaks were not severe, while rail corner radii were fixed at 0.1 cm
- 2) separation distances between the guard plate and rail were set at 2.0 mm to allow for insulation
- 3) rail and guard plate thicknesses were fixed at one centimeter; this is consistent with conductor thicknesses used throughout this dissertation
- 4) bore radius was set at 2.257 cm, so the bore area equals 16 square centimeters
- 5) the minimum thickness of the portion of the guard plate which is above and below the rail ( $t_t$  in Figure 4.18) was fixed at 0.75 cm; this is discussed in more detail in the following paragraph.

# ROUND-BORE GUARD PLATE DESIGN

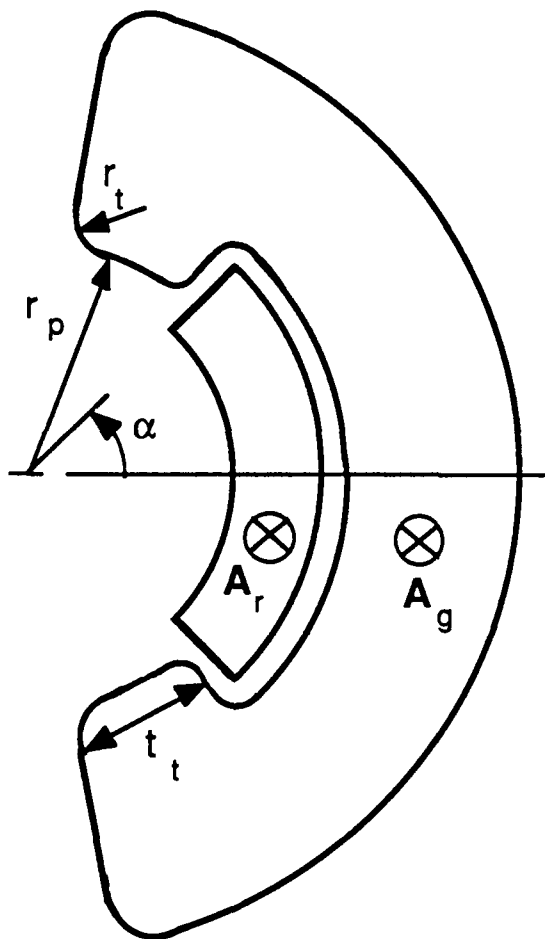


**FIGURE 4.18:** Round-bore railgun with addition of wrap-around guard plates. Only the right rail and guard plate are shown. The drawing defines the radius of the top, inside, rail corner,  $r_t$ ; the radius of the top portion of the guard plate,  $r_p$ ; the thickness of the portion of the guard plate above and below the rail,  $t_t$ ; and the rail and guard plate vector potentials,  $A_r$  and  $A_g$ . Vector potentials are shown as into the page. The rail variables are the same as defined in Figure 4.14.

Establishing guard plate thickness,  $t_t$ , as 0.75 cm requires explanation. Calculations show that reducing this thickness improves the guard plate's ability to influence the rail current density peaks which exist on the inside rail corners, and also reduces the proximity effect between opposing guard plates. However, insufficient thickness in the portions of guard plate above and below the rails will cause thermal problems from resistive heating. Effects of resistive heating on guard plate temperature depend on guard plate currents as a function of time. Accordingly, detailed guard plate thermal analysis can only be accomplished after the required performance goals and power supplies for a particular railgun task are known. For this dissertation, which is intended to be of a more general nature and not specific to any one particular railgun, it was judged imprudent to reduce the guard plate thickness,  $t_t$ , below 0.75 cm.

Before presenting optimization results, it is interesting to note that these optimizations require substantial amounts of computer time. Each optimization run can require 300 to 600 current and force calculations, and each calculation requires three large, matrix-inversions, as discussed in Section 4.2. Even with matrix sizes reduced as much as possible (while still providing enough conductor subsections for consistent results), 5,000 to 10,000 seconds on the Cray X-MP/24 are often required for one optimization run. Since numerous restarts are necessary to insure that optimization results represent global minima and not local minima, it is apparent that considerable computer time is required.

Results of guard plate optimizations will now be presented. As mentioned previously, eight different cases were

considered. Force was maximized with guard plate peak densities of 1.0, 1.5, 2.0, and 3.0 MA/inch, and current distribution was optimized for the same four guard plate current densities. For all cases, rail current density was limited to 1.0 MA/inch. To facilitate understanding of all results, force and current optimizations employing the guard plate density limit of 2.0 MA/inch will be discussed in detail. This will include presentation of accelerator cross-sectional scale drawings, rail current density plots and guard plate current density plots. Results for the remaining 6 optimizations will be presented in tabular form only.

This section presents results of force optimizations. Figures 4.19 through Figure 4.21 display results obtained for the case in which the guard plate peak current density is 2.0 MA/inch (rail current peak density is 1.0 MA/inch). Figure 4.19 is a scale drawing of the force-optimized, railgun cross-section. Figures 4.20 and 4.21 present the associated rail and guard plate current distributions. Both current density plots are normalized by the same factor, so that the current density on the center of the back surface of rail is 1.0 . The force and current magnitudes presented in the caption to Figure 4.20 assume availability of independent power sources for rails and guard plates. If guard plates and rails are connected in series, i.e., driven by one power source, projectile force is 1.94 MN, rail and guard plate current is 2.10 MA, and the effective inductance gradient is 0.88  $\mu\text{H/m}$ .

# FORCE-OPTIMIZED, ROUND-BORE RAILGUN WITH GUARD PLATES

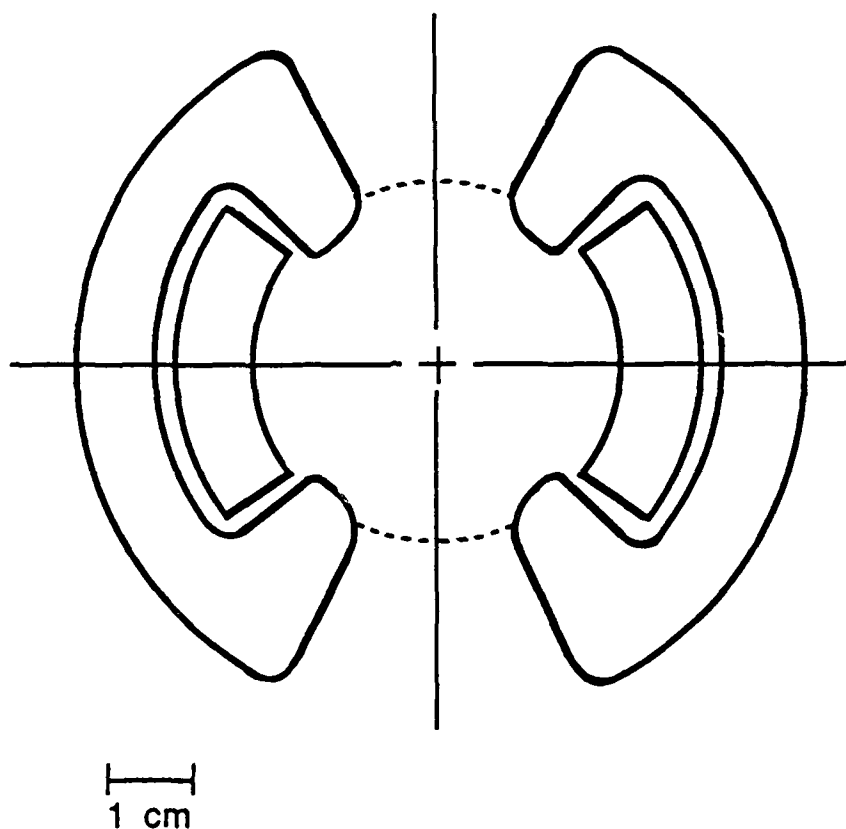


**FIGURE 4.19:** Scale drawing of a round-bore railgun with guard plates optimized for maximum force. Referring to Figure 4.18,  $r_t = 0.613$  cm,  $r_p = 1.968$  cm,  $\alpha = 37.8^\circ$ , and  $A_r/A_g = 1.08714$ . The guard plates overhang the rails and protrude into the bore 0.289 cm, i.e., bore radius minus  $r_p$  equals 0.289 cm.

**NORMALIZED RAIL CURRENT DENSITY**  
**TWO-RAIL RAILGUN WITH GUARD PLATES**

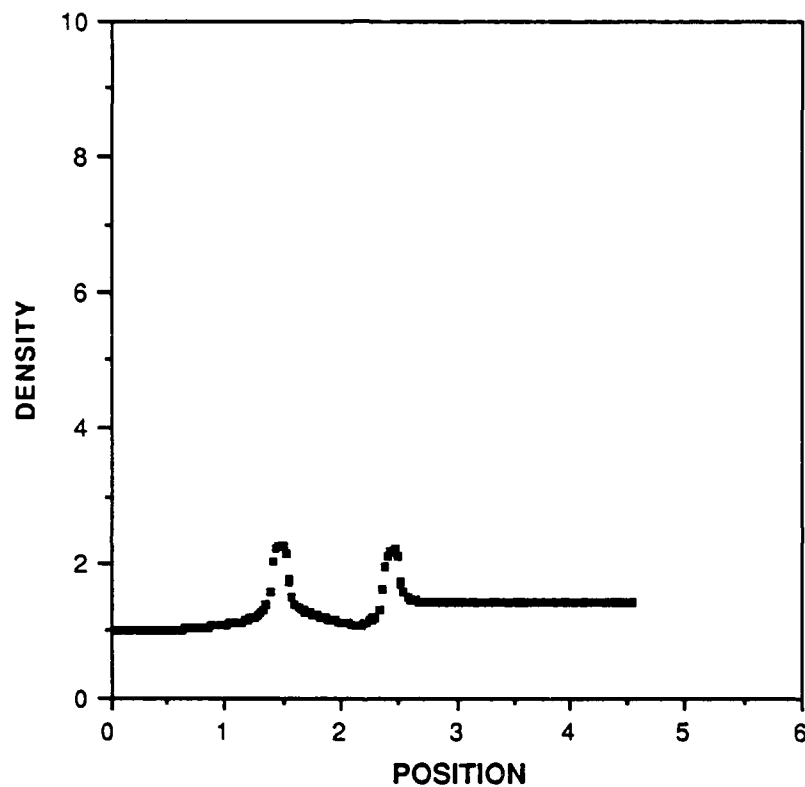


**FIGURE 4.20:** Normalized rail current density for the railgun with guard plates of Figure 4.19. Force developed with this gun is 2.49MN, with a rail current of 2.14MA and a guard plate current of 2.95MA. This calculation invokes limits of  $\leq 1\text{MA}$  and  $\leq 2\text{MA}$  for maximum, allowable, current density peaks in rails and guard plates, respectively. Scales for this plot are the same as in Figure 4.15 to facilitate comparison.



**NORMALIZED GUARD PLATE CURRENT DENSITY**  
TWO-RAIL RAILGUN WITH GUARD PLATES

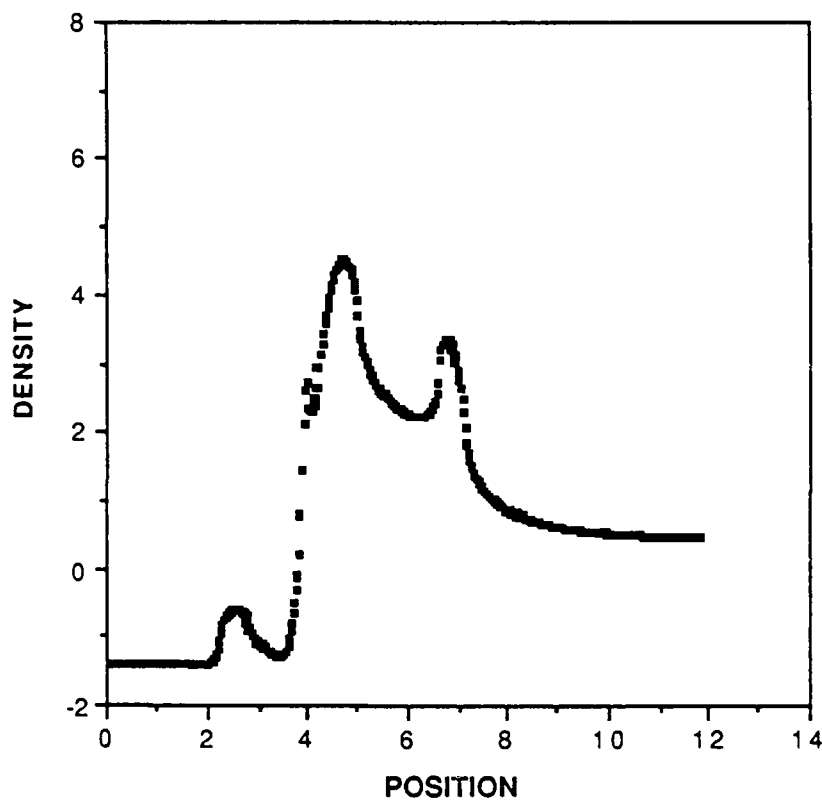


**FIGURE 4.21:** Normalized guard plate current density for the railgun of Figure 4.19. This plot is the companion plot of Figure 4.20.

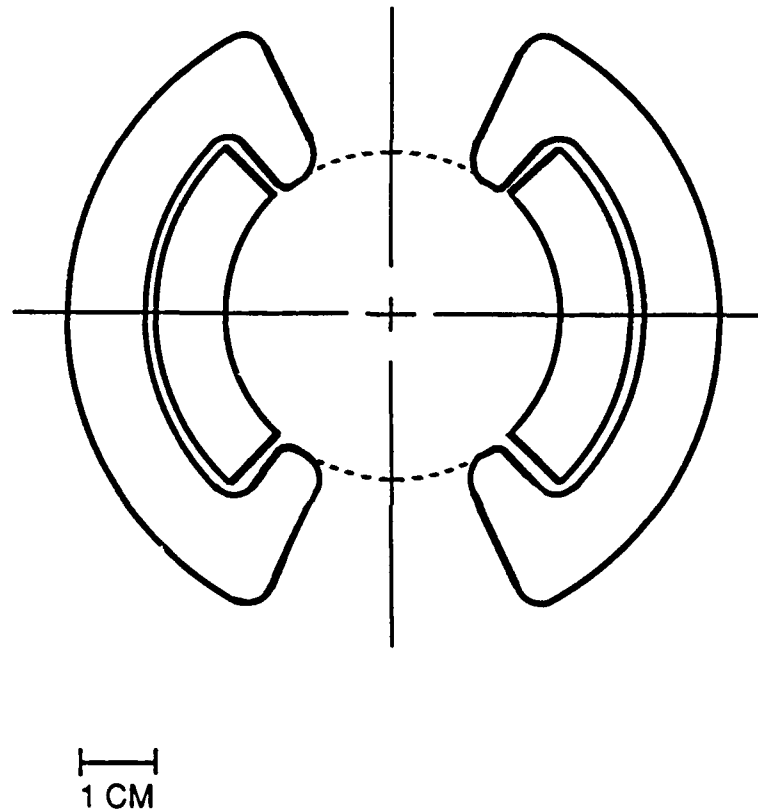
The fact that guard plates overhang the rails and intrude slightly into the bore in Figure 4.19 causes significant complications in railgun design and manufacture. Although similar to rifling which has been a necessary part of chemical gun design for many years, the possibility of eliminating the need for this overhang is of interest. Therefore, several optimizations were done in which guard plates were not allowed to overhang the rails. The results obtained for the case in which the guard plate peak current density is 2.0 MA/inch, are presented next.

Figure 4.22 depicts the force-optimized guard plate, with no overhang. The guard plate design of Figure 4.22 is seen to have a very similar, general shape to that of Figure 4.19, the main difference being that the guard plate does not protrude beyond the inside rail edge. This is typical of most results in this chapter: seemingly minor, geometric changes, coupled with variations in conductor vector potentials, significantly affect railgun performance. Figures 4.23 and 4.24 present the associated rail and guard plate current distribution. Again, force magnitudes assume the availability of independent rail and guard plate power sources.

Force optimizations invoking the other guard plate current densities (1.0, 1.5, and 3.0 MA/inch) result in current distributions and guard plate shapes similar to those displayed in Figures 4.22 through 4.24. Consequently, plots and scale drawings are not presented for these cases, although results are tabulated in the following chart. The variable names at the top of each column refer to the variables depicted in Figure 4.18. Only two optimizations were done with guard plates being

# FORCE-OPTIMIZED, ROUND-BORE RAILGUN WITH GUARD PLATES

(Without Overhang)



**FIGURE 4.22:** Scale drawing of a round-bore railgun with guard plates optimized for maximum force. Referring to Figure 4.18,  $r_t = 0.394$  cm,  $\alpha = 45.23^\circ$ , and  $A_r/A_g = 1.06002$ . For this optimization,  $r_p$  was fixed at the bore radius of 2.257 cm.

**NORMALIZED RAIL CURRENT DENSITY**  
**TWO-RAIL RAILGUN WITH GUARD PLATES**  
(Without Overhang)

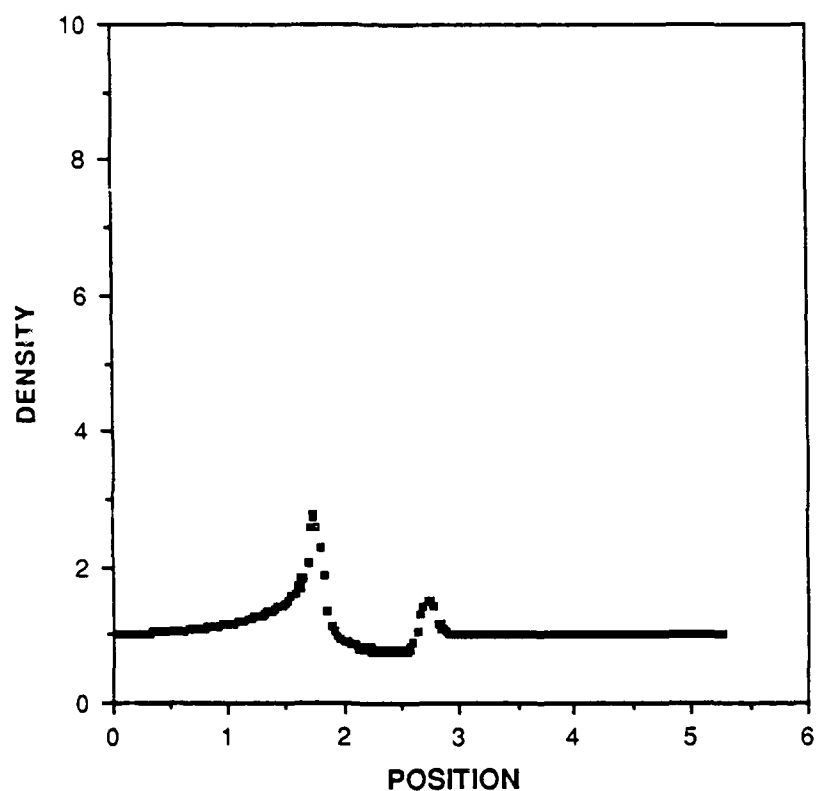


**FIGURE 4.23:** Normalized rail current density for the railgun with guard plate of Figure 4.22. Force developed with this gun is 1.59MN, with a rail current of 1.65MA and a guard plate current of 2.85MA. This calculation invokes limits of  $\leq 1\text{MA}$  and  $\leq 2\text{MA}$  for maximum, allowable, current density peaks in rails and guard plates, respectively. Scales for this plot are the same as in Figure 4.15 to allow comparison .

**NORMALIZED GUARD PLATE CURRENT DENSITY**  
TWO-RAIL RAILGUN WITH GUARD PLATES

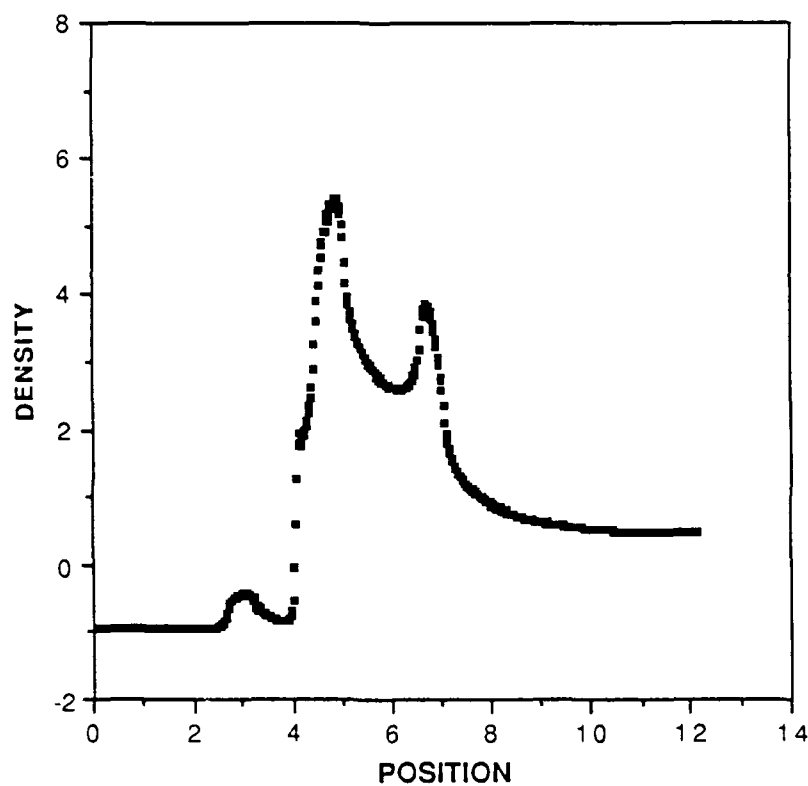


**FIGURE 4.24:** Normalized guard plate current density for the railgun of Figure 4.22. This plot is the companion plot of Figure 4.23.

allowed to overhang and extend beyond the rails into the bore. This was due to the large amounts of computer time required to perform each optimization and the fact that extended overhangs cause railgun design and production difficulties. The two cases selected for optimization with guard plate overhang were chosen to bracket the most interesting operating conditions. They are included to highlight the benefits accrued from a small degree of guard plate projection into the bore.

**TABLE 4.5**  
**FORCE OPTIMIZATION RESULTS**  
(ROUND BORE)

Max Guard Density (MA/in)	$A_r/A_g$	$r_t$ (cm)	Overhang ( $r_r - r_p$ ) (cm)	$\alpha_r$ (deg)	Force (MN)	Rail Current (MA)	Guard Current (MA)
1.0	1.10814	0.650	0.000	31.59	1.186	1.621	1.115
1.5	1.06478	0.598	0.000	40.49	1.506	1.593	2.333
2.0	1.06002	0.394	0.000	45.23	1.585	1.647	2.850
3.0	1.05920	0.199	0.000	50.79	1.640	1.733	3.579
1.5	1.09186	0.646	0.228	30.96	1.925	1.814	2.120
2.0	1.08714	0.613	0.289	37.80	2.489	2.137	2.946

When interpreting the above results, it should be remembered that the thickness of the portion of guard plate

above and below the rail,  $t_t$  in Figure 4.18, was fixed at 0.75 cm and that the radius of the guard plate corner which is closest to the inside rail corner was set to be 0.1 cm. Accordingly, the radius of the top, inside, guard plate corner ( $r_t$  in Figure 4.18), can be no larger than 0.65 cm. For the optimization with a maximum guard plate density of 1.0 MA/inch (see preceding table),  $r_t$  has its maximum value. Even with this maximum radius, it is not possible to have a peak guard plate density of only one MA/inch without a large rail vector potential (relative to that of the guard plate) which increases the rail current (with respect to the guard plate current). This explains why some values displayed in the first row of the table do not follow trends established in other rows.

#### **4.7 Current-Optimized, Round-Bore Guard Plates**

Rail current distributions for railguns with force-optimized guard plates (Figures 4.20 and 4.23) do not resemble the rail current distributions of Figures 4.6 through 4.9. Although Figures 4.6 through 4.9 depict rail densities that are close to what had been previously described as "ideal" (high current densities on the rail inner surface and zero distribution on the other rail surfaces), they do not represent high rail total currents since much of the rail surface is not used to carry current. Consequently, ideal current configurations are not maximum force configurations. Although all previous sections in this dissertation have used force to measure railgun goodness, guard plate design can also be optimized to shape rail

current distribution to be as close to ideal as possible. This section discusses current optimization procedures and results.

The set of variables used in current optimizations were the same as for force optimizations. The optimization procedure minimized the "variance" of calculated, rail current distribution from a specified ideal. Variance was defined in terms of the average of the absolute value of the difference between ideal and actual local current densities. This variance is calculated by first specifying the ideal current density,  $J(\text{ideal})_m$ , for each segment of rail surface (rail segments are the  $\Delta s_m$  in equations 2.13 and 2.14). Next, the actual current distribution,  $J(\text{actual})_m$ , for a particular set of geometric variables and a specified ratio of rail to guard plate vector potentials is calculated, using the methods discussed previously. Then, variance is calculated using the following expression:

$$\text{Variance} = \frac{1}{N} \sum_{m=1}^N | J(\text{ideal})_m - J(\text{actual})_m | \quad (4.12)$$

where  $N$  is the total number of rail segments.

The specification of the ideal current distribution requires some discussion. As mentioned previously, an ideal rail current distribution is one with high, uniform, current density on the portion of rail in electrical contact with the armature and a current density elsewhere which is approximately zero. This type of current distribution can cause computational difficulties because the technique to calculate current



distribution involves solving a large matrix equation. Numerical difficulties during solution can arise when the matrices have both large and small numbers; large, cumulative errors can result. A very wide range of density magnitudes in the calculated current distribution is a good indication that these large, cumulative errors may have accrued. The problem can be alleviated by using double precision variables or by using iterative matrix solution schemes, but either option increases computation time significantly. Through trial and error, it was found that consistent matrix solutions can be accomplished, using the efficient IMSL routines, if the ratio of the resulting current density on the center of the rail front surface to the density on the center of the rail back surface is less than 1200:1. Therefore, allowing a reasonable safety margin, the ideal, rail current density was defined to be one which had a normalized magnitude of 400 on portions of rail in contact with the armature and a magnitude of one elsewhere.<sup>1</sup>

Once an appropriate, ideal current distribution was specified, attempts to optimize rail current distributions quickly established the result that railguns with very small angles subtended by the rail ( $\alpha$  in Figure 4.18) have the smallest variances. Since a very small angle implies very small rail surface and very small rail current, this would be a very low force railgun. However, it was found that the rail angle,  $\alpha$ , could often be fixed at a larger value, such as 20° or 40°, and other guard plate parameters, such as the guard plate top, inside,

---

<sup>1</sup>The 1200:1 ratio is not an absolute limit. With care, ratios exceeding 6000:1 can also provide useful results. In this situation, for use during optimizations, a safe criteria, insuring very consistent results, was needed.

corner radius ( $r_t$  in Figure 4.18), could be adjusted to compensate. This still produced a good current distribution, with only a slightly increased variance. Figures 4.25 and 4.26 illustrate this effect. These figures present rail current distributions that resulted from guard plates which were current optimized with rail half-angles of  $20^\circ$  and  $40^\circ$ . Although the rail current distribution in Figure 4.25 matches the specified ideal closer than that of Figure 4.26, both are seen to be good current distributions. Both have a high, relative current density on the inside of the rail. Both distributions also have a small ratio of peak current density (on the inside rail corner) to that on the center of the inner rail surface. With the exception of the current peaks, both current distributions are seen to closely resemble a "step" distribution. The accelerator of Figure 4.26, however, carries more total current and produces much more projectile force than that of Figure 4.25.

Due to the aforementioned effects of the rail angle,  $\alpha$ , current optimizations were done in sequences. For each of the four, specified, guard plate peak current densities (1.0, 1.5, 2.0, and 3.0 MA/inch), rail current optimizations were performed with successively larger rail angles,  $\alpha$ . The intent was to find accelerator geometries with good current and force characteristics. As  $\alpha$  was increased, each current-optimized design produced more force until a limit was eventually reached, so that further increases in  $\alpha$  caused decreases in force. It should be noted that in the vicinity of peak force, changes in  $\alpha$  cause small changes in force, i.e., the  $\alpha$  vs. force curve is flat in this region. This allowed relatively large step increases in  $\alpha$ . Due to the large amount of computer time required for each step

**NORMALIZED RAIL CURRENT DENSITY**  
**TWO-RAIL RAILGUN WITH GUARD PLATES**

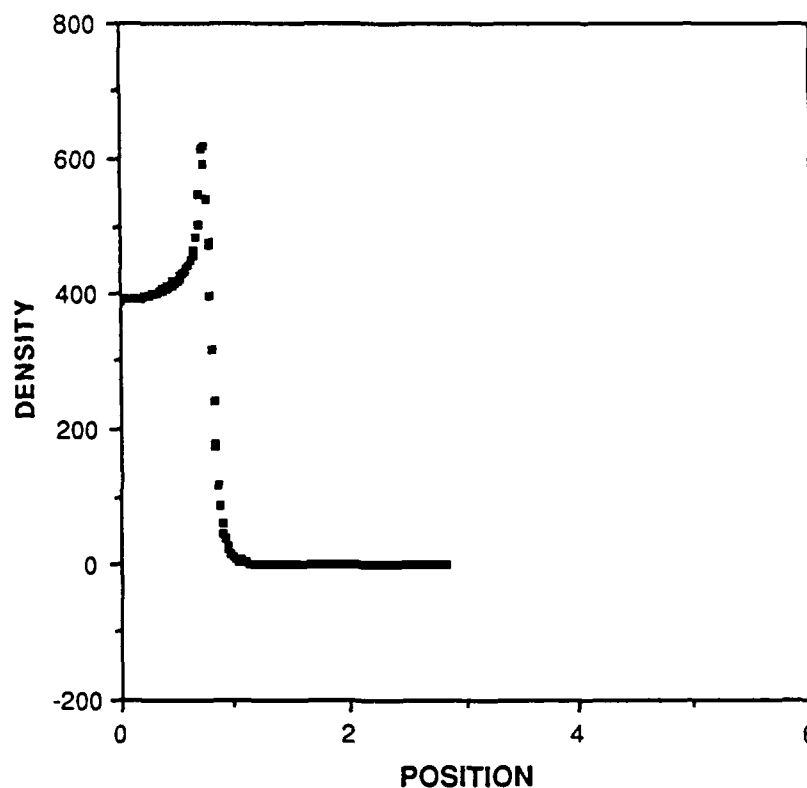


**FIGURE 4.25:** Rail current density for a current-optimized railgun. Referring to Figure 4.18,  $r_t = 0.444$  cm and  $A_r/A_g = 1.0002$ ;  $r_p$  was fixed at the bore radius of 2.257 cm and the rail angle,  $\alpha$ , was fixed at  $20^\circ$ . This railgun produces a projectile force of 0.782 MN. It has a rail current of 0.459 MA and a guard plate current of 3.704 MA.

# NORMALIZED RAIL CURRENT DENSITY TWO-RAIL RAILGUN WITH GUARD PLATES

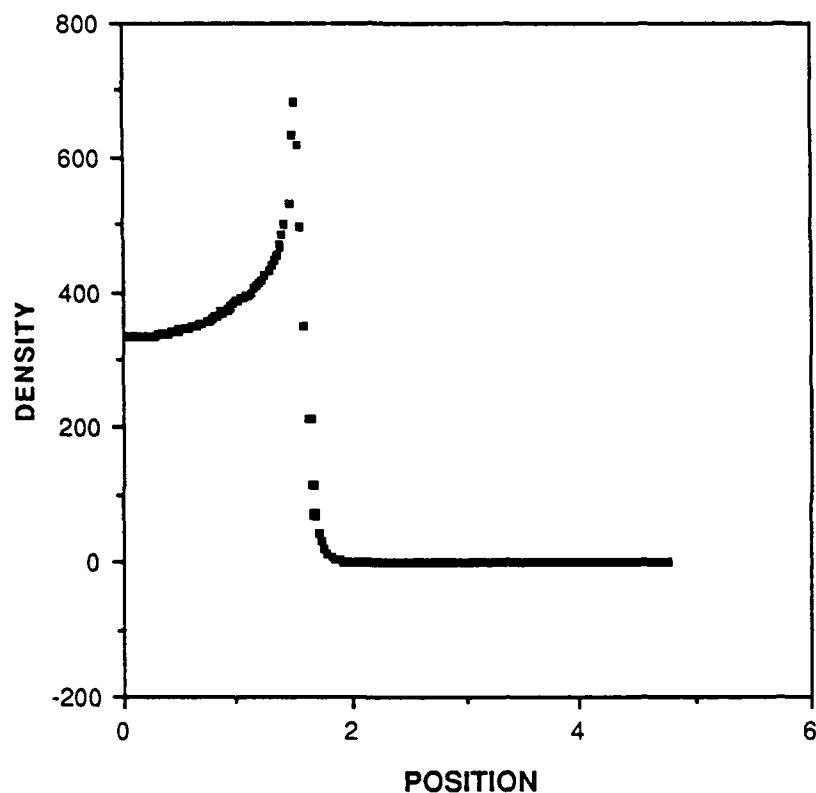


**FIGURE 4.26:** Rail current density for a current optimized railgun. Referring to Figure 4.18,  $r_t = 0.641$  cm and  $A_r/A_g = 1.0002$ ;  $r_p$  was fixed at the bore radius of 2.257 cm and the rail angle,  $\alpha$ , was fixed at  $40^\circ$ . This railgun produces a projectile force of 1.090 MN. It has a rail current of 0.744 MA and a guard plate current of 4.588 MA.

in  $\alpha$ , it was determined that  $2.5^\circ$  increments in  $\alpha$  were sufficiently small.

As was done for the results of force optimized guard plates, current distributions and accelerator scale drawings are only provided for the case in which the guard plate density was limited to 2.0 MA/inch. These are presented in Figures 4.27 through 4.29. Note that the ratio of the peak current density to that on the center of the inside of the rail is only approximately 2:1, while the same ratio for the simple railgun on Figure 4.15 is 5:1. Additionally, the top and back surface current shown in Figure 4.28 is negligible compared to the current on the inside rail surface. The force calculation assumes peak densities of one and two MA/inch for the rail and guard plate, respectively.

The remaining results for the current optimizations are presented in tabular form. As for the force optimizations, results are divided into two categories. The first category involves current-optimizations which were accomplished with guard plates precluded from overhanging the rails and extending into the bore. For the second category, no restrictions were placed on the guard plate overhang.

# CURRENT-OPTIMIZED, ROUND-BORE RAILGUN WITH GUARD PLATES

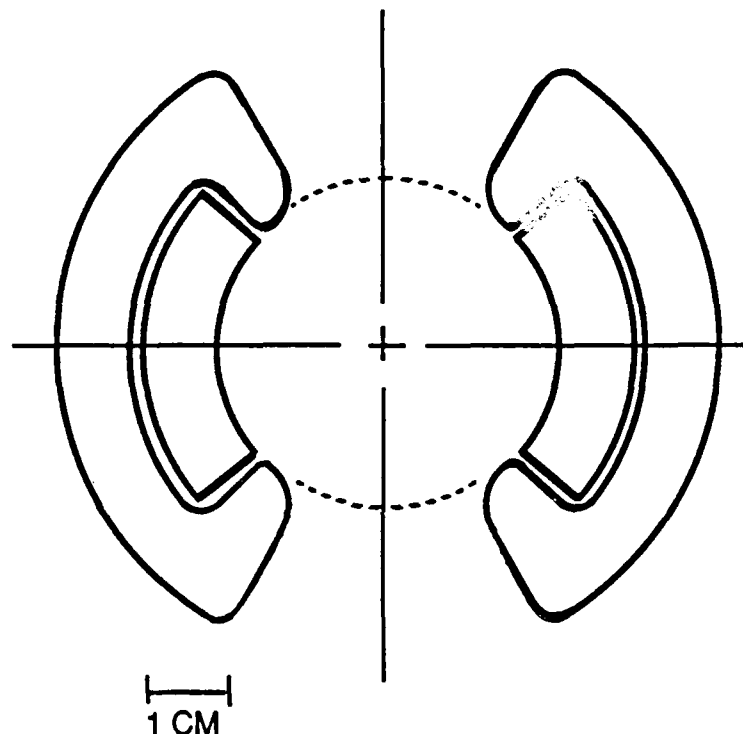


**FIGURE 4.27:** Scale drawing of a round-bore railgun with guard plates optimized for current. Referring to Figure 4.18,  $r_t = 0.641$  cm,  $\alpha = 40.0^\circ$ , and  $A_r/A_g = 1.00021$ . For this optimization,  $r_p$  was fixed at the bore radius of 2.257 cm.

# NORMALIZED RAIL CURRENT DENSITY TWO-RAIL RAILGUN WITH GUARD PLATES

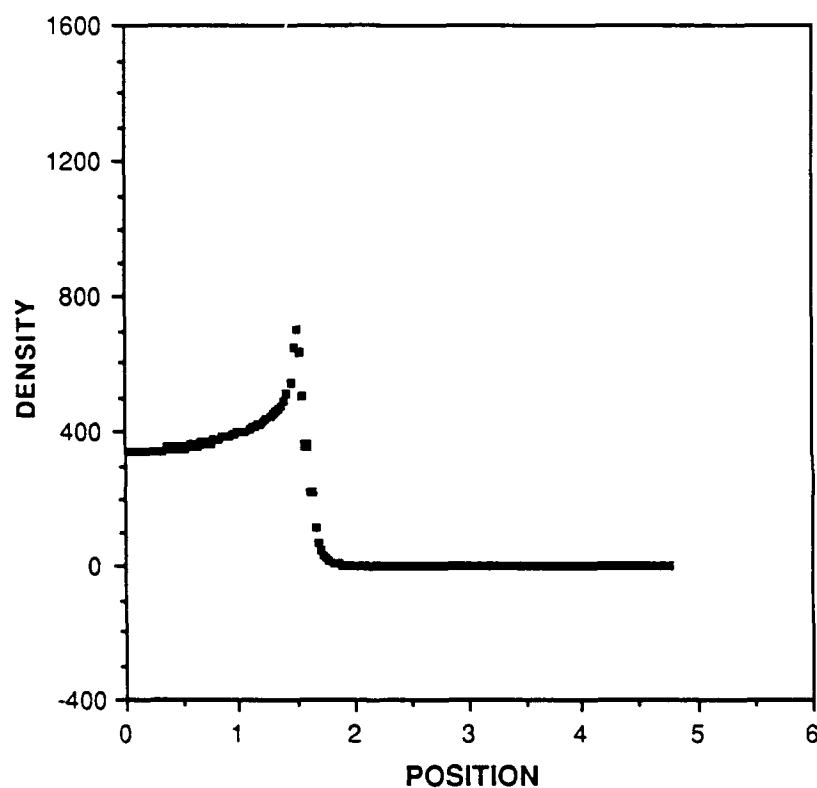


**FIGURE 4.28:** Normalized rail current density for the railgun with guard plates of Figure 4.27. Force developed with this gun is 1.09 MN, with a rail current of 0.744 MA and a guard plate current of 4.588 MA. This calculation invokes limits of  $\leq 1\text{MA}$  and  $\leq 2\text{MA}$  for maximum, allowable, density peaks in the rails and guard plates, respectively.

# NORMALIZED GUARD PLATE CURRENT DENSITY TWO-RAIL RAILGUN WITH GUARD PLATES

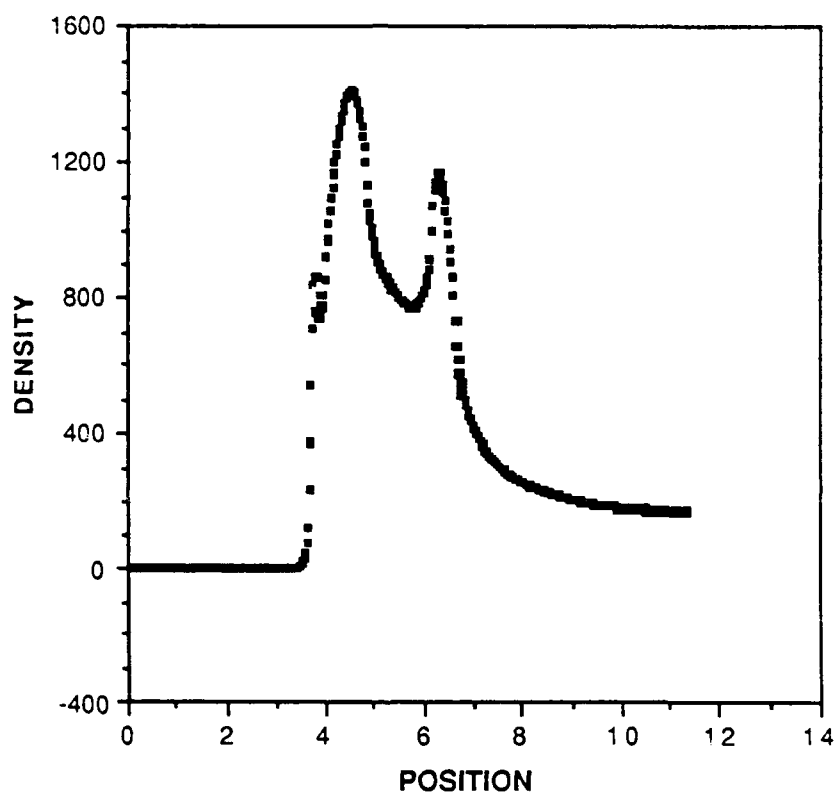


**FIGURE 4.29:** Normalized guard plate current density for the railgun of Figure 4.27. This plot is the companion plot of Figure 4.28.



**TABLE 4.6**  
**CURRENT OPTIMIZATION RESULTS**  
**(ROUND BORE)**

Max Guard Density (MA/in)	$A_r/A_g$	$r_t$ (cm)	Overhang ( $r_r - r_p$ ) (cm)	$\alpha_r$ (deg)	Force (MN)	Rail Current (MA)	Guard Current (MA)
1.0	1.00024	0.650	-0.274	30.00	0.528	0.532	2.263
1.5	1.00021	0.650	-0.070	32.50	0.813	0.609	3.446
2.0	1.00021	0.641	0.000	40.00	1.090	0.744	4.588
3.0	1.00020	0.274	0.000	42.50	1.213	0.798	5.193
2.0	1.00019	0.650	0.043	30.00	1.176	0.658	4.617
3.0	1.00018	0.650	0.155	32.50	2.052	0.837	7.007

Examination of the above table illustrates the effects of constraints on certain variables. For example, the first two rows have a guard plate top radius of 0.65 cm ( $r_t$  in Figure 4.18), the maximum possible. Even for this maximum radius, to keep the peak guard plate current density (relative to the rail density) below its imposed limit, it is necessary to have a negative guard plate overhang, i.e.,  $r_p$  in Figure 4.18 is greater than the rail radius. The next two rows have imposed limits of zero overhang, which were not required in the first two rows to prevent the guard plate from protruding into the bore. This

results in decreased guard plate top radii,  $r_t$ . A final observation concerning this table is that large guard plate currents are required, compared to those for the force optimizations.

#### 4.8 Chapter Conclusion

Several conclusions can be drawn from results presented in this chapter. The most obvious conclusion, from the force optimization results, is that accelerators with wrap-around guard plates can produce up to seven times the force produced by simple railguns or normal augmented railguns -- without increasing local peak current densities. The actual performance obtained, for a particular choice of relative rail and guard plate current densities, is primarily a function of the complexity of design. The more complex designs involve allowing guard plates to overhang rails slightly (protruding into the bore space, similar to rifling in a conventional gun barrel), and the use of separate power supplies for the rail and guard plate conductors. These added complexities represent unacceptable complications for many applications, but may be justifiable for others. For example, many conceptual designs for high-energy railgun systems already envision several power supplies in order to generate the high power levels required. Additionally, segmenting the guard plate into a few, properly-proportioned "slices" which are wired in series with each other and with the rails, may provide the high total currents required in the guard plates, while still requiring only one power source. At the lower end of the performance range, simple series-wired guard

plates, with no overhang protruding into the bore, produce three times the force of simple railguns -- still a substantial benefit.

The performance enhancements just mentioned represent force improvements obtainable without increasing local current densities. However, Figures 4.20 and 4.23 indicate that the proportion of current on top and back rail surfaces is not improved over that of the simple two-rail railgun, shown in Figure 4.15. In fact, it appears somewhat worse, especially in Figure 4.20. The extent to which this increases the rail peak current density and increases the rail damage which occurs on the inner rail corners ( $s \approx 1.75$  in Figures 4.20 and 4.23) cannot be ascertained since the three dimensional current distribution in the vicinity of the armature is not accurately known at this time. However, it appears likely that operating the railgun associated with Figure 4.20 at the total currents indicated, may cause somewhat increased rail damage over the simple railgun associated with Figure 4.15.<sup>1</sup> To equalize damage levels and allow comparisons, it may be necessary to reduce the rail and guard plate currents below the levels indicated in the caption of Figure 4.20. It is anticipated, however, that the force produced by the railgun of Figure 4.20 will still represent a substantial improvement over that of the railguns discussed in Figures 4.14.

This leads to consideration of the railgun associated with Figure 4.28, which has a guard plate optimized for current distribution. In this case, top and backside rail current is nearly zero. Accordingly, rail damage associated with this gun should

---

<sup>1</sup>This does not change the conclusion that the peak guard plate current density should be 1.0, 1.5, 2.0, or 3.0 times as great as the peak rail current density. The relative rail and guard plate peak current densities are based on the absence of contact between the armature and the guard plate.

be less than that associated with Figure 4.15. This would allow for increasing rail and guard plate currents in order to equalize damage for appropriate comparisons. Again, the magnitude of this possible increase is not presently known. However, there is a good possibility that the railgun which ultimately produces the most force with a given amount of rail damage will be one which has been optimized for current distribution, such as the railgun associated with Figure 4.28.

## Chapter 5

### Four-Rail, Round-Bore Railguns with Current Guard Plates

#### Chapter Outline

5.1	Introduction. . . . .	162
5.2	Force-Optimized, Round-Bore Guard Plates for Four-Rail Railguns . . . . .	164
5.3	Current-Optimized, Round-Bore Guard Plates for Four-Rail Railguns. . . . .	173
5.4	Chapter Conclusion . . . . .	178

#### 5.1 Introduction

This chapter presents results of research seeking to apply the guard plate concepts of Chapter 4 to multiple-rail railguns. The objective of this research was to develop viable accelerator designs having both the widespread utility of round-bore railguns *and* the desirable distribution of outward rail forces which is inherent with multi-rail railguns. To facilitate comparisons with previous chapters, the guiding tenets of this study are identical with those presented in Section 4.1 for two-rail railguns with guard plates. Furthermore, as in Chapter 4, passive current-shaping measures were not applied to railgun rails. Therefore, the only rail cross-sectional shapes

considered were 1.0 cm thick, circular segments, as in Figure 4.14, with sharp rail-corners (corner radii = 0.1 cm).

Previous results concerning simple multi-rail railguns and two-rail railguns with guard plates allowed the following features to be incorporated into this study of multi-rail railguns with guard plates:

- (1) The computational and optimization techniques developed in previous chapters were used without change.
- (2) Only four-rail railguns with guard plates were considered. This simplification was appropriate because Chapter 3 results indicated that four-rail railguns experience less aggravated proximity effects than six- or eight-rail railguns, which leads to a greater force-producing capability (for the same imposed local peak current density limits).
- (3) Only wrap-around guard plates were considered because Chapter 4 results indicated that the wrap-around design is the most effective.
- (4) The optimization variables and procedures developed in Chapter 4 for the wrap-around guard plates (see Section 4.6 and Figure 4.18) were used without change. Additionally, the guard plate geometric parameters that were not allowed to vary, were fixed at the same values specified in Section 4.6.

As in Chapter 4, projectile force was maximized with guard plate peak current densities of 1.0, 1.5, 2.0, and 3.0

MA/inch, and current distribution was optimized for the same four guard plate peak current densities. In all cases, rail peak current density was limited to 1.0 MA/inch. Results for these optimizations are presented in the next two sections.

## **5.2 Force-Optimized, Round-Bore Guard Plates for Four-Rail Railguns**

This section presents results of force optimizations. Figure 5.1 through Figure 5.3 display results obtained for the case in which the guard plate peak current density is 2.0 MA/inch (rail current density is 1.0 MA/inch). Guard plates were allowed to overhang the rail, protruding into the bore, for these optimizations. Results of similar optimizations, performed with the guard plate top radius ( $r_p$  in Figure 4.18) equal to the bore radius, are displayed in Figure 5.4 through Figure 5.6. Figures 5.1 and 5.4 both illustrate a significant limitation of multi-rail railguns with guard plates. Recall that the thickness of the portion of guard plate above and below the rail ( $t_t$  in Figure 4.18) was fixed at 0.75 cm. As a result, a 16 square-centimeter, round-bore, four-rail railgun has approximately 150° of bore circumference occupied by guard plate material. This leaves a limited portion of the bore perimeter to be occupied by magnetic flux and the four rails. Reducing  $t_t$  can alleviate this crowding problem, but can also introduce thermal problems in the guard plates.

As in Chapter 4, results for force optimizations invoking the other guard plate current densities (1.0, 1.5, and 3.0 MA/inch) are presented in tabular form only. In Table 5.1, the

variable names at the top of each column refer to the variables depicted in Figure 4.18. Values for rail and guard plate currents represent total railgun rail and guard plate currents, not the current flowing in each rail or guard plate. The current in one rail or guard plate is half the value displayed in the table. Table 5.1 is divided into two categories. The first category involves force optimizations which were accomplished with guard plate top radii ( $r_p$  in Figure 4.18) fixed at the bore radius. For the second category, no restrictions were placed on  $r_p$ . Trends displayed in Table 5.1 are similar to those displayed in Table 4.5 for the two-rail force optimization. One significant difference between Table 4.5 and 5.1 is the magnitude of the ratio of vector potentials,  $A_r/A_g$ . For the four-rail case, there is an aggravated proximity effect between neighboring guard plates which necessitates a higher vector potential in the rails, relative to the guard plate vector potential. Otherwise, local peak guard plate current densities would be too large relative to the rail local peak current densities i.e., guard current density would be more than 1.0, 1.5, 2.0, or 3.0 times as great as the peak rail current density.



**TABLE 5.1**  
**FORCE OPTIMIZATION RESULTS**  
 (FOUR-RAIL, ROUND BORE)

Max Guard Density (MA/in)	$A_r/A_g$	$r_t$ (cm)	Overhang ( $r_r - r_p$ ) (cm)	$\alpha_r$ (deg)	Force (MN)	Rail Current (MA)	Guard Current (MA)
1.0	1.26127	0.650	0.000	8.76	0.736	1.738	2.498
1.5	1.20549	0.650	0.000	12.04	0.947	1.891	4.205
2.0	1.19050	0.642	0.000	14.26	1.059	2.008	5.695
3.0	1.18335	0.629	0.000	16.63	1.158	2.135	8.422
1.5	1.19657	0.650	0.131	8.95	0.999	1.746	4.489
2.0	1.17707	0.650	0.199	9.93	1.232	1.864	6.290

# FORCE-OPTIMIZED, ROUND-BORE, FOUR-RAIL RAILGUN WITH GUARD PLATES

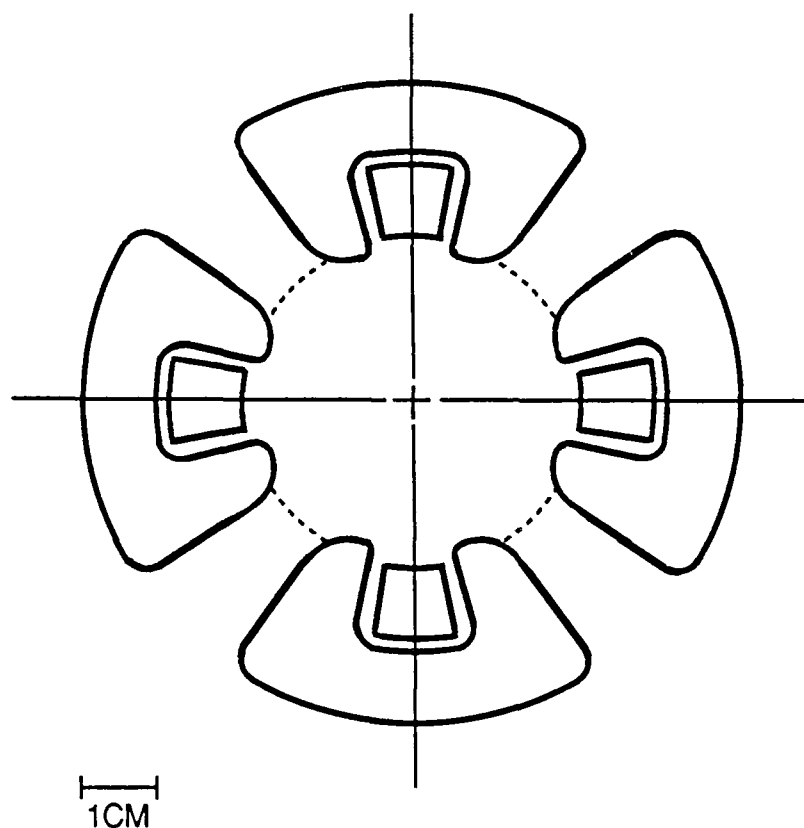


**FIGURE 5.1:** Scale drawing of a round-bore, four-rail railgun with guard plates optimized for maximum force. Referring to Figure 4.18,  $r_t = 0.650$  cm,  $r_p = 2.057$  cm,  $\alpha = 9.93^\circ$ , and  $A_r/A_g = 1.17707$ . The guard plates overhang the rails and protrude into the bore 0.199 cm, i.e., bore radius minus  $r_p$  equals 0.199 cm.

# NORMALIZED RAIL CURRENT DENSITY FOUR-RAIL RAILGUN WITH GUARD PLATES

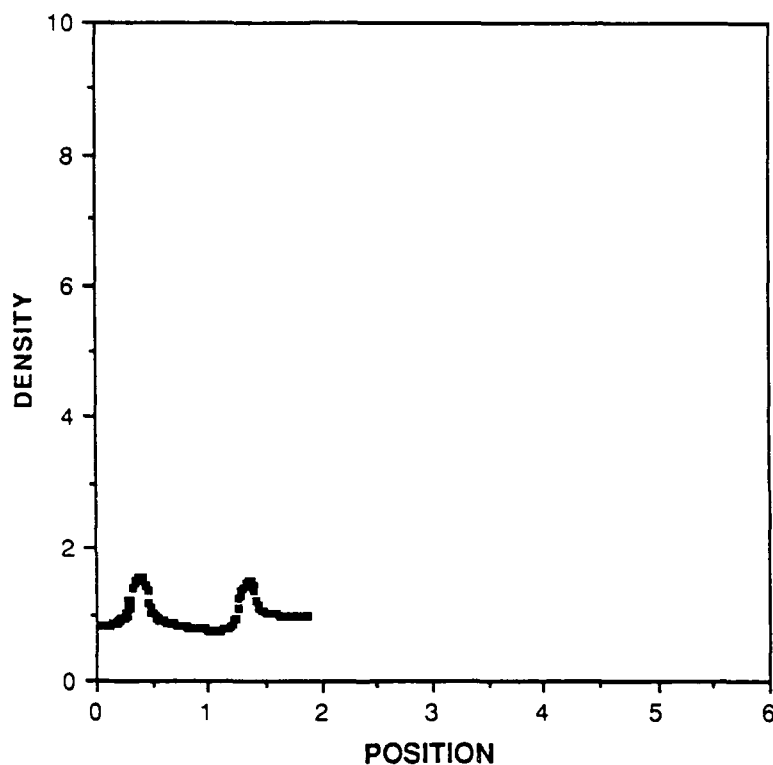


**FIGURE 5.2:** Normalized rail current density for the railgun with guard plates of Figure 5.1. Force developed with this gun is 1.23MN, with a total rail current of 1.86MA and a total guard plate current of 6.29MA. This calculation invokes limits of  $\leq 1\text{MA}$  and  $\leq 2\text{MA}$  for maximum, allowable, current density peaks in rails and guard plates, respectively. Scales for this plot are the same as in Chapter 4 to facilitate comparison.

**NORMALIZED GUARD PLATE CURRENT DENSITY**  
FOUR-RAIL RAILGUN WITH GUARD PLATES

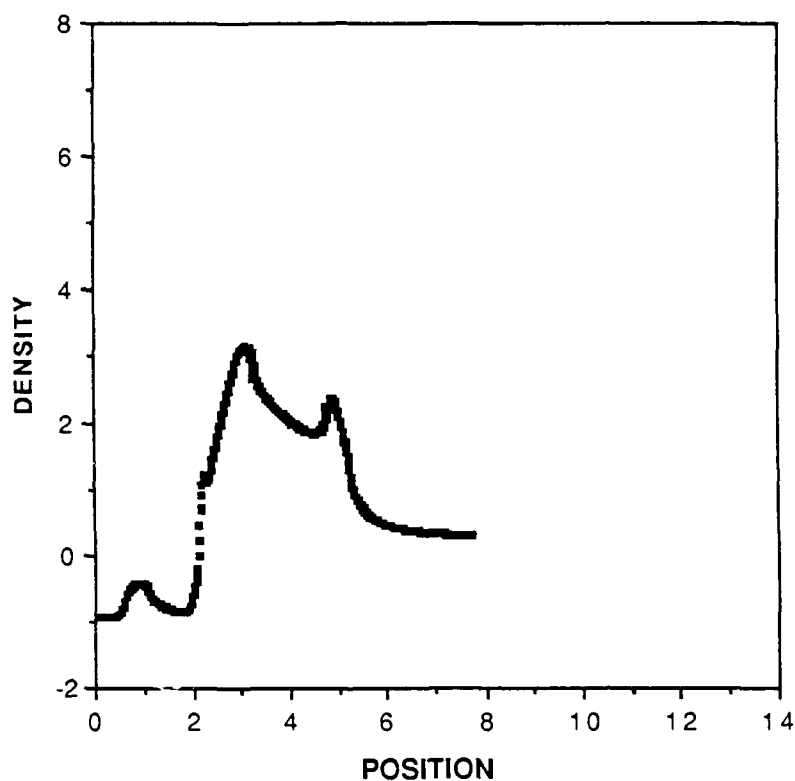


**FIGURE 5.3:** Normalized guard plate current density for the railgun of Figure 5.1. This plot is the companion plot of Figure 5.2.

**FORCE-OPTIMIZED, ROUND-BORE, FOUR-RAIL  
RAILGUN WITH GUARD PLATES**

(Without Overhang)

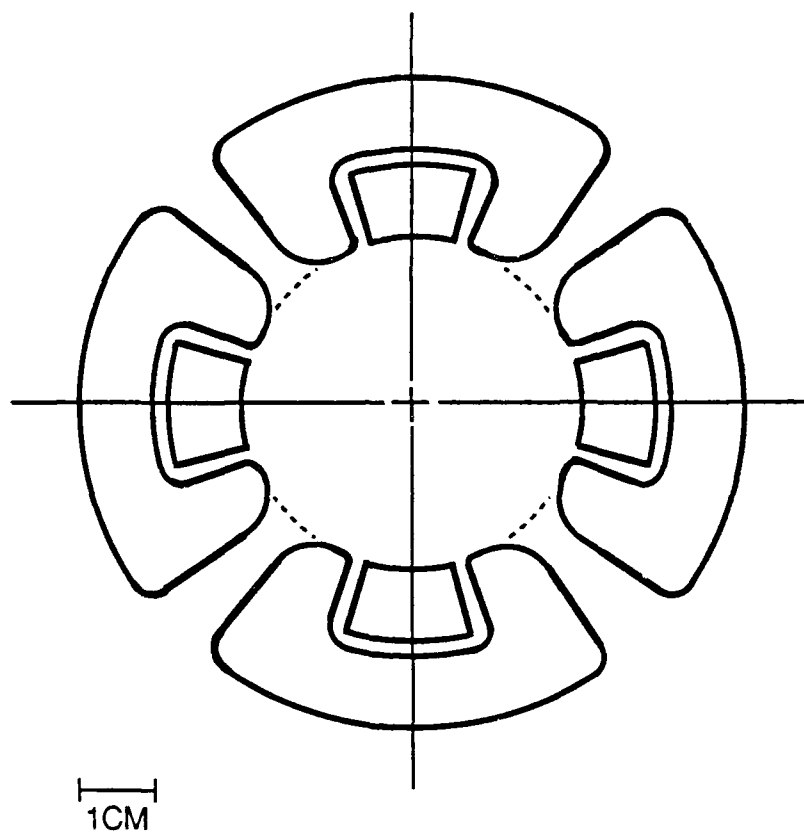


**FIGURE 5.4:** Scale drawing of a round-bore, four-rail railgun with guard plates optimized for maximum force. Referring to Figure 4.18,  $r_t = 0.642$  cm,  $\alpha = 14.26^\circ$ , and  $A_r/A_g = 1.19050$ . For this optimization,  $r_p$  was fixed at the bore radius of 2.257 cm.

# NORMALIZED RAIL CURRENT DENSITY FOUR-RAIL RAILGUN WITH GUARD PLATES

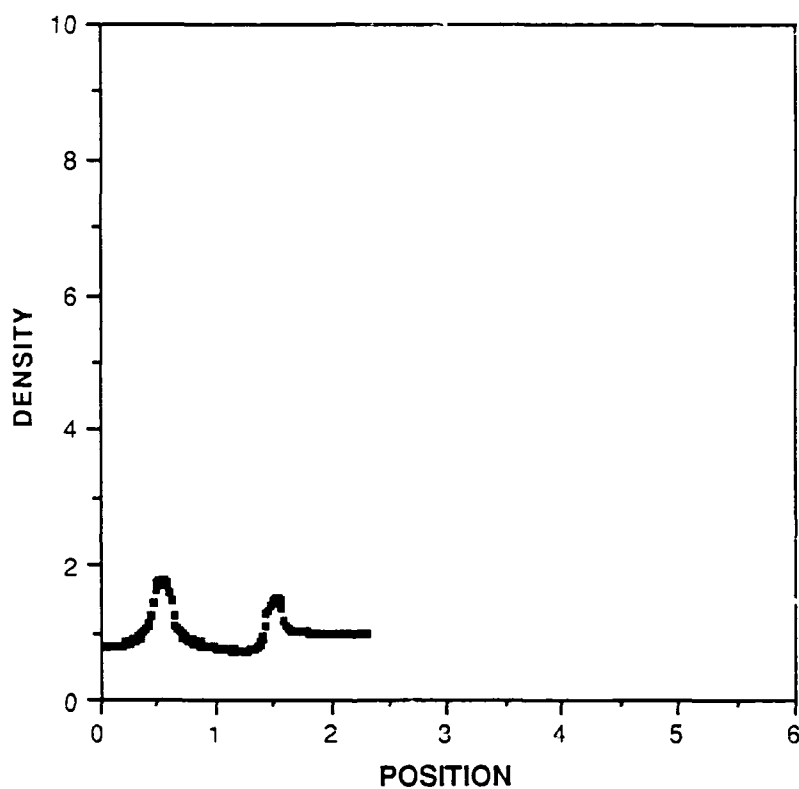


**FIGURE 5.5:** Normalized rail current density for the railgun with guard plates of Figure 5.4. Force developed with this gun is 1.06MN, with a total rail current of 2.01MA and a total guard plate current of 5.70MA. This calculation invokes limits of  $\leq 1\text{MA}$  and  $\leq 2\text{MA}$  for maximum, allowable, current density peaks in rails and guard plates, respectively. Scales for this plot are the same as in Chapter 4 to facilitate comparison.

**NORMALIZED GUARD PLATE CURRENT DENSITY**  
FOUR-RAIL RAILGUN WITH GUARD PLATES

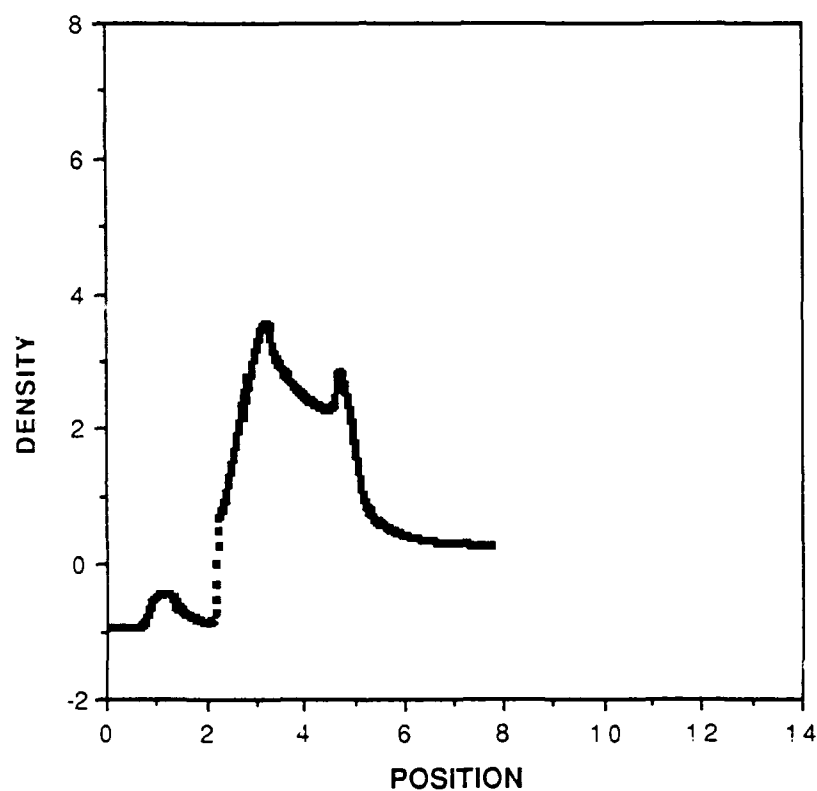


**FIGURE 5.6:** Normalized guard plate current density for the railgun of Figure 5.4. This plot is the companion plot of Figure 5.5.

### 5.3 Current-Optimized, Round-Bore Guard Plates for Four-Rail Railguns

This section presents results of current optimizations. As in Chapter 4, current optimizations were done in sequences. For each of the four, specified, guard plate peak current densities (1.0, 1.5, 2.0, and 3.0 MA/inch), rail current optimizations were performed with successively larger rail angles,  $\alpha_r$ . The intent was to find accelerator geometries with good current and force characteristics. Although  $2.5^\circ$  increments in  $\alpha_r$  were used in Chapter 4 for two-rail railguns,  $1.0^\circ$  increments were used in these four-rail optimizations. This smaller increment was necessary due to the smaller rail angles employed by the four-rail railguns (compare  $\alpha_r$  in Table 4.5 and Table 5.1).

Figure 5.7 through 5.9 display results obtained for the case in which the guard plate peak current density is 2.0 MA/inch (rail current density is 1.0 MA/inch). Results of all current optimizations are presented in Table 5.2. Trends displayed in Table 5.2 are similar to those displayed in Table 4.6 for two-rail railguns with guard plates. One exception to the trends in Table 5.2 is the large rail current contained in the first row, (maximum guard plate density of 1.0 MA/inch). This large rail current results from the large negative overhang of the guard plate which leaves over half of the rail top and bottom surfaces uncovered by guard plate. Consequently, these rail surfaces have higher current densities than normally found with other guard plate designs. The current optimization for this case (guard plate peak density equal to the rail peak current density) was



repeated with several different sets of starting values for the optimization variables to verify the results.

**TABLE 5.2**  
**CURRENT OPTIMIZATION RESULTS**  
 (FOUR-RAIL, ROUND BORE)

Max Guard Density (MA/in)	$A_r/A_g$	$r_t$ (cm)	Overhang ( $r_r - r_p$ ) (cm)	$\alpha_r$ (deg)	Force (MN)	Rail Current (MA)	Guard Current (MA)
1.0	1.00063	0.650	-0.511	11.00	0.334	0.656	3.625
1.5	1.00052	0.650	-0.228	11.00	0.389	0.586	5.678
2.0	1.00043	0.650	-0.127	12.00	0.462	0.603	7.571
3.0	1.00036	0.650	-0.009	12.00	0.620	0.610	11.469

CURRENT-OPTIMIZED, ROUND-BORE, FOUR-RAIL  
RAILGUN WITH GUARD PLATES

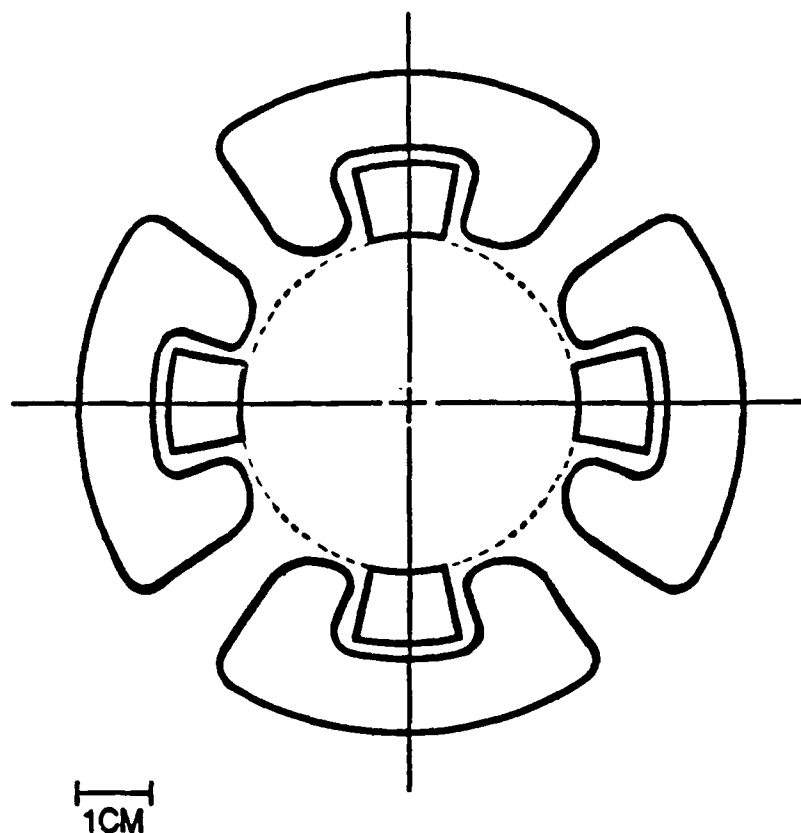


**FIGURE 5.7:** Scale drawing of a round-bore, four-rail railgun with guard plates optimized for current. Referring to Figure 4.18,  $r_t = 0.650$  cm,  $r_p = 2.38$  cm,  $\alpha = 12^\circ$ , and  $A_r/A_g = 1.00043$ .

# NORMALIZED RAIL CURRENT DENSITY FOUR-RAIL RAILGUN WITH GUARD PLATES

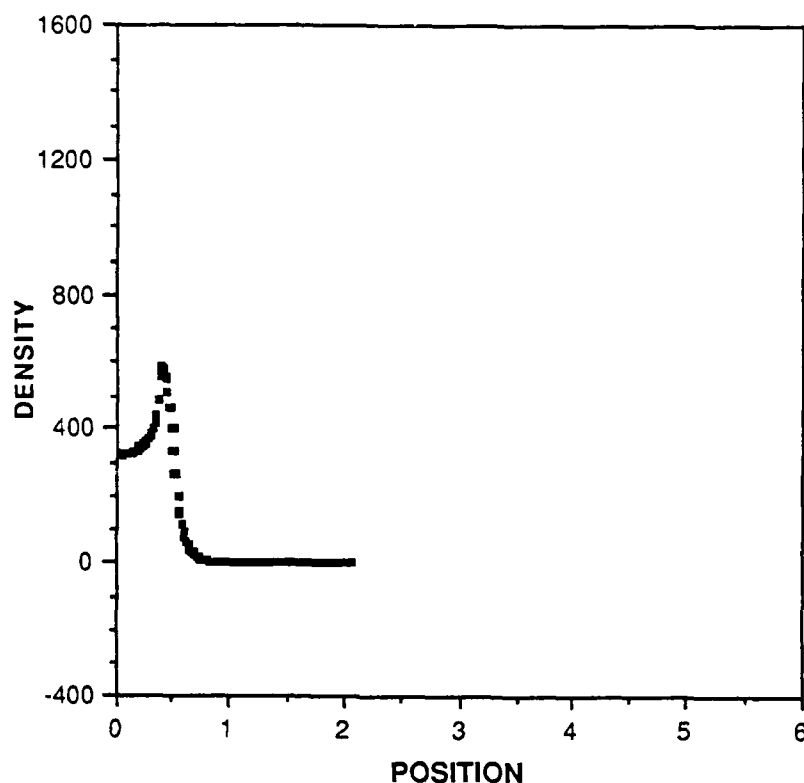


**FIGURE 5.8:** Normalized rail current density for the railgun with guard plates of Figure 5.7. Force developed with this gun is 0.46MN, with a total rail current of 0.60MA and a total guard plate current of 7.57MA. This calculation invokes limits of  $\leq 1\text{MA}$  and  $\leq 2\text{MA}$  for maximum, allowable, current density peaks in rails and guard plates, respectively. Scales for this plot are the same as in Chapter 4 to facilitate comparison.

**NORMALIZED GUARD PLATE CURRENT DENSITY**  
**FOUR-RAIL RAILGUN WITH GUARD PLATES**

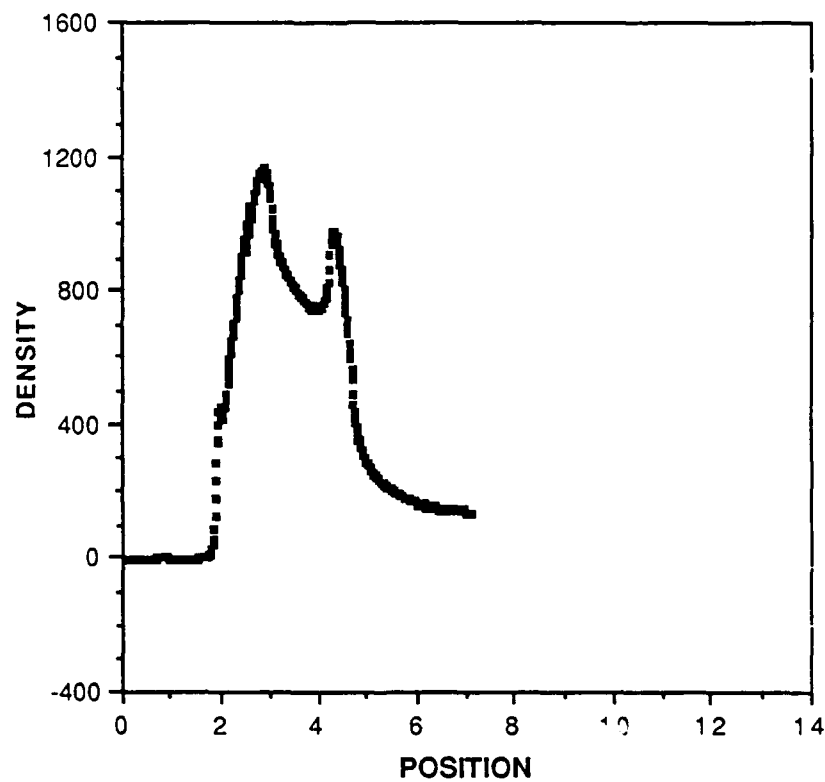


**FIGURE 5.9:** Normalized guard plate current density for the railgun of Figure 5.7. This plot is the companion plot of Figure 5.8.

#### 5.4 Chapter Conclusion

The most obvious conclusion from the force optimization results contained in Table 5.1 is that guard plates make it possible to design four-rail, round-bore railguns which can produce 2 to 3.5 times as much force as the simple, two-rail, round-bore railgun (see Table 4.4), with the same local peak current density limits. Current optimization results indicate that it is also possible to design four-rail, round-bore railguns with good force characteristics and significantly improved current distributions, compared to simple two-rail railguns. The comments contained in Section 4.8, concerning the relative merits of force-optimized designs and current-optimized designs for two-rail railguns, also apply to four-rail railguns and will not be repeated here.

## Chapter 6

### Concluding Remarks

#### Chapter Outline

6.1	Introduction. . . . .	179
6.2	Recovered Projectiles . . . . .	182
6.3	Design Implementation. . . . .	192
6.4	Summary and Conclusions . . . . .	206

#### 6.1 Introduction

The objective of this dissertation was to investigate the potential for managing rail current to overcome existing railgun deficiencies. The approach used was to optimize railgun force-producing capability, subject to a specified, local current density constraint. This approach compares railguns by their ability to perform their primary function i.e., accelerate projectiles, while not aggravating their primary, current-provoked limitation, heat-related rail damage. However, this approach only addresses one aspect of a very complex problem.

During armature acceleration, several interdependent mechanisms contribute to rail damage. These include: Joule heating; frictional heating between rails and solid armatures; heating due to the contact voltage drop between rails and armatures; mechanical damage, such as rail gouging by solid

armatures; localized arcing between rails and solid armatures; heat transferred from plasma armatures to rails; formation of a plasma layer between rails and solid armatures at high speeds; degraded rail-armature contact due to rail flexing and material deformation; and the effective reduction of electrical contact surface between rails and armature due to velocity skin effects. These damage mechanisms, as well as their interactions, and their relative importance under typical, railgun operating conditions, are not adequately understood at this time. Additionally, these damage mechanisms are not only interrelated, but also very dependant on factors such as accelerator geometry, projectile geometry, current pulse shape, rail material properties, armature material properties, and armature velocity profiles. The relationship between the damage mechanisms and these additional factors is also not adequately understood. Consequently, controlled railgun experiments to accurately evaluate potential improvements with regard to individual damage mechanisms are not possible at this time.

Due to the difficulties in experimentally investigating individual damage mechanisms, the popular approach is to design and build an experimental, "state-of-the-art" accelerator, with some innovative design feature. This generally requires the efforts of an engineering team to incorporate the recent advances in mechanical, electrical, and thermal analysis of railgun accelerators. Then, after each railgun shot, the used rails, recovered armature, and data collected by diagnostic equipment are examined for some evidence of improvement.

Unfortunately, this approach is expensive and the results are often inconclusive, if not misleading.

This dissertation explores improving railgun performance without aggravating current density-provoked rail damage. As a consequence of the difficulties in isolating rail damage mechanisms, results allowing definitive, experimentally-verified conclusions, concerning multi-rail and guard plate current management techniques, are not available. However, the limitations of experimental results do not eliminate the need for a serious design, fabrication, and testing effort as the next logical step in the development of these current management concepts. An appropriate experimental program requires railguns with bores sufficiently large to allow geometric flexibility and easy fabrication, and projectile energies sufficiently high to tax the designs, devices, and concepts. It is likely that an experimental program of this type would require at least two iterations: design, fabricate, test, and analyze; redesign, fabricate, test, and analyze.

As a dissertation conclusion, this chapter presents some general remarks intended to assist railgun designers in implementing multi-rail and guard plate concepts. It is intended to be especially useful in the initiation of a design and testing program for railguns that employ these current management concepts. As in previous chapters, there is no attempt to make this chapter a source for charts, tables, or graphs to allow design of improved railguns that meet specific railgun objectives.

The first topic in this chapter concerns relevant observations involving some of the many UT-CEM armatures



which have been successfully recovered after railgun shots. For two reasons, recovered armatures are the most readily available historical record of damage caused by electric current during railgun shots. First, economics dictate that rails be used for many shots (often with honing between shots) before accelerator disassembly. In contrast, armatures are used for only one shot. Second, damage is usually more pronounced in armatures than in rails. This is because armatures suffer the effects of friction and contact voltage drop for the entire acceleration period, and carry the full railgun current in a more restricted area than do rails. As a result, even low power railgun shots with little or no rail damage often produce interesting armature damage. Following the armature discussion, Section 6.3 provides general remarks concerning implementation of multi-rail and guard plate concepts. Finally, Section 6.4 provides a brief summary of dissertation results.

## **6.2 Recovered Projectiles**

The objective of this section is to highlight the importance of designing projectiles and armatures in conjunction with designing accelerators. To accomplish this objective, photographs are provided of several UT-CEM armatures which have been successfully recovered with some form of "soft-catch" device (typically a barrel of rags or water). All photographs involve a 45 mm, two-rail, round-bore, simple railgun. The railgun which fired these projectiles was specifically designed to be "stiff," i.e., considerable effort was

expended to minimize rail flexing. This stiffness is credited with the fact that rail damage in this railgun was atypically minor (Price, et al., 1989). Although the railgun shots discussed in this section were not part of the research for this dissertation, they provide insights which may be useful when attempting to employ multi-rail and guard plate concepts. However, the reader should be cautioned against trying to infer too much information from these photographs. As mentioned previously, many interrelated damage mechanisms are involved and recovered armatures from other railguns may lead to different conclusions.

Figure 6.1 shows a 45 mm armature consisting of two circular rings of conducting fingers. The view in the photograph is of three fingers which contacted one rail. Due to switch failure, this particular shot was at low power. The concentration of damage in the rear section is due to velocity skin effects (see Long 1987). Damage is also concentrated in the portions of armature which were in contact with rail corners, as might be expected from rail current distributions provided in previous chapters. Figure 6.2 shows a piece of recovered armature similar to the armature of Figure 6.1. This was a high power shot. The recovered armature section corresponds to the rear circular ring of armature fingers in Figure 6.1. Again, damage is more severe in the portions of armature adjacent to rail corners (the area close to the pencil lead).

Figure 6.3 shows the entire, integrated, projectile-armature assembly corresponding to Figure 6.1. The projectile portion, which has no electrical function, is the solid cylinder



**FIGURE 6.1:** Armature portion of an integrated armature-projectile assembly which was recovered after a very low-power railgun shot. This picture shows the three fingers which contacted one rail. The entire armature-projectile assembly is shown in Figure 6.3.



**FIGURE 6.2:** Recovered portion of an armature from a high-power railgun shot. The armature fingers which contacted one rail are shown. This armature was of the same type as shown in Figure 6.1.

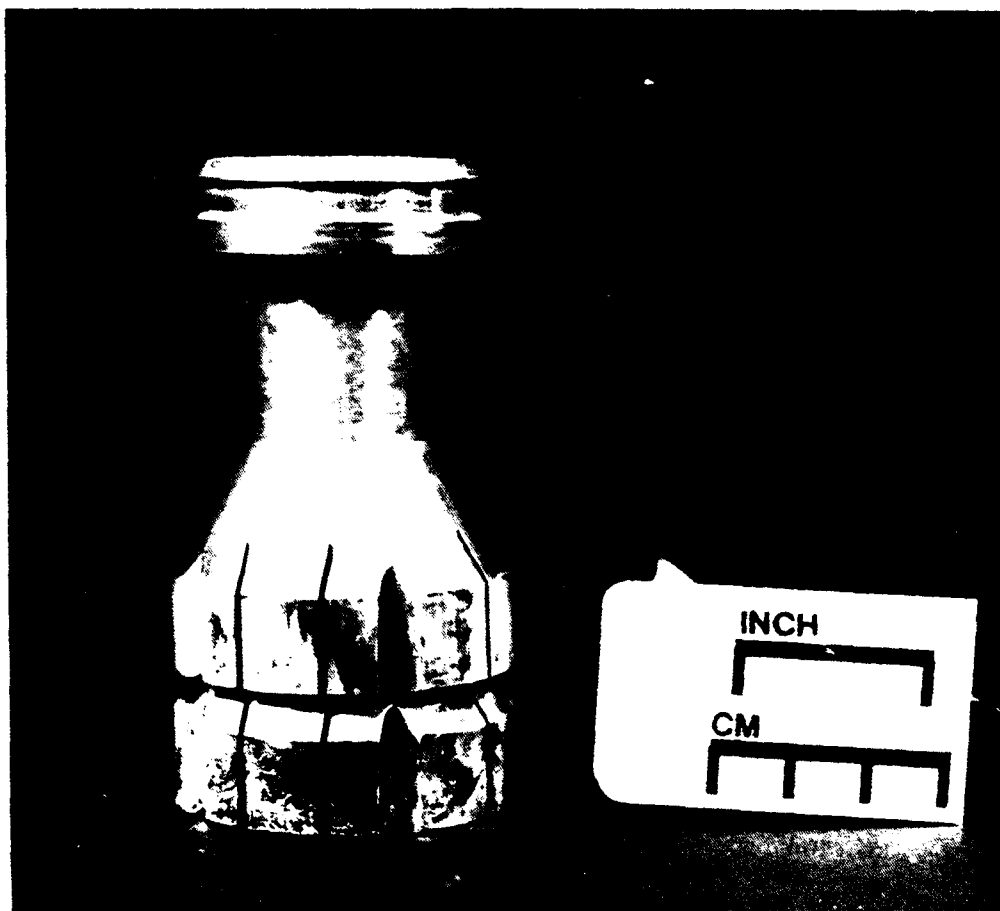


**FIGURE 6.2.** Entire, recovered armature-projectile assembly. This is a full view of the same armature-projectile assembly photographed in Figure 6.1.

and flat disk assembly attached to the top of the armature. The disk serves as a "bore-rider" for in-bore stability, and is insulated from the rails during acceleration. This figure is particularly interesting because the view is of three armature fingers which were in contact with railgun dielectric. These fingers show more damage than the portions of armature in contact with rails (shown in Figure 6.1). The most prevalent theory for this damage maintains that it occurred while the projectile exited the railgun and the usual "muzzle arc" formed. However, there is another, generally ignored, effect which may also be significant. Recognizing that magnetic field lines in the bore behind the projectile close on themselves either outside the bore or in front of the projectile in the bore, it is natural to expect high field concentrations and high current densities along exposed, sharp corners on the armature (exposed sharp corners are armature corners not adjacent to a rail surface). The cavity back of the armature (visible in Figure 6.1) causes the fingers in contact with dielectric to be especially pronounced and results in high magnetic field concentrations as field lines curve toward the front of the projectile. The associated, high current densities may significantly contribute to armature damage in these fingers.

To reduce armature mass, later projectile designs eliminated the armature fingers in contact with dielectric. This resulted in armature-projectile assemblies similar to that shown in Figure 6.4, with "C"-shaped armatures. Figure 6.5 shows a recovered "C"-shaped armature. Again, damage is seen to be more severe in the regions of armature adjacent to rail corners. It should be noted that the two outside armature



**FIGURE 6.4:** Armature-projectile assembly. The projectile portion of this assembly is similar to that shown in Figure 6.3, but the armature portion is a solid "C" shape.



**FIGURE 6.5:** A recovered "C"-shaped armature. This armature is similar to that shown in Figure 6.4, except the legs of the "C" are composed of three fingers, instead of being solid. The surface of the armature which contacted one rail is shown.



fingers were shorter than the center finger before firing, so damage is not as severe it may appear. Figure 6.6 shows a recovered solid "C"-shaped armature fragment from a high power railgun shot. The circled portion of this photograph reveals damage to the inside curve of the back of the "C" which may be associated with magnetic field concentrations that can form as field lines curve toward the front of the projectile (as discussed in relation to Figure 6.3).

The closing of magnetic field lines in front of the armature is the same effect which results in high current densities on rail corners and causes 50% or more of the rail current to be carried on rail top and back surfaces. It is intriguing that effects of current on armature forward surfaces have not been more prominently apparent in recovered railgun armatures.

The objective of this section was to emphasize the degree to which armature geometry can adversely concentrate magnetic fields. Adequate understanding of this problem requires knowledge of three-dimensional, current distributions in the armature and adjoining rail segments. Although this information is not available at this time, it is clear that careful optimization of rail and guard plate geometries can be negated by poor projectile design. This is especially true with guard plates, due to their close proximity to the armature. Consequently, it is important that experimental design and testing programs for multi-rail railguns or railguns with guard plates be accompanied by experimental and analytical programs to improve understanding of current distribution in armatures. Although three-dimensional, analytical solutions are desirable,

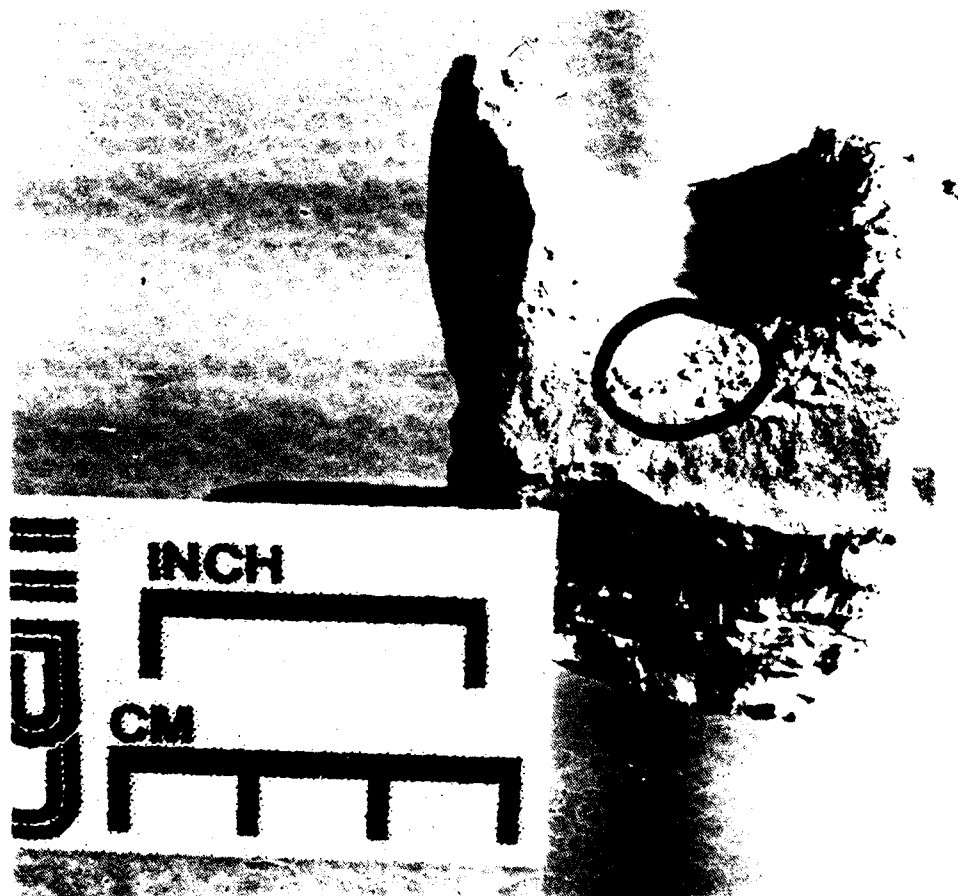


**FIGURE 6.6:** Recovered portion of a solid "C"-shaped armature. This armature is the same type shown in Figure 6.4. The circled region displays damage to the inside curve of the back of the "C."

perhaps much can be learned from carefully selected, simple two-dimensional calculations of infinite conductivity current distributions, using the techniques presented in Chapter 2.

### 6.3 Design Implementation

This section briefly discusses some issues which must be addressed when converting the concepts of previous chapters into actual accelerator designs to meet particular railgun objectives. The intention is not to present a manual on general railgun design, but to mention considerations which are somewhat unique to the railguns discussed in this dissertation. Comments concerning multi-rail railguns will be presented first, followed by guard plate design considerations. Most of this section is devoted to railguns with guard plates since implementing the multi-rail concepts of Chapter 3 is similar to building two-rail railguns (except for the number of rails).

The optimized, multi-rail accelerator of Figure 3.21 exacerbates two problems which already exist with simple, two-rail railgun systems. First, the low, four-rail inductance gradient is not well suited to existing pulse power supply options. This problem can significantly impact railgun system efficiency and size. One solution is to connect the four rails in series, making a two-turn accelerator. This requires two independent current paths through the armature, but increases the inductance gradient by four times, to  $0.672 \mu\text{H/m}$ . Despite increased accelerator resistance, this increased inductance gradient may allow overall system size reduction. The major

disadvantage is that armatures for series-fed railguns could be very difficult to develop. At high speeds, plasmas tend to form between the armature and rails. A series-connected, two-turn, four-rail, accelerator requires an armature which does not allow electrical shorting between the two, accelerator turns in the presence of these plasmas.<sup>1</sup> The second problem with four-rail railguns is that total armature current is increased, even though the current carried by individual rails is lower than for the two-rail railgun. For example, to produce equal armature force, the total current carried by the armature for the four-rail railgun is approximately 2.17 times that for the simple, square-bore, two-rail railgun (calculated based on the currents and inductance gradients in Figures 3.21 and 3.25). However, *peak* rail current in the four-rail railgun is only three-fourths that of the simple, two-rail railgun (again, for the same armature force). Consequently, well-designed armatures, without exposed sharp corners, may be able to carry the additional total current without severely aggravating armature damage. When considering armature design, it is important to note that some flexibility exists with the armature geometry. It is not mandatory that the entire bore area of Figure 3.21 be occupied by armature. Figure 6.7 depicts an armature for the same rail configuration shown in Figure 3.21, that is less likely to have regions with severe thermal problems.

The implementation of guard plate concepts will now be addressed. This involves a short discussion of two topics, bore

---

<sup>1</sup>This complication was first noted by Ray Zaworka, UT-CEM.

## ALTERNATE FOUR-RAIL ARMATURE

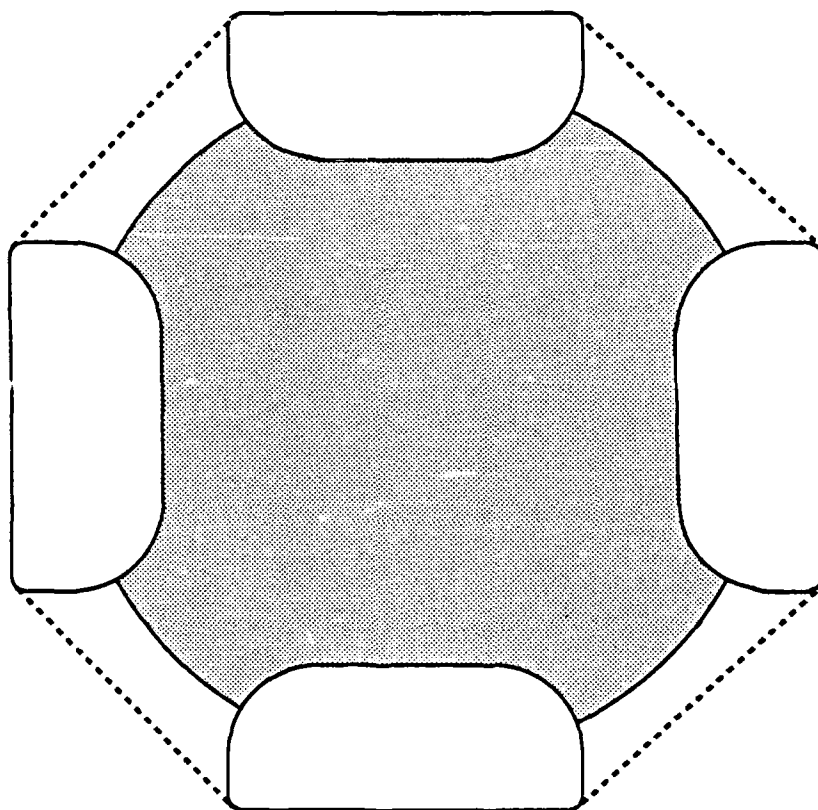


**FIGURE 6.7:** Alternate four-rail armature suitable for the railgun of Figure 3.21. The bore of Figure 3.21 is defined by dashed lines. The armature, shown as shaded, is essentially round, with slots for the rails.

size and current diffusion, and a more detailed discussion concerning interfacing with power supplies.

Bore size considerations can be summarized by stating that bigger is better. The thickness of the portion of guard plate above and below the rail ( $t_t$  in Figure 4.18) is dependent on thermal considerations. As mentioned in Chapter 4, electromagnetically it is beneficial to make this dimension as small as possible, but the required minimum thickness can be determined only after the power supply is specified and guard plate current as a function of time is known. However, once  $t_t$  is fixed, the proportion of bore circumference occupied by guard plate material is smaller for larger bores. This allows larger proportions of bore perimeter to be occupied by rail surface without aggravating proximity effects, and allows higher total rail and guard plate currents. Benefits are more significant for four-rail railguns with guard plates, which were found in Section 5.2 to be significantly limited by the bore circumference (recall, that for the four-rail railguns considered in Chapter 5,  $t_t$  was 0.75 cm, the bore radius was 2.26 cm, and 150° of bore perimeter was occupied by guard plate surfaces).

The second short topic to be discussed is current diffusion in guard plates. In Chapter 4, it was mentioned that guard plates were assumed to be energized by pulse power devices because uniform DC guard plate currents were less effective than pulsed surface currents.<sup>1</sup> The pulsed current distribution places guard plate current near the surface and closer to the rails, so guard plates have more effect on rail current

---

<sup>1</sup>Also, as a practical matter, the large, requisite guard plate currents can most readily be provided by pulse power supplies.

distribution. The pulsed current distribution also has peaks in those places that have the most effect on rail peak current densities. For computational purposes, rails and guard plates were approximated as infinitely conducting. In portions of rails close behind the armature, which have carried current for a very short time, the current is very close to the surface. However, due to current diffusion, guard plate current near the armature may not always be as close to the surface. Consequently, enhancements obtainable for railguns with guard plates will be somewhat less than calculated based on infinite conductivity current distributions.<sup>1</sup> Figure 6.8 presents an example of diffused current distribution, as a function of time, in railgun copper conductors. The effects of diffusion are seen to happen quickly, although the preponderance of current is reasonably close to the conductor surface through most of the acceleration time. Four reasonable steps are available to offset the effects of diffusion. First, space allowed for insulation between rail and guard plate can be minimized. For this dissertation, rail-guard plate separation was arbitrarily set at 0.2 cm, which is likely to be larger than necessary, unless the railgun is quite long. The second remedy recognizes that the infinite conductivity current distribution is one in which current resides on the conductor surface while magnetic fields inside the conductor are zero. Therefore, steps can be taken to cause the

---

<sup>1</sup>Although guard plate current diffusion diminishes the ability of guard plates to reduce rail current peaks, it should not significantly affect the accuracy of the calculated armature force per unit total rail current. As was the case with simple railguns, data from the UT-CEM small caliber, augmented railgun indicates that the inductance gradient calculated from the infinite conductivity current distribution is in excellent agreement with inductance gradients determined from measured current and acceleration.

guard plate current distribution to be in a thin surface region with low magnetic fields in the guard plate interior. One such arrangement could be a copper covering (one or two millimeters thick) on a core of magnetic material. The low resistivity copper is intended to be the primary, guard plate, current-carrying material, and the permeable magnetic core is intended to slow the diffusion of magnetic fields into the guard plate interior (see Equation 4.5). The third step which can be taken to offset the consequences of guard plate current diffusion, is to tailor the rail current so that it is reduced when the guard plate effectiveness is reduced. Then, even with reduced effectiveness, the guard plates can keep rail current peaks sufficiently low. The required drop-off in rail current during the latter portions of acceleration occurs naturally with most power supply options, and could be carefully controlled with a compulsator power supply. The fourth possible means of offsetting guard plate current diffusion, is to incorporate the concepts of distributed energy supply (DES) railguns. DES railguns are accelerators divided into several short, individually-powered segments. Two-rail, DES simple railguns have already been successfully demonstrated (Holland 1984), and DES guard plates should also be possible. With this concept, diffusion would be limited because guard plate segments would only be active for a short time. DES guard plates could be used with either DES rails or continuous rails.



## CURRENT DIFFUSION INTO A FLAT CONDUCTOR

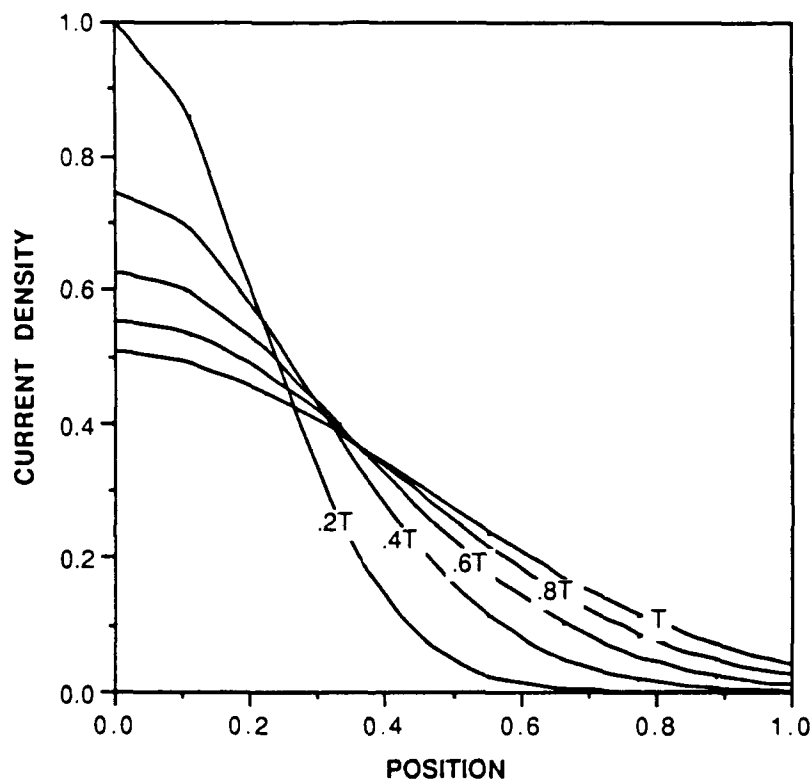


**FIGURE 6.8:** Plots of current density as a function of depth into a 1.0 cm thick, flat conductor. "T" is the acceleration time for a 1.5 meter railgun, assuming constant armature acceleration from zero to 2000 m/s. The instantaneous current distributions at the end of five, equal, time intervals are shown. The areas under each curve are equal. Plots are based on the magnetic diffusion equation solution presented in Knoepfel (1970, Equations 3.24 and 3.13)

The third guard plate topic, power supply considerations, will now be discussed. Previously, it was assumed that rails and guard plates would have independent power supplies. It was mentioned that this complication could be avoided by dividing guard plates into a few, properly-proportioned "slices" which are wired in series with each other and the rails. This series-connected system could have a high, effective inductance gradient, which is advantageous with many power supplies. The concept will be illustrated by an example.

Referring to Table 4.5, the accelerator to be considered is described by the third row. Noting that the guard plate current of 2.85 MA is approximately twice the rail current, the guard plate is split into two segments. Then, allowing the usual 0.2 cm spacing for insulation, the rail and guard plate cross-section are as depicted in Figure 6.9. All rail and guard plate geometric variables are as shown in the third row of Table 4.5 and in Figure 4.22. The right rail and each of the two, right, guard plate halves in Figure 6.9 carry equal currents in the same direction and the same applies for the left rail and guard plate segments. Consequently, the total current carried by each pair of guard plate segments is twice the current of the adjacent rail.

**FORCE-OPTIMIZED, ROUND-BORE RAILGUN  
WITH SPLIT GUARD PLATES  
(WITHOUT OVERHANG)**

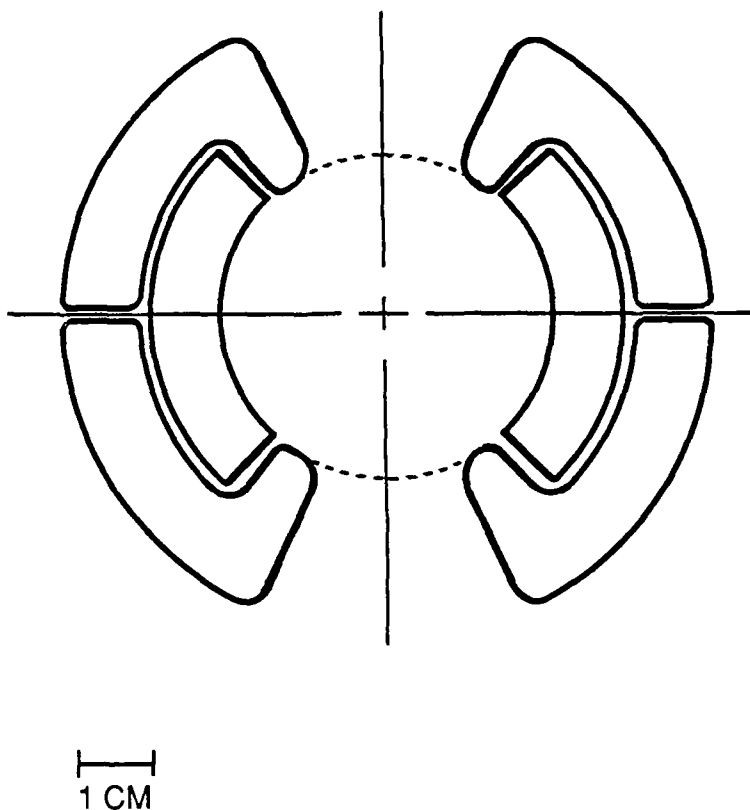


**FIGURE 6.9:** Identical accelerator as shown in Figure 4.22, except each guard plate has been split into two halves.

Figures 6.10 through 6.13 show relevant rail and guard plate current distributions for comparison. Figures 6.10 and 6.11 display current distributions for the rails and guard plates of Figure 4.22, with rail and guard plate vector potentials adjusted so that total guard plate current is exactly twice the total rail current. Performance parameters for this railgun are shown in Table 6.1 in column three. Column two of Table 6.1 displays the performance parameters for the railgun of Figure 4.22 with vector potentials optimized for force, as contained in Table 4.5 (rail current  $\neq$  twice guard plate current). Figures 6.12 and 6.13 display current distributions for the split guard plate railguns of Figure 6.9, with each guard plate segment, or slice, carrying the same current as the rails. The performance parameters for this railgun are shown in column four of Table 6.1. For this railgun, an effective inductance gradient can be obtained using  $F = .5 L' i^2$ .

**TABLE 6.1**  
**SPLIT GUARD PLATE PERFORMANCE COMPARISON**

Performance Parameter	Force-Optimized Railgun	Single Guard Plate, $I(\text{guard}) = 2 \times I(\text{rail})$	Split Guard Plate, $I(\text{guard segment})=I(\text{rail})$
Force	1.585 MN	1.529 MN	1.524 MN
Rail current	1.647 MA	1.532 MA	1.526 MA
Guard current	2.850 MA	3.064 MA	1.526 MA
Effective $L'$	N/A	N/A	1.309 $\mu\text{H/m}$

**NORMALIZED RAIL CURRENT DENSITY**  
**TWO-RAIL RAILGUN WITH GUARD PLATES**  
(Without Overhang)

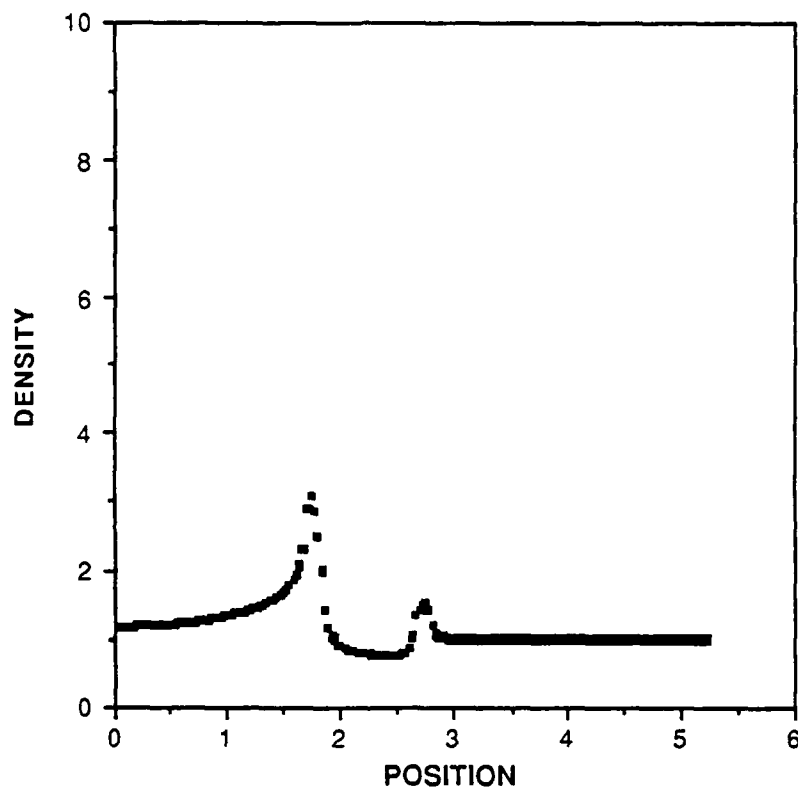


**FIGURE 6.10:** Normalized rail current density for the railgun with guard plate of Figure 4.22. Force developed with this gun is 1.53MN, with a rail current of 1.53MA and a guard plate current of 3.06MA. This calculation invokes limits of  $\leq 1\text{MA}$  and  $\leq 2\text{MA}$  for maximum, allowable, current density peaks in rails and guard plates, respectively. Vector potentials were adjusted so that total guard plate current is twice the total rail current.

**NORMALIZED GUARD PLATE CURRENT DENSITY**  
TWO-RAIL RAILGUN WITH GUARD PLATES  
(WITHOUT OVERHANG)

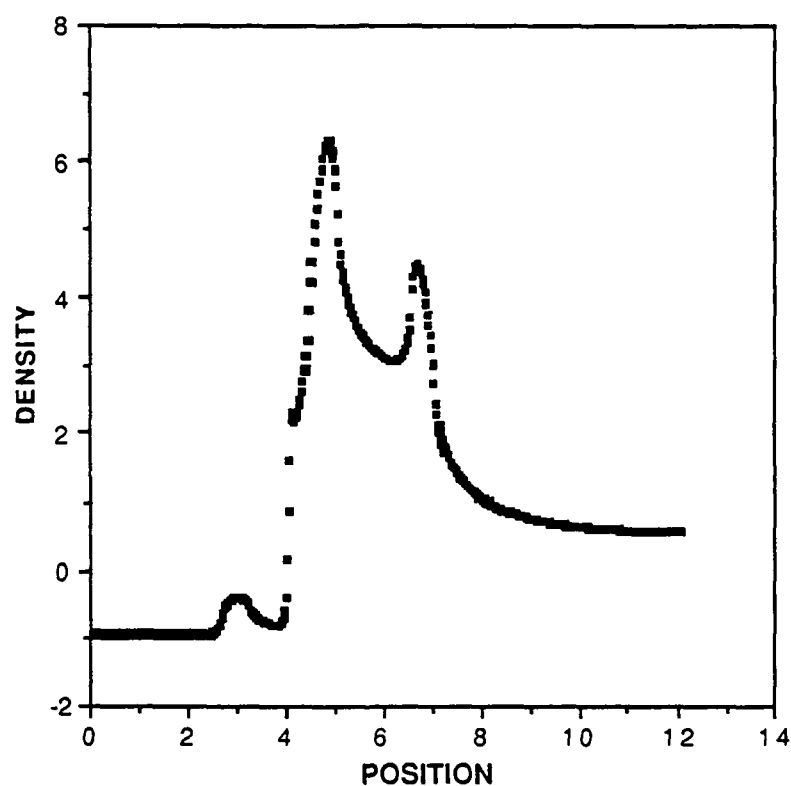


**FIGURE 6.11:** Normalized guard plate current density. This plot is the companion plot of Figure 6.10.

**NORMALIZED RAIL CURRENT DENSITY**  
**TWO-RAIL RAILGUN WITH SPLIT GUARD PLATES**  
(Without Overhang)

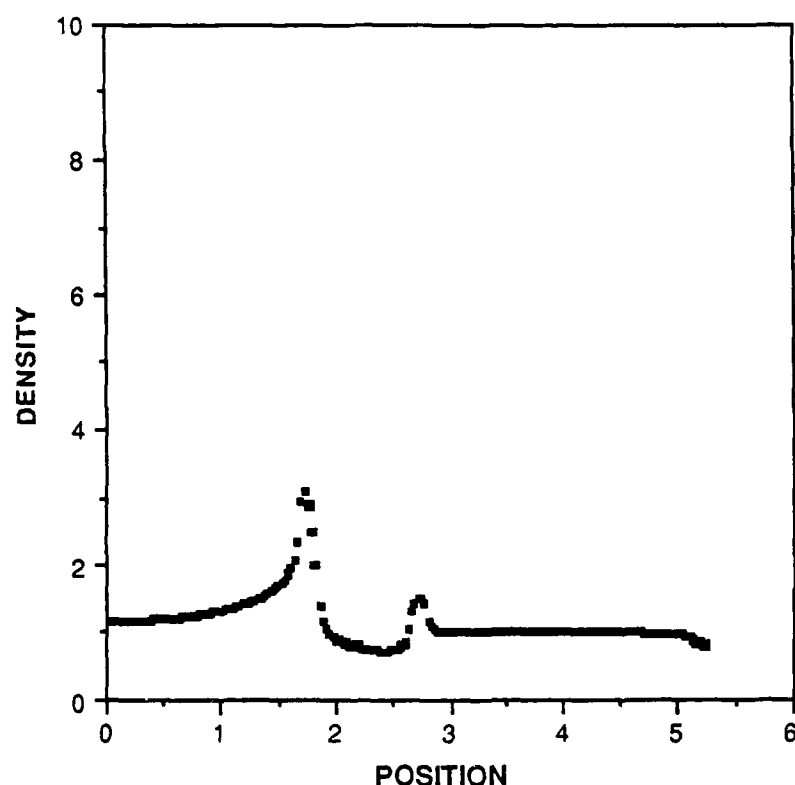


**FIGURE 6.12:** Normalized rail current density for the railgun with guard plate of Figure 6.9. Force developed with this gun is 1.52MN, with a rail current of 1.53MA and a guard plate current of 1.53MA in each half. This calculation invokes limits of  $\leq 1\text{MA}$  and  $\leq 2\text{MA}$  for maximum, allowable, current density peaks in rails and guard plates, respectively. Vector potentials were adjusted so that each half guard plate has the same total current as each rail. This allows series connection.

**NORMALIZED GUARD PLATE CURRENT DENSITY**  
TWO-RAIL RAILGUN WITH SPLIT GUARD PLATES  
(WITHOUT OVERHANG)

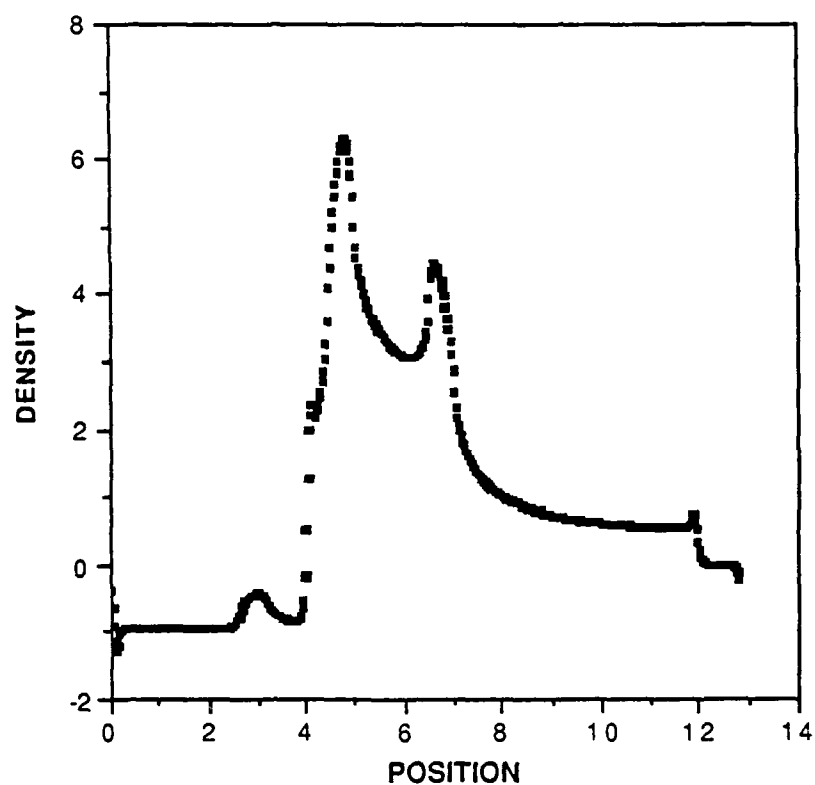


**FIGURE 6.13:** Normalized guard plate current density. This plot is the companion plot of Figure 6.12.



Two comments deserve mention concerning Figures 6.12 and 6.13. First, the guard plate segment associated with Figure 6.13 forms a closed perimeter, so the current density at the position  $s=0.0$  equals the density at position  $s=13.0$ . Second, the dip in rail current density at position  $s=5.4$  in Figure 6.12 is due to the guard plate corner and resulting guard plate density peak on the inside corner of the guard plate split. This is significant because it indicates that guard plate splits in the vicinity of rail density peaks are probably acceptable. The gap in the guard plate is adequately offset by the resulting guard plate corners and associated guard plate current density peaks.

This split guard plate example leads to the conclusion that the complication of separate rail and guard plate power supplies can be avoided without severe performance degradation. Additionally, splitting guard plates to allow a series-connected accelerator leads to a high inductance gradient, which interfaces well with existing power supply options.

#### 6.4 Summary and Conclusions

This dissertation has been an investigation into railgun current management techniques with two explicit objectives: 1) to develop viable multi-rail configurations to allow improved structural design of railguns with better rail containment properties; and 2) to develop active current control measures to favorably influence rail current distribution. The investigation focused on the accelerator portion of railgun systems, so that inherent capabilities and limitations of this component could be isolated. However, the eventual incorporation into useful,

complete systems was not ignored; utility considerations governed the overall direction of the investigation. Consequently, results of this dissertation are useful for many of the presently-envisioned railgun tasks.

Findings of the investigation into multi-rail railguns are summarized in Section 3.6 (simple multi-rail railguns) and Section 5.4 (multi-rail railguns with guard plates). While it is not necessary to repeat these summaries, the most important multi-rail result is worth emphasizing: It is impossible to build simple, multi-rail railguns that can accelerate conventional round-bore projectiles, without accepting substantially-decreased performance or increased rail damage. Attractive multi-rail railgun performance requires unconventional bore geometries or the additional complexity of guard plates. However, there are some encouraging multi-rail results. The aforementioned unconventional bore geometries appear to be generally useful (see Figures 3.21, 3.23 and 3.24). Additionally, multi-rail railguns with guard plates for conventional round-bore projectiles are very promising. This is especially true for large bore railguns, and holds for bores as small as 2.25 cm in radius (as in this dissertation).

The use of guard plates to actively manage rail current distribution for improved performance, a concept originated for this dissertation, appears to be very promising. Specific results for this research objective are summarized in Section 4.8 (two-rail railguns) and Section 5.4 (four-rail railguns). The three to seven fold increases in projectile force listed in Table 4.5 (compare with Table 4.4), even if not totally obtainable in practice, are substantial. The magnitude of this increase

justifies an experimental program to refine and fully develop the concept. As mentioned previously, such an experimental program requires the interdisciplinary contributions of an engineering team and should involve simultaneous research to improve understanding of three-dimensional current distributions in armatures.

In addition to the two explicit research objectives, this dissertation implicitly required substantial effort for development of computational techniques, optimization techniques, and problem definition. Computational techniques are described in Chapter 2 and Section 4.2, and optimization techniques are described in Section 3.5. Problem definition, including such tasks as determination of appropriate accelerator performance criteria, determination of critical variables for optimization, and establishing relative current density limits, is discussed throughout the dissertation. The results of this implicitly required effort are somewhat difficult to evaluate. Although the computational and optimization routines performed satisfactorily, more efficient routines and approaches are possible. The number of computations required for each optimization and the large matrix inversions required for each computation, would have been prohibitive on slower computers than the Cray X-MP/24.

As discussed in the Chapter 1, much progress is required before today's railguns become acceptable alternatives to existing chemical guns for most projectile launching tasks. However, the unique capabilities and advantages of railgun launchers, coupled with the progress of the last ten years, make it worthwhile to continue the development of railgun technology.

It is hoped that the current management concepts, quantitative results, and the progression of ideas presented in this dissertation help advance this important technology.

## Appendix A

### Magnetic Field Plots

The purpose of this appendix is to provide magnetic field plots (or, equivalently, constant contour plots of the vector potential,  $A_z$ ) for some of the railgun geometries discussed in this dissertation. As is customary with plots of this type, field direction is tangent to the plotted curves, and field magnitude is inversely proportional the spacing between curves. The plots were obtained using the updated version of Texas Magnetic Analysis Program (TEXMAP), an internal UT-CEM finite element program.

All plots depict solutions to static, Laplacian, boundary-value problems for the vector potential,  $A_z$ . As discussed in Chapter 2, this represents the situation posed by current-carrying, infinitely-conducting, long conductors in the steady state. For these plots, boundary conditions consisted of specified vector potentials on conductor surfaces; a specified vector potential of zero "far" from the railgun<sup>1</sup>; and appropriate homogeneous Neumann or Dirichlet conditions along lines of symmetry. The caption to each plot references a railgun from Chapters 4 or 5; conductor cross-sections for this railgun have

---

<sup>1</sup> Trial and error determined that 1.4 meters was sufficiently far from the 16 square centimeter, round-bore railgun for this zero condition.

been superimposed on the plots. The absence of contour lines inside conductors reflects the uniformity of the vector potential in these regions. Figures A.2 through A.5 involve railguns with guard plates. For these plots, ratios of rail-to-guard plate vector potentials are the same as for the referenced railgun in Chapter 4 or 5.

For this appendix, no attempt has been made to make field line spacing consistent between plots. Consequently, all plots are independent and contain twenty vector potential contours at equally spaced contour intervals. Nineteen lines are labeled; the twentieth follows the rail perimeter (which is also the conductor with the highest specified vector potential). Field information for the referenced railguns of Chapter 4 or 5 can be obtained only after the field magnitude for some point on the plot is known. For the infinitely-conducting rails and guard plates of this dissertation, with only surface currents, magnetic field boundary conditions provide field magnitudes around conductor perimeters. With this information, these plots can provide good estimates of field magnitudes.

## TWO-RAIL, ROUND-BORE RAILGUN

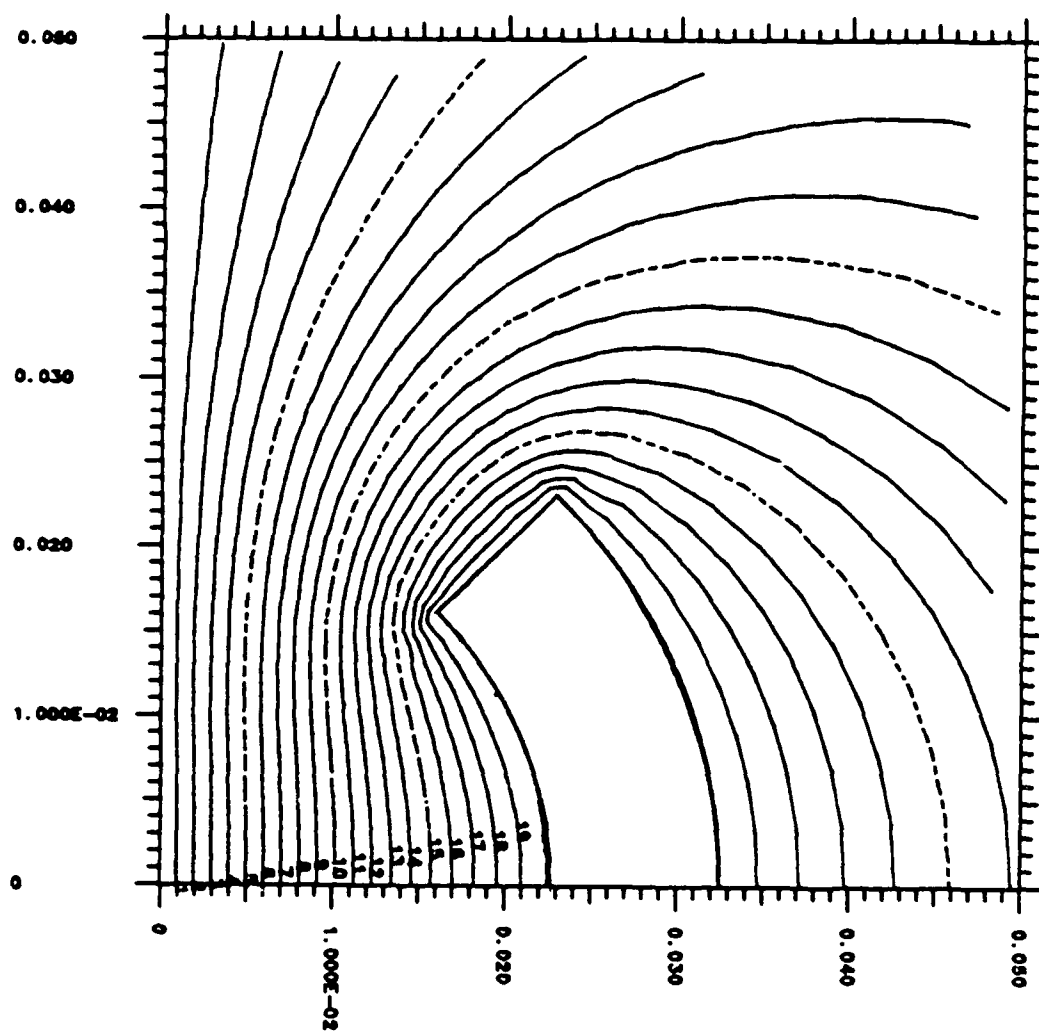


FIGURE A.1: Magnetic field plot for the railgun of Figure 4.14.

FORCE-OPTIMIZED, TWO-RAIL, ROUND-BORE  
RAILGUN WITH GUARD PLATES

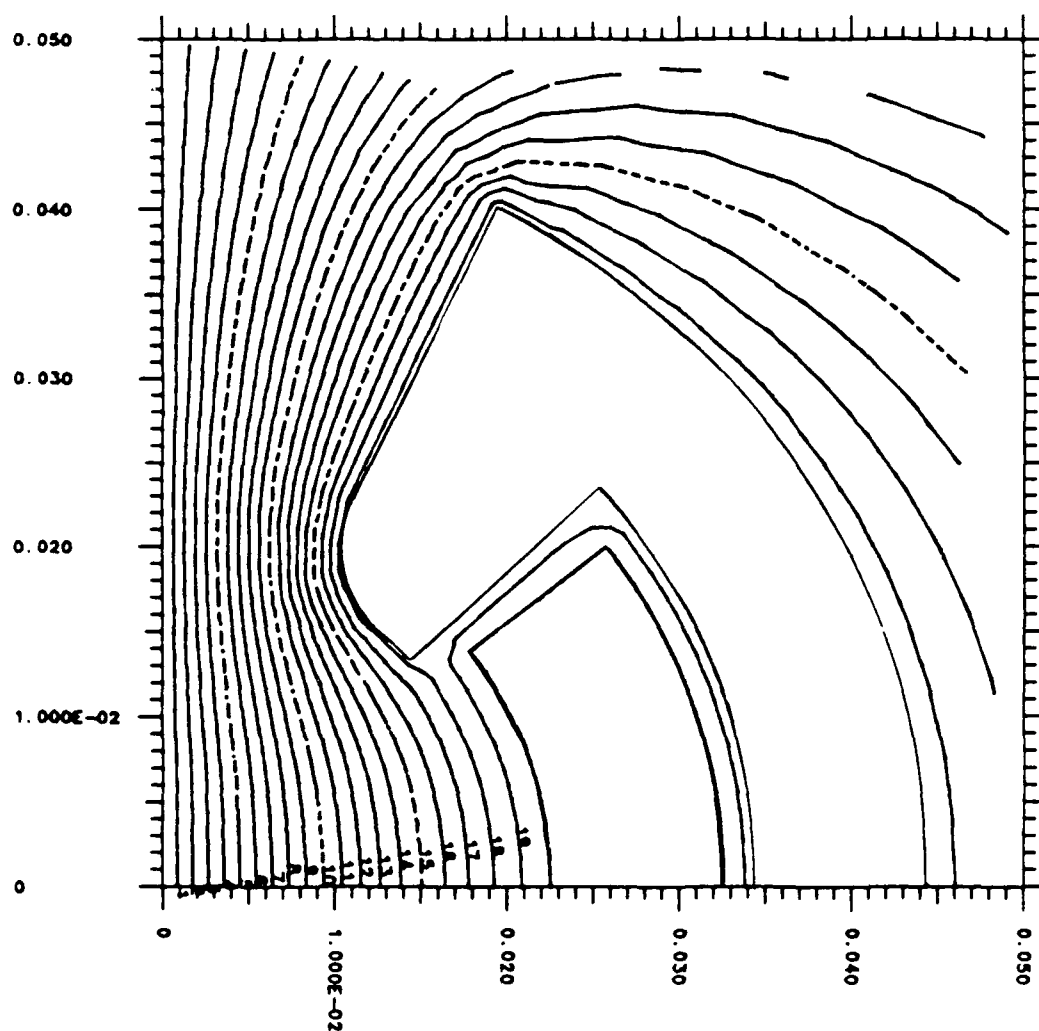


FIGURE A.2: Magnetic field plot for the railgun of Figure 4.19.



# FORCE-OPTIMIZED, TWO-RAIL, ROUND-BORE RAILGUN WITH GUARD PLATES

(Without Overhang)

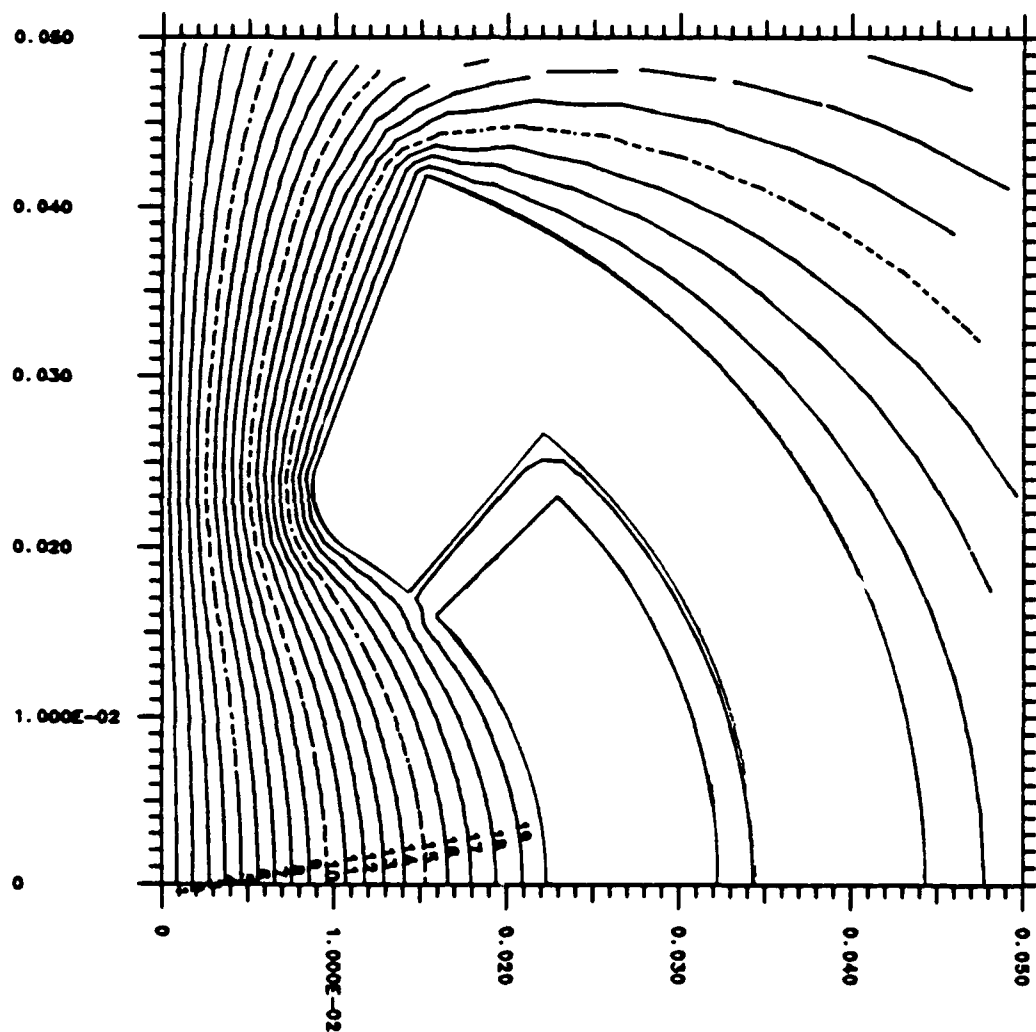


FIGURE A.3: Magnetic field plot for the railgun of Figure 4.22.

CURRENT-OPTIMIZED, TWO-RAIL, ROUND-BORE  
RAILGUN WITH GUARD PLATES  
(Without Overhang)

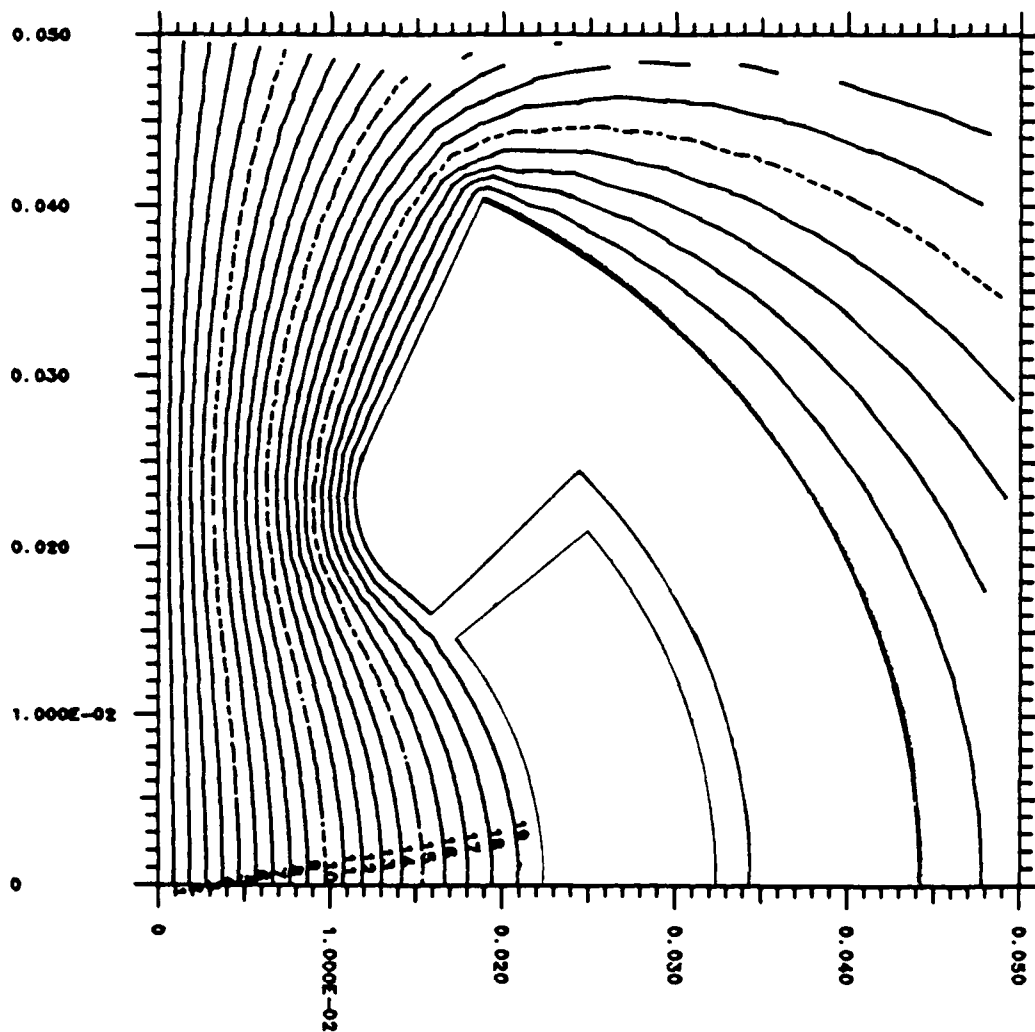


FIGURE A.4: Magnetic field plot for the railgun of Figure 4.27.

# FORCE-OPTIMIZED, FOUR-RAIL, ROUND-BORE RAILGUN WITH GUARD PLATES

(Without Overhang)

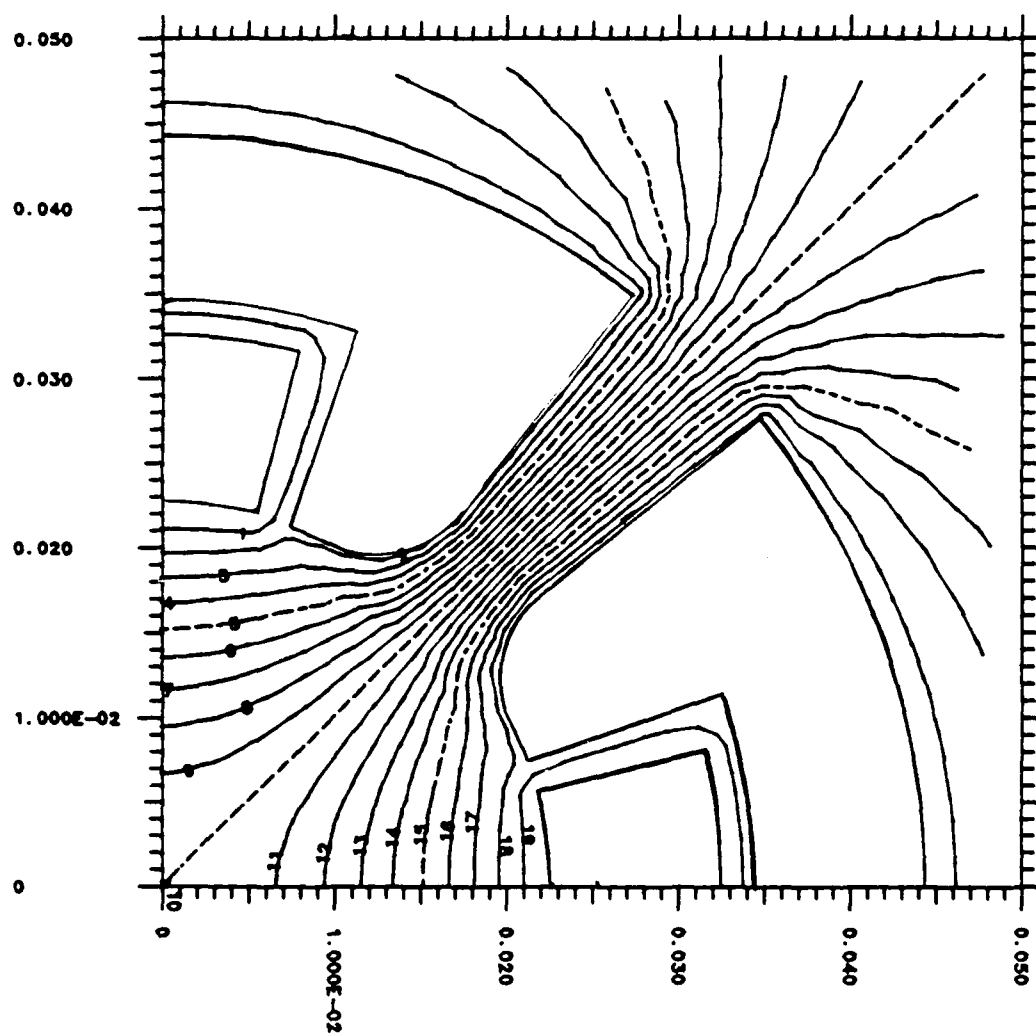


FIGURE A.5: Magnetic field plot for the railgun of Figure 5.4.

## List of References

- Barber, John P. "Metal Armature Critical Issues." Proceedings of the First EM Gun Armature Workshop. Eglin, Florida: Air Force Armament Laboratory, Eglin AFB, June 1986.
- Becker, Eric B.; Carey, Graham F.; and Oden, J. Tinsley. Finite Elements. Vol. 1: An Introduction. Englewood Cliffs, New Jersey: Prentice Hall, Inc., 1981.
- Beno, Joseph H. and Weldon, William F. "An Investigation into the Potential for Multiple Rail Railguns." IEEE Transactions on Magnetics. 25:1 (January 1989a): 92-96.
- . "Railgun Current Guard Plates: Active Current Management and Augmentation." Accepted for publication in IEEE Transactions on Plasma Science. 17:3 (June 1989b).
- Corson, Dale R. and Lorrain, Paul. Introduction to Electromagnetic Fields and Waves. San Francisco: W.H. Freeman and Company, 1962.
- Craddock, W.; Virostek, H.; Calvin, S.; and Eljes, Y. "Thermal Analysis of Fiber Armatures." IEEE Transactions on Magnetics. 25:1 (January 1989): 127-132.
- Deis, D.W.; Scherbarth, D.W.; and Ferrentino, G.L. "EMACK Electromagnetic Launcher Commissioning." IEEE Transactions on Magnetics. 20:2 (March 1984): 245-248.

- Drake, P.A., and Rathmann, C.E. "Two-Dimensional Current Diffusion in an EML Rail with Constant Properties." IEEE Transactions on Magnetics. 22:6 (November 1986): 1448-1452.
- Dukes, J.M. "An Investigation into Some Fundamental Properties of Strip Transmission Lines with the Aid of an Electrolytic Tank." Proceedings of the Institute of Electrical Engineers. Part B, 103 (1956): 319-333.
- Fair, Harry D. "Electromagnetic Propulsion: A New Initiative." IEEE Transactions on Magnetics. 18:1 (January 1982): 4-6.
- Grover, Frederick W. Inductance Calculations. New York: D. Van Nostrand Company Inc., 1946.
- Halliday, David, and Resnick, Robert. Physics. Parts I and II. New York: John Wiley and Sons, Inc., 1967.
- Harrington, Roger F. Field Computation by Moment Methods. Malabar, Florida: Robert E. Krieger Publishing Company, 1983.
- Holland, L.D. "Design, Fabricate and Test a Distributed Energy Electromagnetic Railgun." Ph.D. dissertation, University of Texas at Austin, April 1984.
- Jackson, John David. Classical Electrodynamics. 2d ed. New York: John Wiley and Sons, Inc., 1975.
- Jaeger, J.C. "Moving Sources of Heat and the Temperature at Sliding Contacts." Journal and Proceedings of the Royal Society of New South Wales. LXXVI, Parts I-IV (1942): 203-224.
- Kerrisk, J.F. "Current Distribution and Inductance Calculations for Rail-Gun Conductors." Los Alamos National Laboratory Report, LA-9092-MS: (November 1981).

- Knoepfel, Heinz. Pulsed High Magnetic Fields. Amsterdam: North Holland Publishing Company, 1970.
- Kotas, J.F.; Guderjahn, C.A.; and Littman, F.D. "A Parametric Evaluation of Railgun Augmentation." IEEE Transactions on Magnetics. 22:6 (November 1986): 1573-1577.
- Landau, L.D., and Lifshitz, E.M. Course of Theoretical Physics. Vol. 2: The Classical Theory of Fields. 4th English ed. New York: Pergamon Press, 1975.
- . Course of Theoretical Physics. Vol. 8: Electrodynamics of Continuous Media. 2d English ed. New York: Pergamon Press, 1984.
- Leuer, J.A. "Electromagnetic Modeling of Complex Railgun Geometries." IEEE Transactions on Magnetics. 22:6 (November 1986): 1584-1590.
- Lewis, H.R., Jr. "Computation of Electrostatic and Rapidly Pulsed Magnetic Fields." Journal of Applied Physics. 37:7 (June 1966): 2541-2550.
- Long, G.C. "Railgun Current Density Distributions." IEEE Transactions on Magnetics. 22:6 (November 1986): 1597-1602.
- Long, G.C. "Fundamental Limits to the Velocity of Solid Armatures in Railguns." Ph.D. dissertation, University of Texas at Austin, August 1987.
- Marshall, Richard A. "Current Flow Patterns in Railgun Rails." IEEE Transactions on Magnetics. 20:2 (March 1984): 243-244.
- Paris, Demetrius T., and Hurd, F. Kenneth. Basic Electromagnetic Theory. New York: McGraw-Hill Book Company, 1969.

- Press, William H.; Flannery, Brian P.; Teukolsky, Saul A.; and Vetterling, William T. Numerical Recipes. Cambridge: Cambridge University Press, 1987.
- Price, J.H.; Fahrenthold, E.P.; Fulcher, C.W.G.; Peterson, D.R.; Weldon, W.F.; and Zowarka, R.C., Jr. "Design and Testing of Large Bore, Ultra-stiff Railguns." IEEE Transactions on Magnetics. 25:1 (January 1989): 460-466.
- Ramo, Simon; Whinery, John R.; and Van Duzer, Theodore. Fields and Waves in Communication Electronics. 2d ed. New York: John Wiley and Sons, 1984.
- Smythe, William R. Static and Dynamic Electricity. New York: McGraw-Hill Publishing Company, 1950.
- Woodson, Herbert H. and Melcher, James R. Electromechanical Dynamics. Part 1: Discrete Systems. New York: John Wiley and Sons, 1968.
- Young, Fredrick J., and Hughes, William F. "Rail and Armature Current Distributions in Electromagnetic Launchers." IEEE Transactions on Magnetics. 18:1 (January 1982): 33-41.

## VITA

**Joseph Henry Beno Jr.**

he entered the United States Military Academy at West Point, New York, in 1967. There, he was awarded a Bachelor of Science degree and commissioned as a Second Lieutenant in the United States Army in 1971. He still serves on active duty in the Army in the rank of Lieutenant Colonel. His early assignments included duty with field soldiers in the Federal Republic of Germany, logistics management positions, and missile maintenance management positions. He attended the University of Alabama at Huntsville, Alabama from 1976 thru 1978 and received a Masters of Science Degree in Physics. Since then, his military assignments have included additional duty with field soldiers, three years in Army Research and Development programs, and two years as an academic instructor in the Department of Physics, at the United States Military Academy at West Point. In September 1986, he entered the graduate program in Electrical Engineering at the University of Texas, Austin, Texas.

This dissertation was typed by Joseph H. Beno.